ON THE MODELING AND SUPPRESSION OF ELECTROMAGNETIC INTERFERENCE EMISSIONS OF POWER CONVERTERS

ON THE MODELING AND SUPPRESSION OF ELECTROMAGNETIC INTERFERENCE EMISSIONS OF POWER CONVERTERS

BY

FATEMEH ABOLQASEMI, M.Sc.

A THESIS

SUBMITTED TO THE DEPARTMENT OF ELECTRICAL AND COMPUTER ENGINEERING

AND THE SCHOOL OF GRADUATE STUDIES

OF MCMASTER UNIVERSITY

IN PARTIAL FULFILMENT OF THE REQUIREMENTS

FOR THE DEGREE OF

DOCTOR OF PHILOSOPHY

Doctor of Philosophy (2022) McMaster University

(Electrical and Computer Engineering) Hamilton, Ontario, Canada

TITLE:	On the Modeling and Suppression of Electromagnetic Interference Emissions of Power Converters
AUTHOR:	Fatemeh Abolqasemi M.Sc. (Electrical Engineering), Sharif University of Technology, Tehran, Iran B.Sc. (Electrical Engineering), Sharif University of Technology, Tehran, Iran
SUPERVISORS:	Dr. Ali Emadi Ph.D. (Texas A&M University, College Station, Texas, USA) Dr. Berker Bilgin Ph.D. (Illinois Institute of Technology, Chicago, Illinois, USA)
NUMBER OF PAGES:	xxi, 200

Abstract

Electromagnetic interference (EMI) issues are associated with high-speed switching of power converters. EMI modeling is an essential tool to study and control the EMI emission, enabling more efficient solutions. A comprehensive review and comparison of different modeling approaches for conducted emissions are provided in this paper, which can be used as a design guideline for engineers. Electromagnetic compatibility (EMC) measurement devices and testing procedures are also reviewed for power converter applications. This overview would help the reader to obtain a better understanding of the EMC testing procedure, requirements, and the EMC measurement devices. Afterwards, conducted emissions in a three-phase inverter fed motor drive is studied. A physics-based model is derived for each part of the system using a device characterization tool, a finite element analysis tool, and impedance curve fitting tools. An improved universal equivalent circuit is proposed to model the induction motor in the entire frequency range. A balanced approach regarding the accuracy and simplicity of the model is considered through the model extraction. Furthermore, common mode and differential mode emissions are studied, and two equivalent circuits are extracted.

Spread spectrum modulation techniques have been proven to be an effective solution to suppress the conducted electromagnetic emissions of power converters. Various

modulation methods are investigated for an active neutral point clamped (ANPC) inverter. The effect of EMI receiver and intermediate filter bandwidth is also considered in the modeling. Furthermore, a new unified model is proposed for an active neutral point clamped inverter based on the existing equivalent circuit models for common mode (CM) EMI and the developed DM model. In another approach to reduce the EMI emissions, a new hybrid CBPWM strategy is proposed that not only eliminates the neutral point voltage oscillations but also reduces the common mode voltage (CMV) by half. Furthermore, the harmonic content of the output voltage is reduced by adjusting the modulation waves based on the location of the reference vector in the space vector diagram. An active neutral point voltage controller is also presented and applied in order to maintain the performance of the modulation strategy under the NPV perturbations. Modeling and simulation results are validated by experimental results.

To my Mom.

Acknowledgements

First and foremost, I would like to express my sincere gratitude to my supervisors Dr. Ali Emadi and dr. Berker Bilgin for their invaluable encouragement, support, and guidance throughout my four years' Ph.D. research at McMaster University. It has been a great honor to work with them for the past few years. Without their help, the completion of this thesis would have been impossible. I would also like to thank my supervisory committee members, Dr. Mehdi Narimani and Dr. Sanjaka Wirasingha, for their insightful comments and discussions throughout the course of my studies.

This research was undertaken, in part, thanks to funding from the Canada Research Chair in Transportation Electrification and Smart Mobility, Natural Sciences and Engineering Research Council of Canada (NSERC), and McMaster University.

My gratitude also goes to Dr. Nasiri-Gheidari, my Master's supervisor, who first convinced me to pursue my Ph.D. studies ending up in this amazing adventure in Canada. I would also like to thank all my colleagues and friends from McMaster Automotive Resource Centre (MARC) for their accompaniment and concerns. Especially, I would like to thank Amirreza Pourfakhraei and Yicheng Wang for their help with the experimental setup.

Finally, special thanks must go to my family and my dear husband. I would like to thank them for their endless love, care, and support throughout my entire life.

Notation and Abbreviations

Abbreviations

ANPC	Active neutral point clamped
CBPWM	Carrier-based pulse width modulation
CM	Common mode
CMV	Common mode voltage
CSFPWM	Constant switching frequency PWM
DM	Differential mode
EMC	Electromagnetic compatibility
EMI	Electromagnetic interference
EUT	Equipment under test
FD	Frequency domain
FFT	Fast Fourier transform

IGBT	Insulated gate bipolar transistor
LISN	Line impedance stabilizer network
NP	Neutral point
NPV	Neutral point voltage
NPC	Neutral point clamped
PCFM	Periodic carrier frequency modulation
PWM	Pulse width modulation
RCMV-CBPWM	Reduced common mode voltage CBPWM
RMS	Root mean square
RCFM	Random carrier frequency modulation
RBW	Resolution band width
SA	Spectrum analyzer
SVM	Space vector modulation
TEFSM	Thevenin equivalent frequency domain source model
TD	Time domain

Contents

Abstract **iii**

Acknowledgements **vi**

Notation and Abbreviations **vii**

1 Introduction **1**

1.1 Background and motivations 1

1.2 Contributions and thesis outline 3

2 Modeling of Conducted Emissions for Electromagnetic Interference (EMI) Analysis of Power Converters: State-of-the-Art Review **6**

2.1 Introduction 7

2.2 EMC measurement and standards 9

2.3 Overview of EMI modeling 13

2.3.1 Signal integrity and cross-talk 14

2.3.2 Conducted emissions 15

2.4 Parasitic components 22

2.4.1 Bulk capacitor 23

2.4.2 Switching devices 24
2.4.3 Bus bars 26
2.4.4 Motors 28
2.4.5 Cables 30
2.5 Simulation methodologies 31
2.6 Summary 37

3 Modeling of Conducted Electromagnetic Emissions for a Three-Phase Inverter Fed Motor Drive 38

3.1 Introduction 39
3.2 Time domain model 40
3.2.1 Switching module 41
3.2.2 Busbars 47
3.2.3 Electric machine 50
3.2.4 Capacitor and LISN 56
3.3 Conducted emissions 58
3.3.1 Common mode 60
3.3.2 Differential mode 61
3.4 Summary 66

4 On the Electromagnetic Compatibility (EMC) Measurement and Testing Procedures for Power Converters 67

4.1 Introduction 67
4.2 EMC test procedures 70
4.2.1 Test plan 71

4.2.2 EMC tests . . . 73
4.3 EMI receivers and analyzers . . . 79
4.4 Measurement devices . . . 83
4.4.1 Conducted emissions . . . 84
4.4.2 Radiated emissions . . . 86
4.5 Test equipment on the market . . . 86
4.6 Summary . . . 87

5 Analytical EMI Modeling of an Active Neutral Point Clamped Inverter 89
5.1 Introduction . . . 90
5.2 Time domain model . . . 92
5.3 Frequency domain model . . . 94
5.3.1 EMI noise source modeling . . . 95
5.3.2 Unified equivalent circuit model . . . 97
5.4 Conducted emissions . . . 98
5.5 Summary . . . 100

6 Mitigating Conducted Electromagnetic Interference of an Active Neutral Point Clamped Inverter by Spread Spectrum Modulation 103
6.1 Introduction . . . 104
6.2 Analysis of spread spectrum modulation techniques . . . 108
6.2.1 Periodic CFM . . . 110
6.2.2 Random PWM . . . 113
6.3 EMI receiver model . . . 116

6.4 Evaluation of spread spectrum modulations 121
6.4.1 Conducted EMI emissions 123
6.4.2 Overall evaluation 125
6.5 Experimental evaluation 127
6.5.1 Experimental setup 127
6.5.2 EMI receiver model verification 127
6.5.3 Detailed model verification 128
6.5.4 Experimental results 129
6.6 Summary 131

7 An Improved Carrier Based PWM Strategy with Reduced Common Mode Voltage for a Three Level NPC Inverter 134

7.1 Introduction 135
7.2 NP current and CMV of the three-level NPC 137
7.2.1 Neutral point current 139
7.2.2 Common mode voltage 142
7.3 Derivation of the proposed HCBPWM 143
7.3.1 Principle of the operation 145
7.3.2 CMV reduction 149
7.3.3 Harmonic content 152
7.3.4 Neutral point voltage deviation 154
7.4 Active NPV controller 156
7.5 Experimental results 159
7.6 Summary 163

8 Conclusions and Future Work **164**

8.1 Conclusions 164

8.2 Future work 166

List of Figures

1.1 As the equipment develops, the number of available EMI solutions are limited and more expensive. 2

2.1 Different aspects of EMC problem. 8

2.2 CISPR32 class B conducted emission limits (QP and AVG denote quasi-peak and average measurement techniques, respectively). 11

2.3 Line impedance stabilization network(LISN), (a) Schematics (b) Impedance looking into LISN seen by EUT. 13

2.4 Common mode and differential mode currents. 14

2.5 Classification of conducted EMI modeling techniques. 16

2.6 Thevenin equivalent EMI noise emission model for a single IGBT . . 18

2.7 Norton equivalent EMI noise emission model of an IGBT phase leg . 19

2.8 Generalized three-terminal equivalent circuit 21

2.9 Motor drive system including dominant stray components. 23

2.10 Equivalent circuit of a bulk capacitor. 24

2.11 Equivalent circuit of an IGBT phase leg with stray capacitances and inductances 26

2.12 Piece-wise linear IGBT model 27

2.13 A simple laminated bus bar. 27

2.14 High frequency per phase model for an induction motor 29
2.15 Per section equivalent circuit for modeling a long cable 31
2.16 (a) Trapezoidal waveform and (b) the bounds on its harmonic spectrum. 33
2.17 Discreet harmonic spectrum and the spectral bounds for a trapezoidal signal with $D = 0.1$, $A = 200$, $f_{sw} = 10kHz$, $t_r = 200ns$. 33
2.18 CM current paths in a buck converter. 36
3.1 Motor drive system including main parasitic elements. 41
3.2 Test circuit for IGBT characteristics. 43
3.3 Switching transients of Case 1 a)turn off b)turn on. 43
3.4 Internal construction layers of the IGBT module. 45
3.5 3D simplified model of the IGBT module. 46
3.6 Stray capacitances of the power module. 46
3.7 AC current density distribution in the dc busbar. 49
3.8 high frequency equivalent circuit of the induction motor a) per-phase equivalent circuit b) three-phase differential model c) three-phase common mode model. 51
3.9 Measurement setup for motor impedance measurement a) differential mode b) common mode 51
3.10 Universal per-phase equivalent circuit a) previous model b) proposed model 52
3.11 Measured CM and DM characteristics. 53
3.12 Measured and simulated impedance magnitude a) DM b) CM. 55
3.13 Differential mode impedance of the motor for different operating points represented by rotor slip (s). 55

3.14 Equivalent circuit of the dc link capacitor. 56
3.15 Line impedance stabilization network. 57
3.16 Inverter output a) motor phase current and b) output line voltage. . . 58
3.17 Motor drive system where switches are replaced by noise sources. . . 59
3.18 CM equivalent circuit of the three-phase motor drive. 61
3.19 CM path g-parameter (G_{CM}) characteristics. 61
3.20 CM conducted emissions of the three-phase motor drive. 62
3.21 DM equivalent circuit of the three-phase motor drive. 62
3.22 DM path impedance characteristics. 63
3.23 DM conducted emissions of the three-phase motor drive. 63
3.24 Unified equivalent circuit of the motor drive system. 64
3.25 DM conducted emissions considering the coupling between CM and DM. 65
4.1 Block diagram of operating principle of frequency domain EMI measurement. 80
4.2 Time domain measurement process. 82
4.3 Coupling capacitors in an immunity test setup. 85
4.4 Common antennas for radiated emissions measurement. 86
5.1 The detailed model of the ANPC considering main parasitic elements. 92
5.2 Common mode modeling of the ANPC a) Phase A leg, b) Substituting MOSFETs with voltage and current sources, c) Short circuiting the dc link capacitors and sources are merged, d) Three phase CM model of the inverter. 94
5.3 Differential mode modeling of the ANPC, a) substituting MOSFETs with current and voltage sources, b) DM model of the inverter. 97

5.4 Asymmetric impedance paths of CM currents leading to MM emissions (state P in phase A). Red arrows: CM currents, blue arrows: DM currents. 99
5.5 Unified equivalent circuit of the system. 99
5.6 Comparison between the prediction of unified equivalent circuit and the detailed model a) V_{CM}, b) V_{DM}. 101
5.7 Prediction error of V_{MD} in different models. 101
6.1 EMI suppression methods. 105
6.2 Harmonic spectrum of the CM voltage of a three phase conventional inverter using two IGBTs. 106
6.3 A classification of spread spectrum modulation techniques. 107
6.4 A typical PWM waveform. 110
6.5 Relationship between the current and the switching frequency. 113
6.6 Carrier frequency functions of distribution-based PCFM a) uniform b) normal and c)exponential. 114
6.7 Harmonic spectrum of EMI conducted emissions of the ANPC. 116
6.8 The calculation process to model a swept-tuned spectrum analyzer. . 117
6.9 The Gaussian intermediate filter gain. 118
6.10 The calculation process of time domain EMI measurement. 120
6.11 Comparison between the FFT output, swept-tuned spectrum analyzer, and TDEMI. 120
6.12 The detailed model of the ANPC considering main parasitic elements. 121
6.13 Common mode emissions of the ANPC applying different modulation methods. 124

6.14 The experimental setup of the 3-L ANPC. 128
6.15 Comparison between the measurement results of the SA and the Oscilloscope. 129
6.16 Conducted emissions of the inverter, measurement and simulation results a) DM, b) CM. 130
6.17 Measured line-to-line voltages with harmonic spectrum a) CCFM, b) PCFM, c) RCFM. 131
6.18 Conducted emissions of the inverter, measurement results a) DM, b) CM. 132
7.1 Topology of the ANPC and its space vector diagram. 138
7.2 a) Virtual space vector diagram in sector I, b) switching sequence of V_{ref}, resultant NP current, the NPV variations, and the generated V_{CM}. 141
7.3 Conventional CBPWM with two carriers. 144
7.4 Construction of the phase leg state using positive and negative modulation waves. 145
7.5 Positive and negative modulation waves of phase A, $m = 0.8$. 149
7.6 The reversed switching patterns using two carriers with opposite phases. 150
7.7 Different combination of switching sequences to reduce CMV when only a) u_{mid}, b) u_{max}, c) u_{min} has different switching pattern. 151
7.8 Harmonic flux trajectories of a) conventional CBPWM in Sector I, b) double modulation RCMV-CBPWM when u_{min} is reversed in all Sectors. 153
7.9 RMS value of the HFT in a fundamental cycle for three different modulation. 153

7.10 Neutral point current (rms) in the first Sector for unity power factor when a) u_{max} is reversed, b) u_{min} is reversed. 155
7.11 Neutral point current (rms) of the proposed hybrid modulation for unity power factor in the first Sector. 155
7.12 Space vector diagram of the proposed hybrid CBPWM with reduced CMV. 156
7.13 Adjusting the duty ratio of the median phase, u_{mid}, for NPV control. 157
7.14 Positive and negative compensating currents in Sector I when a) $\phi = 0$, b) $\phi = \pi/4$. 159
7.15 Average positive and negative compensating currents under different power factors and modulation indices. 160
7.16 The experimental setup of the 3-L ANPC. 161
7.17 Measured line-to-line voltages, dc-link capacitor voltages, output current i_a, U_{cm}, and harmonic content of U_{ab}; a) conventional CBPWM, b) RCMV-CBPWM when only phase a is reversed, c) proposed CBPWM with CMV reductions. 162
7.18 Experimental waveforms for voltage balancing control. 162

List of Tables

3.1 Switching characteristics of the IGBT (Sim: simulation result, Data: datasheet value) 43

3.2 Power loss of the single-phase full bridge inverter 44

3.3 Stray capacitances of the power module 46

3.4 Stray components of the busbar 50

3.5 Improved universal model parameters and the induction motor specifications 55

3.6 Natural frequencies of each conduction mode 65

4.1 A sample EMC test plan 72

4.2 List of EMC certificates of a three-phase solar inverter 72

4.3 Harmonic limits for class A equipment EN61000-3-2 76

4.4 EMC equipment manufacturers 88

5.1 The Design Parameters of the Active Neutral Point Clamped Converter 93

5.2 Switching characteristics of the SiC Mosfet (sim: simulation result, data: datasheet value) 93

6.1 FCC minimum 6 dB resolution bandwidth (RBW_6) 118

6.2 ANPC parameters 122

6.3 Switching characteristics of the SiC Mosfet (sim: simulation result, data: datasheet value) 122
6.4 Maximum suppression of CM EMI emissions for different SS modulation methods 126
6.5 Current THD and power loss of the ANPC for different SS modulation methods 127
6.6 Experimental parameters 129
7.1 Switching states of a 3L-ANPC 138
7.2 The effect of medium and small vectors on the NP 139
7.3 Generated CMV by different space vectors 143
7.4 Experimental parameters 160

Chapter 1

Introduction

1.1 Background and motivations

Electromagnetic interference (EMI) can be regarded as environmental pollution, similar to air pollution. Over the past hundred years, humankind has been using the electromagnetic spectrum extensively. Thanks to the advent of modern semiconductor technologies, the number of electronic devices has grown vastly during the recent decades. So, more electronic systems are now supposed to work near each other and share the EM spectrum. EMI is the inevitable economic and social threat of such a chaotic system that may result in various types of malfunction or even detrimental injuries.

Unfortunately, there is a tendency to overlook the EMI issues by both the manufacturers and the consumers especially when the EMC certificates are not mandatory. One of the contributing factors might be that EMC issues are sometimes hard to recognize and pricey to overcome. On the other hand, EMC failures are way more expensive. Every year, numerous EMC failure stories are reported across the globe

concerning different threat levels. It can be a harmless TV glitch while using the microwave, or it could be a dreadful train crash [1]. As an example, let us look at the "defect information report" submitted to the National Highway Traffic Safety Administration (NHTSA) by TOYOTA in 2013. Following 18 confirmed U.S. cases of abrasion-type injuries from the faulty airbag deployment, TOYOTA had to recall more than one million Corolla, Corolla Matrix, and Pontiac Vibe models across the globe. According to the report, a short circuit in the control module of the airbags occurs when they are exposed to high inductive electrical noise from various vehicle electrical components. In order to solve the problem, additional filters were added to the control module [2].

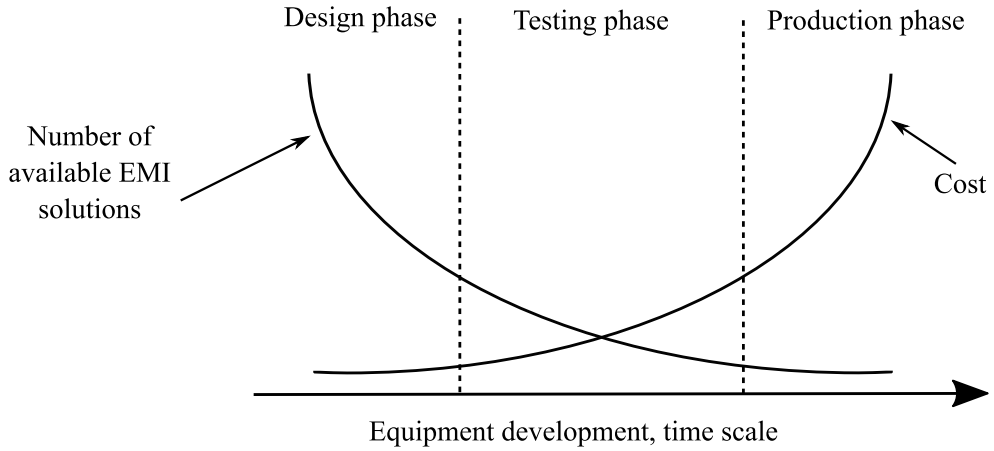

Figure 1.1: As the equipment develops, the number of available EMI solutions are limited and more expensive.

An electromagnetic compatible system happily functions without interfering with itself or the nearby devices. An interference is generated by nature or man-made devices. The EM energy is then transferred to the victim through conduction and radiation. It is more cost effective to deal with the EMI problems in the early stage of the design. As the electronic device develops, fewer EMI solutions are available

at a higher price, as depicted in Fig. 1.1 [3]. Keeping in mind that EMI should be considered during the design, this thesis aims to provide a road map of EMC studying for power electronic inverters.

1.2 Contributions and thesis outline

This thesis studies the conducted emissions in power inverters. After reviewing the basic concepts of EMI in power converters, the first step is to develop an EMI model that suits the research goals. In this regard, Chapter 2 presents a comprehensive literature review of available modeling strategies along with the definition of EMI basics. Moreover, EMC measurement devices and testing procedures are reviewed for power converter applications in Chapter 4. The topics discussed here help the reader obtain an overview of the EMC testing and develop a comprehensive understanding of the EMC measurement device.

In Chapter 3, the modeling process is studied in detail for a three-phase motor drive system. A physics-based model is derived for each part of the system using a device characterization tool, a finite element analysis tool, and impedance curve fitting tools. An improved universal equivalent circuit is proposed to model the induction motor in the entire frequency range. A balanced approach regarding the accuracy and simplicity of the model is considered through the model extraction. Furthermore, common mode and differential mode emissions are studied, and two equivalent circuits are extracted.

Equivalent circuits are a more robust analysis tool during the design process. Hence, equivalent circuit modeling is extensively studied for a three-level neutral point clamped inverter in Chapter 5. Compared with the conventional differential

mode (DM) EMI modeling of power inverters that use only one current source, it is shown that two current sources are required for more precise modeling. A new unified model is proposed for an active neutral point clamped inverter based on the existing equivalent circuit models for common-mode (CM) EMI and the developed DM model. The proposed model predicted both CM and DM EMI emissions and compared them with the time-domain results. Simulation results indicate that the modeling precision is improved by 56%.

In order to mitigate the EMI issues, various approaches are recommended in the literature. Software-based methods that generally suppress the emissions at the source are more cost-effective than hardware-based solutions such as EMI filters. In the last two chapters, two means of EMI noise suppression are explored. In Chapter 6, spread-spectrum modulation techniques are studied and implemented. These methods spread the power spectrum in the frequency range, thus reducing the harmonic spikes. Different spread-spectrum modulations are investigated for an active neutral point clamped (ANPC) inverter. The effect of EMI receiver and intermediate filter bandwidth is considered in the modeling. The validity of simulation results and calculations is confirmed by experimental results.

In another software-based EMI suppression method, a new hybrid CBPWM strategy is proposed in Chapter 7 that not only eliminates the neutral point voltage oscillations but also reduces the common-mode voltage (CMV) by half. Furthermore, the harmonic content of the output voltage is reduced by adjusting the modulation waves based on the location of the reference vector in the space vector diagram. An active neutral point voltage controller is also presented and applied in order to maintain the performance of the modulation strategy under the NPV perturbations. The

performance of the proposed algorithm is compared to the conventional CBPWM and another CBPWM with reduced CMV that is already available in the literature. Finally, experimental results are presented to evaluate the proposed modulation strategy.

Chapter 8 concludes the thesis by summarising the chapters and providing suggestions for future works.

Chapter 2

Modeling of Conducted Emissions for Electromagnetic Interference (EMI) Analysis of Power Converters: State-of-the-Art Review

Electromagnetic interference issues are associated with high-speed switching of power converters. EMI modeling is an essential tool to study and control the EMI emission, enabling more efficient solutions. A comprehensive review and comparison of different modeling approaches for conducted emissions are provided in this chapter, which can be used as a design guideline for engineers. For a motor drive application, common mode and differential mode conducted emissions are studied, and dominant

noise production mechanisms are identified. Moreover, a review of various modeling techniques is presented for the main parasitic components of the system. Finally, time domain and frequency domain analysis approaches are explored along with the equivalent circuits which enable fast prediction of EMI emissions. This chapter intends to help the reader develop an organized understanding of conducted emission modeling to assist them with a more efficient and electromagnetically-compatible design.

2.1 Introduction

With the recent advancements in power electronic technologies, designers and manufacturers tend to go for higher switching frequencies which allows to reduce the size of the converter. Therefore, the operation of electronic devices in close proximity within a power converter is inevitable in modern days. These circuits often adversely affect each other, which may cause malfunction. This has brought an important concern into attention: electromagnetic compatibility (EMC). A system is electromagnetically compatible if it

- functions properly in the intended environment,
- is not a major source of electromagnetic pollution to the environment,
- does not interfere with itself.

EMC is associated with generation, transmission and reception of electromagnetic energy, as shown in Fig. 2.1. A source generates the emission that is transmitted to the receiver through a transfer or coupling path in forms of radiation or conduction. The received signal is processed in the receptor which may or may not cause undesired

behavior. Note that the processing is important in the receptor. In some cases, the received energy has no effect on the function of the receptor and is not specified as interference.

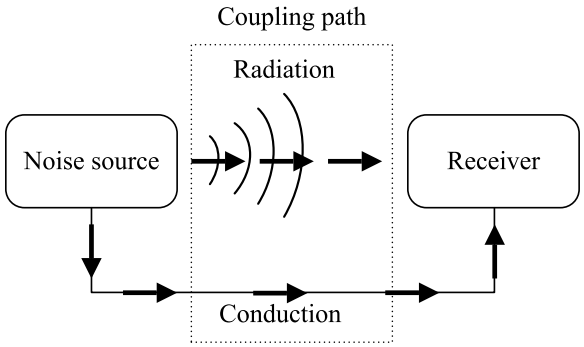

Figure 2.1: Different aspects of EMC problem.

In terms of cost and time, it is more effective to consider EMI issues at the design stage that would minimize post-processing solutions, including additional mitigation components, and testing time and cost. An EMI-integrated design requires comprehensive system modeling capable of predicting EMI emissions. Although there are many papers on EMI modeling of power converters, the absence of a comprehensive review is noticeable. This chapter intends to assist the reader in expanding a thorough knowledge of EMI modeling methods which can be used as a general guideline for engineers to determine the most appropriate modeling methods for the given application. In this chapter, available modeling methods in the literature for conducted EMI emissions of power converters are presented. Next, dominant noise production mechanisms are identified in an inverter-fed motor drive system, and different modeling techniques for the main parasitic components of such systems are also studied. Time domain and frequency domain analysis approaches are also investigated.

2.2 EMC measurement and standards

Electromagnetic compatibility is not only an important index of performance but also a legal requirement for any electronic device before marketing. Employing standards, governments ensure that EMC is controlled in the design and use of electronic equipment. EMC standards usually have a section explaining the technical terms and other sections to define the test equipment, test methods, acceptable measurement receivers and the specific limits that must be met [4].

In the United States, the Federal Communications Commission (FCC) regulates the EMI requirements. Under Title 47 of the Code of Federal Regulations, the FCC Rules and Regulations have several parts concerning the control of interference. Part 15 contains the requirements for radio frequency devices defined as any device capable of emitting radio-frequency energy from 9 kHz to 3000 GHz by conduction or radiation. FCC part 15 has six subparts, which Subpart B is more relevant due to its applicability to digital electronics [5]. Outside of the U.S., the regulations of the International Special Committee on Radio Interference (CISPR, from its French title), which is a part of the International Electrotechnical Committee (IEC), are widely accepted. The requirements of CISPR 32 or the equivalent European Union EN55032 apply to multimedia equipment in order to protect radio frequency band from 9 kHz to 400 GHz[6]. Based on the end-consumer, FCC and CISPR define two types of products: class A products intended for business and industrial environment, and class B equipment marketed for residential setting. The requirements of class B products have more restrictive limits, as the possibility of EMI problems is higher due to the close proximity of electronic devices. Another important EMC standard is published by the U.S. Department of Defense that apply to the military and aerospace

industry. Many military organizations outside of the U.S. have adopted the limits specified by the standard MIL-STD-461G[7].

CISPR 32 or FCC part 15 are the main standards considered in here. Either class B or class A limits can be applied based on the end-user. Fig. 2.2 shows the FCC and CISPR limits for conducted emission of class B products. QP and AVG in Fig. 2.2 denote quasi-peak and average measurement techniques, respectively. Peak detectors normally measure the highest value of the signal regardless of the energy they carry or duration of their existence. However, studies have shown that the level of noise disturbance is also related to the repetition rate of the signal. Therefore, a quasi-peak detector measures the weighted signal according to the repetition rate. For a continuous waveform, peak and quasi-peak would be the same. The quasi-peak measurement is proportional to the amplitude and the repetition rate. A quasi-peak test is required in case the peak values marginally pass the limits. If the measured noise is below the quasi-peak limits, the product is likely to pass the compliance tests.

In addition to setting the limits, every standard defines how to measure the data. The limits set for conducted emissions regulate the emitted noise conducted through the power cord as it is connected to the distribution system and capable of interfering with other subsystems. The conducted emission that needs to be measured is the noise current conducted back to the ac power cord. CISPR and FCC use a standard Line Impedance Stabilizer Network (LISN) placed between the equipment under test (EUT) and the power cord. A common $50\mu H$ LISN is shown in Fig. 2.3(a). The first function of LISN is to prevent the outside noises from contaminating the measurement. L_1 and C_2 in Fig. 2.3(a) block and divert noises coming from the power

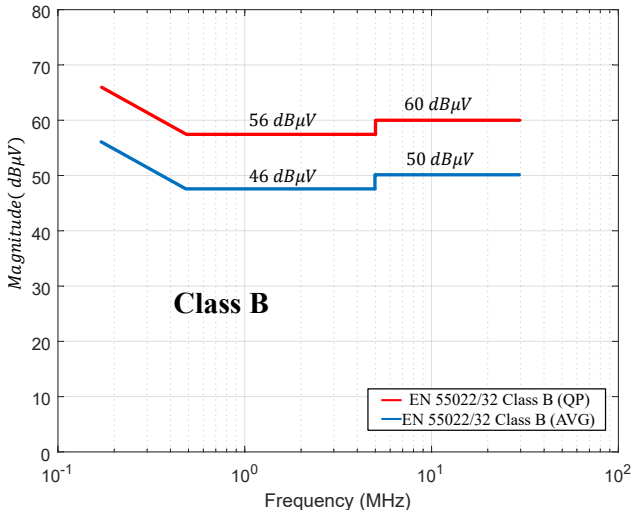

Figure 2.2: CISPR32 class B conducted emission limits (QP and AVG denote quasi-peak and average measurement techniques, respectively).

system within the conducted emission frequency range. The second function of LISN is to present a constant impedance to the product terminals at the frequency range of measurement (150 kHz to 30 MHz). The impedance of the power line can vary at different locations for different power ratings. It can be seen in Fig. 2.3(b) that the impedance is seen by the equipment looking into LISN (between phase/neutral and ground wire, denoted by Z_{LISN} in Fig. 2.3(b)) is almost constant in the frequency range of interest. This helps us to make sure that the measured data at one site correlates with the measurement at the other sites.

The noise currents are decomposed into common-mode and differential-mode currents. Differential mode currents flow between neutral and phase conductors whereas common mode currents flow through the phase and neutral conductors, and take ground wire as the return path (see Fig. 2.4). Measured phase and neutral noise

currents can be rewritten as:

$$I_P = I_{cm} + I_{dm} \tag{2.1}$$

$$I_N = I_{cm} - I_{dm} \tag{2.2}$$

where I_{cm} and I_{dm} denote for common mode and differential mode currents respectively, depicted by the dashed and solid lines in Fig. 2.4. I_P and I_N represent the current flowing in phase and neutral lines respectively. That gives:

$$I_{cm} = \frac{1}{2}(I_P + I_N) \tag{2.3}$$

$$I_{dm} = \frac{1}{2}(I_P - I_N) \tag{2.4}$$

Differential mode currents are generated by the normal operation of the converter. In ideal conditions, no differential mode noise should exist. However, in the real world where components function differently, some differential mode noise current flow between the phase and neutral lines of the power cord. Common mode currents are produced due to parasitic capacitors of the system that induce current on the ground wire.

Electromagnetic quantities are voltage and current (in volts and amperes) for conducted emission, and electric and magnetic field (in volts per meter and amperes per meter) for radiated emission. One common issue is the wide range of measured data. For example, measured conducted noise emission can range between 1 μV and 10 V, that gives a range of 10^7 volts. EMC limits are normally expressed in decibels as shown in Fig. 2.2. Decibels are capable of compressing the data range. So the range of 10^7 is equal to 140 dB. Decibels are the ratio of two quantities. Conducted

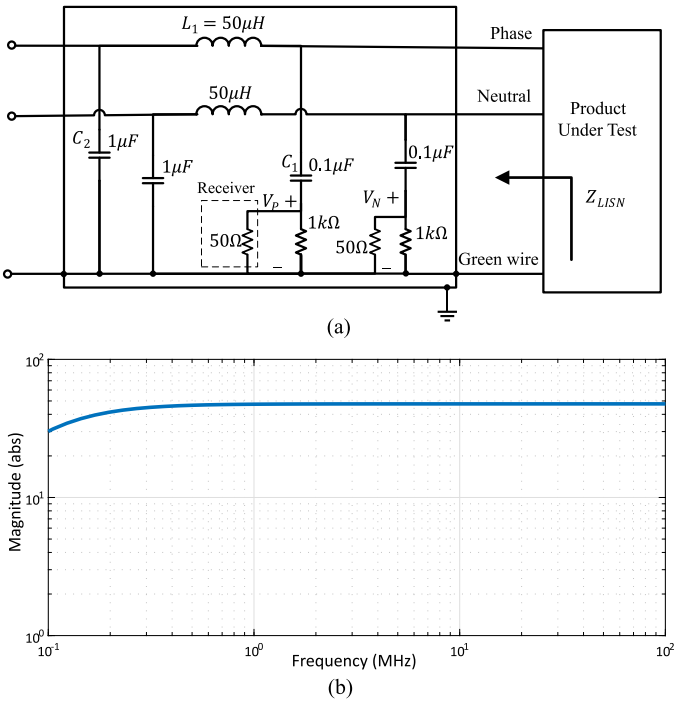

Figure 2.3: Line impedance stabilization network(LISN), (a) Schematics (b) Impedance looking into LISN seen by EUT.

emission voltage is expressed relative to $1\mu V$ as below:

$$dB\mu V \equiv 20\log_{10}(\frac{V}{1\mu v}) = 20\log_{10}^{V} - 20\log_{10}^{1\mu v} = 20\log_{10}^{V} + 120 \quad (2.5)$$

2.3 Overview of EMI modeling

A comprehensive model is required for EMI analysis and prediction. The available modeling techniques of different EMI aspects, with more emphasis on conducted emission, are presented in the following. Readers can refer to textbooks [8] and [3] where EMC fundamentals are well explained. A more mathematical approach is taken in [8], whereas a more application-based approach is adopted in [3].

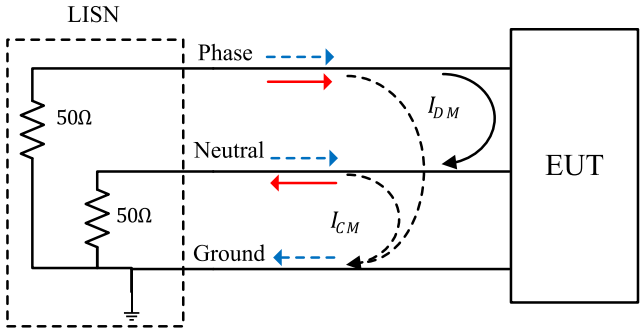

Figure 2.4: Common mode and differential mode currents.

2.3.1 Signal integrity and cross-talk

Signal integrity and crosstalk are the main issues regarding the self interference aspect of electromagnetic compatibility. Signal integrity is related to ensuring that a signal is not damaged during the transmission throughout the interconnects. As the clock frequency and speed of data transfer increase, interconnect conductors have more effect on signal transmission. Assuming the speed of data transmission in a line is equal to the propagation speed, v, the required time for data transmission from one end to the other is:

$$T_D = \frac{L}{v} \tag{2.6}$$

where L is the length of the transmission line. For example, the time delay of transmitted data in a pair of conductors in free space is equal to $\frac{1}{v} = \sqrt{\mu_0 \epsilon_0} = 3.33 ns/m$. That means it takes 3.33 ns to transmit data from one end to another in a one-meter length conductor in free space. Although this time may seem insignificant, rise/fall times of digital signals are very short (in the range of few hundred pico seconds) in modern digital boards. Signal integrity issues are negligible for a short transmission line where the wavelength is comparable to the length of the transmission line. Ringing, ground bounce, impedance mismatch and signal attenuation are main issues

associated with signal integrity.

Crosstalk refers to the electromagnetic coupling between wires and nearby traces of a printed circuit board (PCB). Crosstalk and signal integrity issues are among the most difficult problems to address. They should be considered in a PCB design where traces are in close proximity, and high-speed switching is common. EMC issues related to PCB design are reviewed in [9]. EMI topics in PCB's are classified as: traces, cables, grounding tips and circuit configuration. Susceptibility, emission and crosstalk issues are studied for each category, and many references are provided [10, 11, 12]. Under circuit configuration category, switched mode power supplies and electromagnetically compatible components are studied. PCB simulation and modeling techniques are reviewed in [10, 11, 12] where more recent structures are studied in terms of electromagnetic compatibility and signal integrity.

Signal integrity and cross talk issues should be considered for the control stage design, including the control algorithm and control board design. Since this chapter targets the conducted emission modeling of power converters, the issues associated with control board design are not investigated. However, the effect of the control algorithm is reflected in the switching waveforms as the main source of conducted emissions.

2.3.2 Conducted emissions

Conducted emission modeling techniques can be divided into two categories: (i) behavioral modeling and (ii) detailed modeling. Behavioral modeling is a black box technique that uses multi-port networks with independent sources to model power converters. Derived equivalent circuit is then employed for the prediction of CM

and DM noise current. Once the equivalent network is determined, one can obtain predetermined parameters through a set of measurements. CM and DM noises can be modeled either separately or together considering the mixed mode noises. They mostly rely on experimental measurements to identify model parameters (impedance and sources). The behavioral modeling techniques are more suitable for system level studies. On the other hand, detailed modeling approach considers the features of the circuit elements. The detailed modeling, more elaborated in the section 2.3.2, applies a device-based approach. Equivalent circuit approach is a more simplified form of detailed modeling. Engineers may also combine the behavioral and detailed modeling techniques. Fig. 2.5 summarizes how the conducted EMI modeling methods are classified.

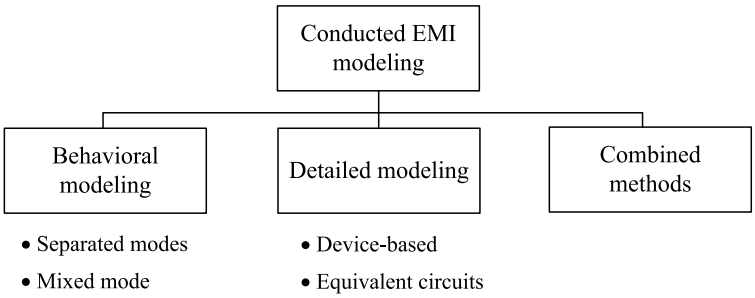

Figure 2.5: Classification of conducted EMI modeling techniques.

Behavioral modeling

An equivalent Thevenin source was first proposed in [13] to model the behavior of a single IGBT switch for EMI prediction. A Thevenin source is implemented to model the IGBT package as the noise source and a two port impedance network to separately model the propagation path as shown in Fig. 2.6. Propagation paths are usually different for DM and CM. The propagation path impedance matrix is

measured by an impedance analyzer. Current and voltage are measured at the LISN port (V_1, I_1) and using (2.7), V_2 and I_2 are calculated.

$$\begin{bmatrix} V_1(j\omega) \\ V_2(j\omega) \end{bmatrix} = \begin{bmatrix} Z_{11}(j\omega) & Z_{12}(j\omega) \\ Z_{21}(j\omega) & Z_{22}(j\omega) \end{bmatrix} \begin{bmatrix} I_1(j\omega) \\ I_2(j\omega) \end{bmatrix} \tag{2.7}$$

$$V_2(j\omega) = V_s(j\omega) - Z_s(j\omega)I_2(j\omega) \tag{2.8}$$

Using (2.8), V_s and Z_s of the noise source in Fig. 2.6 can be calculated. However, two sets of equations are required to solve for the desired parameters. The second set of equations is obtained by changing the impedance network. Finally, the obtained equations are solved for the voltage source (V_s) and the source impedance (Z_s). This method is called Thevenin Equivalent Frequency Domain Source Model (TEFSM) and it is expected to provide higher accuracy as compared to other frequency domain source models such as trapezoidal source modeling [14] where the switching waveforms are approximated by a trapezoidal waveform. Identifying impedances in TEFSM is challenging especially at higher frequencies and the accuracy of predicted results is not very high. Moreover, this model is only valid for fixed operating and switching conditions, i.e. one switching event that is assumed to be repeated in every switching period. Therefore, this method is not suitable for dc-ac converters where the pulse width can change in different switching periods.

Based on the TEFSM, a new approach is proposed in [15] to study a dc-ac half-bridge inverter. In a dc-ac converter, the load current changes during a line cycle. In this method, the line cycle is divided into operating zones based on the load currents. Each zone is characterized by the TEFSM of one representative switching event and

the number of switchings in the zone. The conducted EMI noise for the entire operating cycle is obtained by superimposing the TEFSM models of all operating zones. The accuracy of this method depends on how representative the chosen pulse is for the rest of the pulses in the zone.

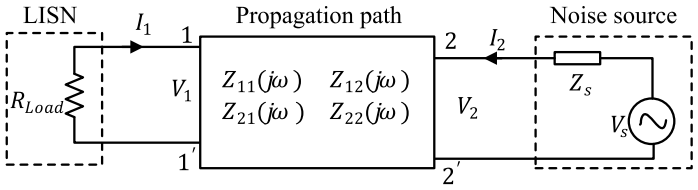

Figure 2.6: Thevenin equivalent EMI noise emission model for a single IGBT [13].

In TEFSM as shown in Fig. 2.6, DM and CM are separately analyzed. In other words, such modeling approach assumes that CM and DM noises are decoupled. This assumption is not necessarily true for power converters and mode decoupling needs to be investigated. Mode decoupling criterion should be studied particularly in EMI modeling approaches that separately models DM and CM. Due to converter asymmetries, CM noise currents contribute to DM voltage. In order to investigate mode decoupling condition in power converters, analytical expressions are derived for input DM and CM impedances [16] based on the Thevenin/Norton equivalent circuit theory. This method is implemented for EMI filter design in a buck converter [17].

In order to tackle the mode decoupling problem, the terminal model of a single IGBT is extended to phase-leg-based converters which facilitate the analysis of many common converters [18]. An IGBT phase leg is modeled by a three terminal Norton model, as shown in Fig. 2.7. Propagation path is replaced by a muti-port impedance network and the size of impedance matrix depends on the number of phase legs. For a full bridge converter with two phase legs, the impedance network size is 6×6 (excluding ground). This modeling approach is capable of studying CM and DM

emissions together where mixed mode emission is also considered.

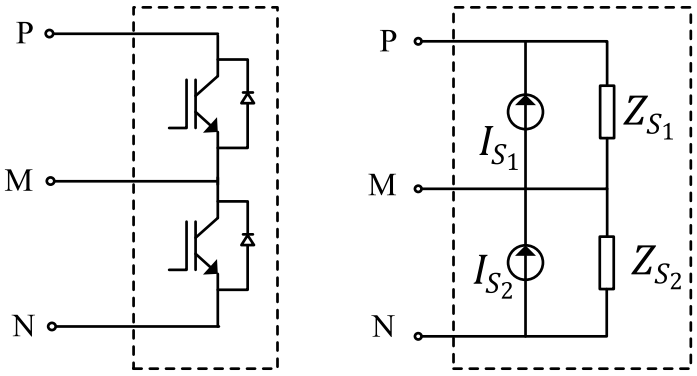

Figure 2.7: Norton equivalent EMI noise emission model of an IGBT phase leg [18].

The methods discussed so far are known as Modular Terminal Behavioral (MTB) modeling. However, the term modular is not accurately used here since the model is modular as long as the switching and operating condition stay the same. Furthermore, as the number of terminals increase, the impedance network gets more complicated leading to a more challenging impedance measurement process.

A more general form of MTB, known as General Terminal Modeling (GTM) is developed in [19]. GTM is an improved version of MTB applicable to multi-port systems. It is more of a black box approach and it has higher accuracy especially at high frequencies. Compared to MTB, only voltage measurements at the converter terminals are required in GTM to identify the equivalent network parameters. Hence, the challenges with the impedance network measurements (e.g. measurement noise, high frequency parasitic capacitors) are eliminated. In GTM, a pre-determined network of three impedances along with two current sources is employed to model any three-terminal system (including ground wire) as shown in Fig. 2.8. Compared to the Thevenin and Norton equivalent circuits with two unknowns in Fig. 2.6 and Fig. 2.7, respectively, five parameters should be identified in the generalized three-terminal

equivalent circuit in Fig. 2.8. This equivalent circuit is the simplest network that uniquely defines a three-terminal system. For this purpose, three sets of measurements are conducted: one for the nominal case and two for the attenuated cases which are obtained by manipulating the system impedances. These measurements provide six equations that are solved for five unknowns. GTM has been applied to buck type converters in [20] and [21] for dc load currents. Current sources of GTM model can be replaced by voltage sources as well [22].

GTM appears to be simpler to understand and apply for parameter identification as compared to MTB. However, one cannot obtain any information about the EMI production and propagation means with GTM since the converter and the load are modeled at the input terminals. The whole model needs to be recalculated for any changes in the converter impedance and operating or switching conditions.

For common-mode current prediction, un-terminated behavioral modeling has been applied to address the aforementioned limitations[23, 24, 25, 26]. This method is capable of predicting CM emission for changes in the load side. A π equivalent circuit is derived to model the motor drive only for CM. However, terminated modeling is still implemented for DM modeling [27],[28] where the converter is modeled at the input side. The terminated behavioral modeling can be applied to mixed mode EMI analysis [29],[30]. The three terminal behavior model of the inverter is derived from the detailed model of the system in [30].

Behavioral methods benefit from simplicity, fast derivation and they are independent of the system configurations. However, they have certain disadvantages. For instance, behavioral modeling methods require standard measurement setup for each operating point. They provide no information about the behavior of the internal

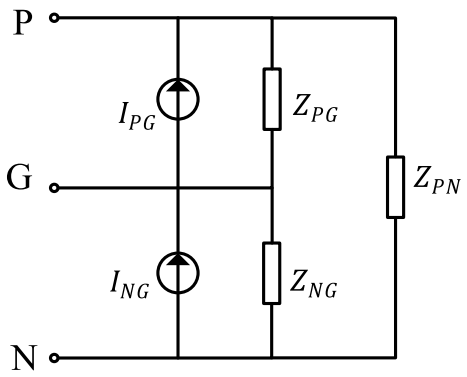

Figure 2.8: Generalized three-terminal equivalent circuit [19].

components. Parameter identification is required in behavioral modeling methods, which can be challenging especially at high frequencies.

Detailed modeling

Detailed modeling techniques employ a device-based approach. Models of circuit components are obtained with physics-based modeling and all the parasitic components are considered [31, 32, 33, 34, 35, 36, 37, 38]. Detailed modeling technique is the most versatile solution to EMI analysis. The main advantage of this method is scalability and adaptability. Once the lumped circuit model of each component is obtained, one can apply each of them in any configuration. Furthermore, parametric analysis is more accessible in this method. One major drawback of detailed modeling is that physics-based model of the components is required which is not always available. The lumped circuit models can get complex as the number of elements increase, and a powerful computer system is required for simulations. This approach seems more suitable to mitigate possible EMI issues at the design stage.

In order to tackle the model extraction limitations, some simplifications are applied to develop more robust models and reduce the complexity. In the equivalent

circuit approach, switching devices, as the main sources of EMI noises, are usually modeled as square- or trapezoidal-shape voltage sources [39, 40, 41, 42, 43, 44]. Although this assumption is reasonable in many EMI studies, the actual physics-based models are required for higher accuracy. State variable approach is implemented in [45] for faster calculation of steady state conducted emission of a buck converter at the expense of losing accuracy.

More analytical approaches have also been presented in the literature. A combined approach is taken based on experimental measurements and modeling of CM circuit in [46] and [47]. Different parts of a variable speed drive are represented by a chain of two port impedance matrices in series. Although this approach enables CM current measurement in various points of the system, the prediction results is not accurate enough at high frequencies due to impedance measurement limitations and also the mode coupling effects.

Although simplified lumped circuit models are capable of predicting the CM and DM noises, they are time consuming especially for parametric analysis. Frequency domain analysis on the other hand provide us with a much faster analysis tool. In the next section, modeling techniques for main components of inverter-fed motor drive system is presented. Then in section IV frequency domain and time domain analysis are discussed in more detail.

2.4 Parasitic components

In a power converter, high dv/dt induced by fast switching of switching devices initiate common mode and differential mode conducted emissions through parasitic elements of the system. Identifying the main mechanism of CM and DM noise production

and propagation throughout the system is essential for analysis and prediction of conducted noise. The detailed modeling discussed in Section III requires physics based modeling of the whole system. The most important parasitic elements in an inverter-fed motor system are shown in Fig. 2.9.

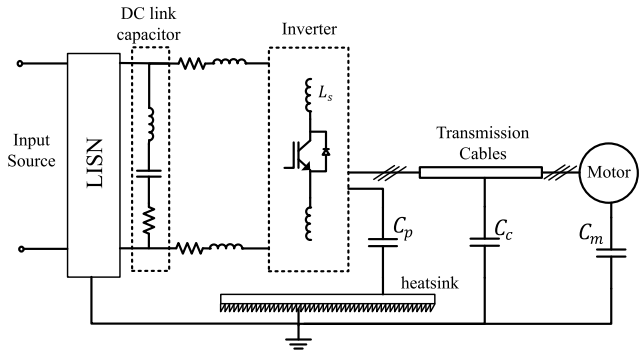

Figure 2.9: Motor drive system including dominant stray components.

Switching waveforms with short rising and falling time induce common mode current in stray capacitors of the system to the ground. The most dominant stray capacitors conducting CM current are the capacitor between motor enclosure to the ground (C_m), cable shielding to the ground (C_c) and between the switching device and heat sink which is normally grounded (C_p). The stray inductance of the dc bus bar, connecting wires and leads, and the dc link capacitor impedance are significant in both DM and CM noise production process. In the following, the most common modeling techniques for the main components of a motor drive system are discussed.

2.4.1 Bulk capacitor

Capacitors are generally a pair of conducting surfaces separated by an insulating material. In Fig. 2.10, equivalent circuit of an actual capacitor is depicted. Capacitance C is the ideal capacitor, and R_p is the insulation resistance corresponding to the dc

leakage current. The typical value of R_p for low-leakage-current capacitors is more than 100000 Mega-ohms, so this resistor is usually neglected unless there is high leakage current. Heat dissipation within the plates, terminals and all conducting parts are represented by R_s in Fig. 2.10 and it is known as the equivalent series resistance (ESR). L stands for the total inductance of the leads and plates and it is known as the equivalent series inductance (ESL).

Although the capacitor impedance seems to be inversely proportional to the frequency, the ESL part dominates at higher frequencies. The series inductance of the bulk capacitor is one of the essential components contributing to DM current production. In the case of an ideal dc-link capacitor, all the transient ac current is provided by the capacitor. However, in the real system, some part of high-frequency current is supplied by the input source due to the ESL and ESR. Direct impedance measurement and curve fitting can be used to effectively extract the equivalent circuit model of a bulk capacitor model[48, 49, 50].

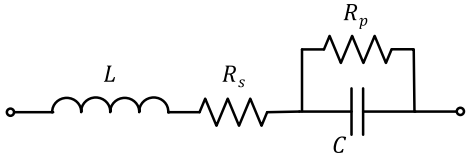

Figure 2.10: Equivalent circuit of a bulk capacitor.

2.4.2 Switching devices

The switching device is the primary source of noise production in power converters. At each switching transition, sharp switching pulses induce CM and DM currents that flow through the propagation path. Therefore, switching device modeling is crucial in EMI analysis. Commercial circuit simulation tools can be used for detailed

modeling of switching devices by considering their nonlinear behavior. A physics-based model developed by Hefner is used in [48] to capture the switching waveform. Hefner's physical IGBT model is also available in Saber simulator. Other physics-based models have been proposed in the literature for IGBT [51, 52, 53, 54, 55] and power MOSFET [56, 57, 58] as the most common switching devices of power converters. SPICE-based simulation tools, PSIM and ANSYS Simplorer are among standard circuit simulation tools. The parameters for these models are extracted from measurements and/or the device datasheet [59, 60].

Power switching devices are available as modules or discrete devices for different applications. For a power module, the parastic inductance of the module need to be considered for more accurate modeling. The stray capacitor between the module and the heatsink is also crucial for CM conducted noise calculation. The heatsink metal plate is normally grounded and the insulating material between the base of the power module and the heatsink is thin enough to provide a good thermal performance. So the stray capacitor, C_p in Fig. 2.9 tend to be relatively large in value. An equivalent circuit of an IGBT phase leg including the interconnect and lead inductances, and the stray capacitances is depicted in Fig. 2.11. The parasitic components of the power module are usually obtained through measurements [48].

Including switching device nonlinearities can increase the complexity of the model and the simulation time. Analytical solutions and approximations have been implemented to address these issues and yield more adoptable solutions. As a more analytical approach, the switching period is broken down into finite sets of time intervals to consider the nonlinear behavior of stray capacitors of a power IGBT [61, 62]. For each interval, the equivalent circuit associated with a switching cycle is solved

for voltage and current equations. The total current and voltage waveforms are built based on the calculated discrete waveforms. In another approach, piece-wise linear IGBT model is applied in [50] and [63] to develop a fast IGBT model, as depicted in Fig. 2.12. The on-state resistance, R_{on} is obtained from the device datasheet and the capacitances are measured using a standard measurement setup. In Fig. 2.12, C_{cg} and C_{eg} represent the stray capacitors between the IGBT collector and emitter to the base plate. The IGBT collector-to-emitter capacitor and the junction capacitance of the anti parallel diode are lumped into C_0.

In terms of analytical solutions, trapezoidal source modeling is another common approximation. Trapezoidal switching voltage waveforms have numerically been synthesized in [64] and [65]. This approach can save sufficient amount of time for the simulations.

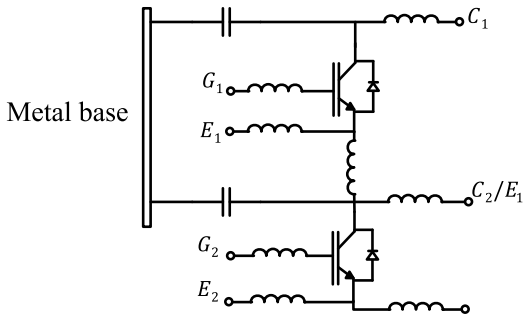

Figure 2.11: Equivalent circuit of an IGBT phase leg with stray capacitances and inductances [48].

2.4.3 Bus bars

Bus bars are large conductors that establish the connection between the electronic components. The bulk capacitor, input dc source, and the switching devices are connected through the bus bar. Usually large currents are transmitted through the

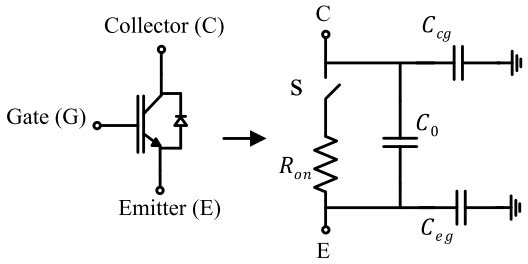

Figure 2.12: Piece-wise linear IGBT model [50].

bus bars. Different criteria need to be considered during bus bar design that have been addressed in [66]. Laminated bus bars are commonly used in power converters for a wide variety of applications. Fig. 2.13 shows a simple two-layer laminated bus bar. The layers are separated with an insulator. Low stray inductance is desired in a bus bar design, since this can reduce the voltage overshoot across the switching device and suppress the conducted EMI. Thin and flat conductors with large surface area and fewer holes can provide low impedance bus bars. The holes are inevitable because they are required for fixtures and terminals connecting the components. The distance between the conductors should also be minimized to increase the capacitance between the layers and minimize the total stray inductance [67]. A higher stray capacitance helps filtering the high frequency noise.

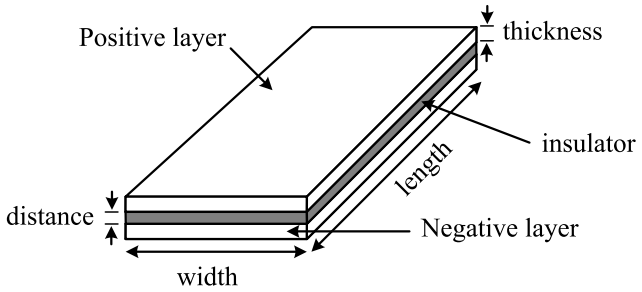

Figure 2.13: A simple laminated bus bar.

High frequency equivalent circuit model of a bus bar can be extracted from direct

measurement or finite element simulation. FEA is generally applied for bus bar parameter extraction [67]; however, measurement-based methods have also been applied in the literature [48].

2.4.4 Motors

Electric machines are normally inductive in low frequency range. Low frequency behavior of electrical machines are well studied in the literature. For instance, the IEEE standard 112 establishes the test procedures and parameters for low frequency T-equivalent model of a poly-phase induction machine. However, high frequency model of a motor is required for EMI analysis. At higher frequencies, terminal behavior of electric machines is more capacitive. Stray capacitance between the motor winding and the motor enclosure is the dominant impedance. Although, physics-based approaches can be employed to derive an accurate model of electrical machines, measurement-based methods are usually employed. The main limitations of physics-based methods are the required design details and the complex structure of an electric machine. Therefore, impedance measurement is normally performed to derive the high-frequency model of electrical machines. Different approaches are proposed to represent the high-frequency model and they can be classified mainly as distributed and lumped parameter models.

A 3-phase induction motor model is proposed in [68] to model the motor behavior over a wide range of frequencies. In this model, the distribution model of the stator winding is integrated into the existing standard low-frequency model. In [69] the parameter extraction methods are discussed and the impacts of magnetic core

selection, parasitic interturn, and winding-to-frame capacitors are investigated. Distributed network of impedances is another method for electric motor modeling and it can be separately used for the high-frequency model in parallel with the low-frequency model. These models are separated by a resonant circuit [70]. In another approach, multistage RLC circuits are used to represent the behavior of any three-phase electric machine. The effect of phase coupling has been taken into account [71] and the model has been applied to an induction and a synchronous machine.

A lumped circuit model can also efficiently model the high-frequency behavior of electrical machines. A simple per-phase lumped-circuit high-frequency model of an induction motor is shown in Fig. 2.14. The model parameters have physical meanings. R_{g1}, C_{g1}, R_{g2} and C_{g2} represent the parasitic resistance and capacitance between the stator winding/ stator neutral and the motor frame, L_d describes the stator winding leakage inductance and R_e shows the high-frequency iron loss of the stator winding. There are different high frequency equivalent circuits proposed in the literature [72, 73, 74].

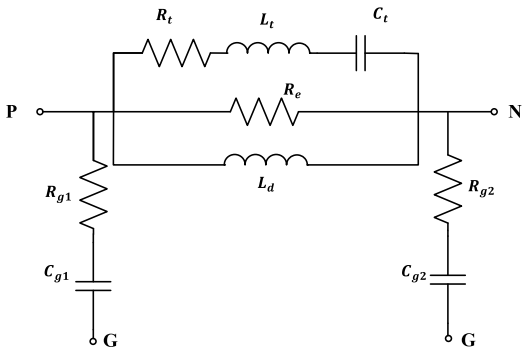

Figure 2.14: High frequency per phase model for an induction motor [75].

2.4.5 Cables

Available modeling techniques for cables can be categorized as direct impedance measurements, finite element tools, and analytical calculations. According to the required level of accuracy and available tools, the most convenient method could be used. Similar to motor modeling, both distributed and lumped circuit models can be used for cable modeling. Distributed parameter model is more suitable for long cables where a number of series identical RLC sections are connected together [75]. Based on the length of the feeding cable, required level of accuracy, and computation capabilities, appropriate number of sections could be chosen for the modeling of a long cable. In [76], the long cable is modeled by twenty π segments shown in Fig. 2.15. Series R and L components are associated with the short circuit characteristic and C component represents the open circuit impedance characteristics. RL and RC ladder networks have been employed to model the distributed impedance of a long cable in [77]. A π representation of a four terminal cable, three phase lines and one shield, have been used in [78] where Laplace elements are used instead of RLC lumped elements. Cable admittance matrix is first obtained by high frequency measurements. Then, numerical fitting algorithms are applied to identify the analytical rational function. The extracted rational function can be represented by π subcircuits of either RLC lumped elements or Laplace elements [79]. As the number of computation cells builds up for longer cables, the computation burden increases. A reduced frequency dependent model of cable is proposed based on the per-unit-length parameters[80]. Finite element simulation tools are also capable of extracting model parameters of a cable over a wide range of frequencies [81].

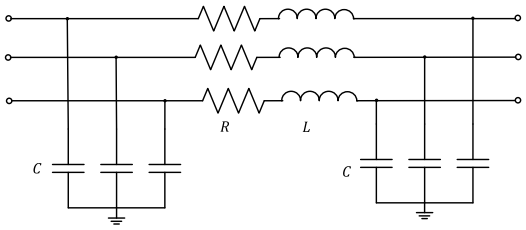

Figure 2.15: Per section equivalent circuit for modeling a long cable [76].

2.5 Simulation methodologies

Regardless of the modeling technique, conducted emissions need to comply with the legal requirements, which are specified in the frequency domain (see Fig. 2.2). Simulation methods can be employed under either time domain or frequency domain analysis [82]. Time domain and frequency domain signals are related by the Fourier transform. Switching devices, as the main noise sources in power electronic devices, are simplified as square/trapezoidal shape voltage/current sources. For a trapezoidal waveform with symmetric rise and fall time ($t_r = t_f$), one-sided Fourier expansion coefficients (representing the magnitude of n^{th} harmonic) are presented as:

$$|C_n| = 2AD\left|\frac{sin(n\pi D)}{n\pi D}\right|\left|\frac{sin(n\pi t_r/T)}{n\pi t_r/T}\right| \tag{2.9}$$

where A, D and T are the amplitude, duty cycle, and the period of the waveform, respectively. Although the harmonic spectrum exists only at discreet frequencies, the spectral envelope is obtained by replacing $f = n/T$:

$$Envelope = 2AD\left|\frac{sin(\pi\tau f)}{\pi\tau f}\right|\left|\frac{sin(\pi\tau_r f)}{\pi\tau_r f}\right| \tag{2.10}$$

where $\tau = DT$. The spectral bounds are effectively used to extract more intuitive information from the harmonic spectra and study the effect of rising/falling time and pulse width. In order to generate the bounds, logarithm of the envelope is calculated:

$$\begin{aligned} 20log_{10}^{(envelope)} = 20log_{10}(2AD) + 20log_{10}(\Big|\frac{sin(\pi\tau f)}{\pi\tau f}\Big|) \\ +20log_{10}(\Big|\frac{sin(\pi\tau_r f)}{\pi\tau_r f}\Big|) \end{aligned} \tag{2.11}$$

Fig. 2.16 shows the harmonic spectrum of a trapezoidal waveform. The first term in (2.11) has a constant value with 0 $dB/decade$ slope. The next two terms have two asymptotes with -20 $dB/decade$ slopes. This means that the magnitude drops by 20 dB per each decade of frequency (a ratio of 10 between two frequencies). As shown in Fig. 2.16, the asymptote for the second term in (2.11) appears at point $f_1 = 1/\pi\tau$ and the last asymptote appears at $f_2 = 1/\pi\tau_r$. The resultant asymptote is the sum of the these asymptotes. So, the harmonic spectrum in Fig. 2.16(b) starts with 0 $dB/decade$ segment with value of $2A\tau/T$ up to the first breakpoint $f_1 = 1/\pi\tau$. The value drops in the second segment with the slope of -20 $dB/decade$ up to $f_2 = 1/\pi\tau_r$. Beyond this point, the magnitude drops by the slope of -40 $dB/decade$. Fig. 2.16 describes how fast the short rise and fall times increase the bandwidth of the noise sources, which results in higher EMI noises at high frequencies. An example of a trapezoidal signal with 10 percent duty cycle, a magnitude of 200 volts, switching frequency of 10 kHz, and the rise and fall times of 200 ns is depicted in Fig. 2.17. The solid line is the calculated asymptote based on the trapezoidal waveform bounds in (2.11). The first segment has the starting value of $E = 20log(2 \times 200 \times 0.1) = 32$. The break points are $f_1 = \frac{1}{\pi \times 1e-5} = 31.8kHz$ and $f_2 = \frac{1}{\pi \times 200e-9} = 1.6MHz$, respectively. The

dots indicate the harmonic spectrum of the signal and their values are multiples of the switching frequency, 10 kHz. The calculated asymptotes shows that they enable calculating the harmonic spectral bounds.

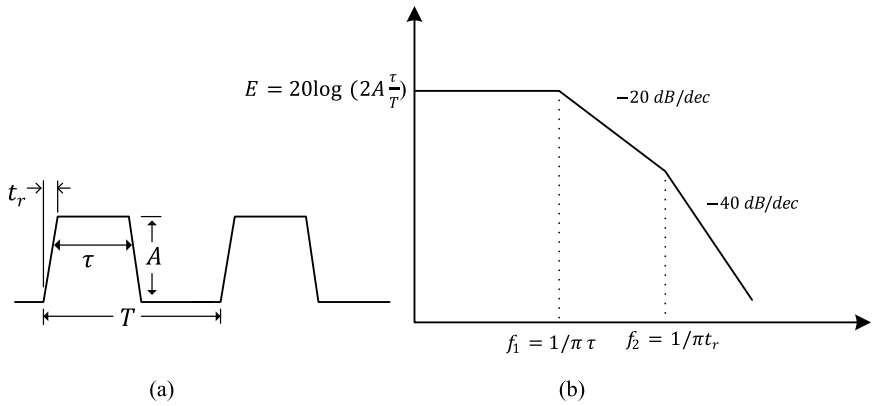

Figure 2.16: (a) Trapezoidal waveform and (b) the bounds on its harmonic spectrum.

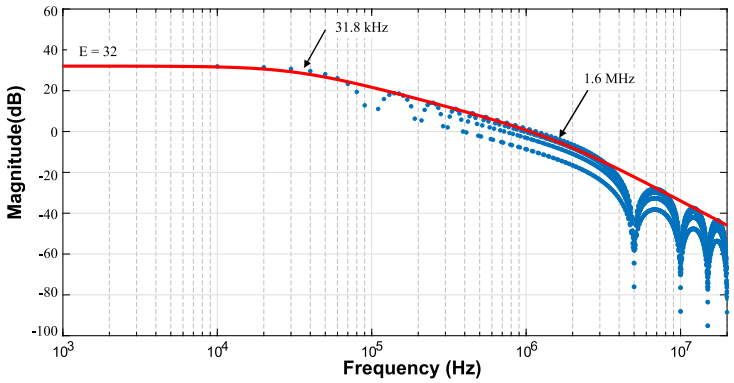

Figure 2.17: Discreet harmonic spectrum and the spectral bounds for a trapezoidal signal with $D = 0.1$, $A = 200$, $f_{sw} = 10kHz$, $t_r = 200ns$.

Time domain analysis followed by Fourier transform is a promising method for EMI analysis and prediction. Time domain analysis can consider the non-linearity of the system if the actual physics-based model of the components, considering the stray elements, are used. However, a high frequency range should be analyzed for

conducted emissions and this limits the required time step to small values [83]. The complexity of the system and the small time step along with the required simulation time to reach to the steady state make the time domain analysis time consuming. On the other hand, frequency domain analysis substantially reduces computational efforts and can be used as a handful design tool. However, this approach requires a fair knowledge of noise production mechanism and propagation paths.

Most measurement-based behavioral modeling techniques are analyzed in the frequency domain. Many simplifications for detailed modeling, discussed in Section IV are also applicable to the frequency domain analysis. In the frequency domain, CM and DM emissions are usually studied separately. Different equivalent circuits are derived for each mode based on the identified noise sources and propagation paths. Then, equivalent circuits are analyzed providing more insights about the noise generation. However, mode decoupling criterion should also be taken into consideration which is closely related to the balance degree of the converter. The converter balance is one of the crucial factors to minimize mixed mode noises. In a balanced circuit, the signal conductors and the circuits connected to them have the same impedance with respect to the ground. As an example, a conventional buck converter can be considered as unbalanced since the output inductor usually has a large value. Due to this asymmetric nature, another factor comes into play: induced currents due to the heatsink capacitor having different impedance paths. This is referred to as mixed-mode noises or Quasi-CM and is depicted in Fig. 2.18 for a buck converter. In Fig. 2.18, R_1 and R_2 are the LISN resistors, L_o is output inductor of the buck converter, V_s is switching device voltage, C_p is the stray capacitor between the switching device and the heatsink, and $I_1 + I_2$ is the total ground current that is supposed to

be purely CM current. The output inductor, L_o has a large value compared to ESL of the dc capacitor so the I_1 flows through the capacitor, C as shown in Fig. 2.18. Therefore, the currents have different path impedances. This means that they are not truly common mode and they contain both CM and DM components, according to (2.12). In other words, mode decoupling is not satisfied.

$$I_{dm,mm} = \frac{1}{2}(I_1 - I_2) \tag{2.12}$$

Inverter-fed motor drive systems are among the balanced systems that have been studied in recent decades. High frequency parasitic elements of the drive system, including the stray capacitor within the motor winding or between two conductors, the nonlinear capacitance of switching devices, the stray inductance of the dc link capacitor, busbar impedance and reverse recovery current of diodes all contribute to DM EMI emission generation during switching transients. On the other hand, the parasitic capacitors between conducting parts and the system ground form a coupling path for CM conducted emission and conduct the noise back to the power mains. The parasitic capacitance between the baseplate of the power module and the grounded heatsink, stray capacitance of motor winding to the grounded frame, and the capacitance between the transmission cables and the ground are the dominant CM coupling paths. In a three-phase motor drive, the switched system is not symmetric with respect to the input power mains (or LISN) during the switching transitions. This leads to mixed mode EMI emissions. The mechanisms of conducted emission generation in a PWM inverter induction motor drive have been investigated in [65] and [70]. The dominant CM and DM noise generation mechanisms are identified and modeled in the first part [70] and a detailed modeling approach was implemented. In

the second part [65], the frequency domain equivalent circuits are proposed based on the insight from the results from the first part. This two-part research indicates how time-domain and frequency-domain modeling approaches are related.

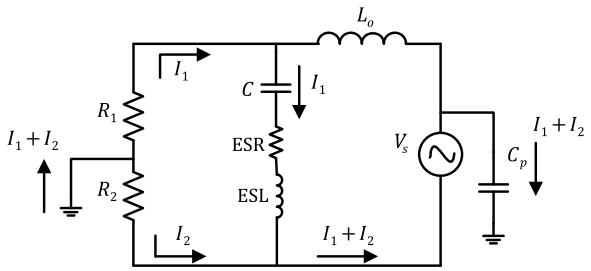

Figure 2.18: CM current paths in a buck converter.

The objective of EMI modeling is to develop a good understanding of how conducted emissions are generated, how they propagate within the converter, and how to predict the level of the disturbance they cause. However, the design may need further solutions to meet the legal requirements. EMI suppression methods could be applied: 1) at the noise source (the generation stage) and/or 2) along the transmission path [84, 85]. Solutions related to noise source can be further categorized as:

- switching modulation schemes such as random, chaotic and variable frequency modulations: switching frequency spectrum is spread over a wide range of frequencies [86, 87, 88]

- snubbers, soft-switching solutions and gate driver modifications [89, 90, 91, 92, 93]: EMI noise level is controlled by shaping the switching voltage and current

- component selection and circuit topology [94, 95, 96]: semiconductor technology and the circuit topology are optimized for emission reduction considering other design requirements

The mitigation techniques along the propagation path can be implemented by external solutions including shielding, active, passive, and hybrid filters [97, 98, 99] or by modifying the circuit design and layout.

2.6 Summary

A comprehensive review of conducted emission techniques, along with the fundamentals of electromagnetic compatibility, is presented in this chapter. Generally, modeling methods are classified as behavioral and detailed techniques. Behavioral modeling is more suitable for system level analysis, whereas detailed modeling is more efficient at the design stage. The available modeling techniques and challenges are studied for the main components of an inverter-fed motor drive system. Based on the application, the required level of accuracy, and the available time and tools, a designer can select the most appropriate modeling technique.

Time-domain detailed modeling is a promising approach at the design level for an EMC-integrated design. Frequency domain modeling approach and approximations can be implemented to reduce the computational burden and provide more robust models. As presented in this chapter, the designer needs to identify the main noise production mechanisms to achieve a more accurate model.

Chapter 3

Modeling of Conducted Electromagnetic Emissions for a Three-Phase Inverter Fed Motor Drive

In this chapter, conducted emissions in a three-phase inverter fed motor drive is studied. A physics-based model is derived for each part of the system using a device characterization tool, a finite element analysis tool, and impedance curve fitting tools. An improved universal equivalent circuit is proposed to model the induction motor in the entire frequency range. A balanced approach regarding the accuracy and simplicity of the model is considered through the model extraction. Furthermore, common mode and differential mode emissions are studied, and two equivalent circuits are extracted.

3.1 Introduction

With recent advancements in power electronics, design engineers tend to go for higher switching frequencies and more compact designs. The operation of different electronic systems in close proximity has brought challenges in electromagnetic interference. In the past, post design solutions were common including additional mitigation components and even redesign of the system. In terms of cost and time, it is more effective to consider EMI issues earlier at the design stage. This requires a comprehensive high frequency model of the system.

Two different approaches are usually taken for conduction emissions modeling of power converters: behavioral and detailed modeling. Behavioral modeling techniques implement multi-port networks with independent sources to model the behavior of different parts of the system [24, 25, 20, 17, 22, 19]. Although behavioral modeling approaches often provide simplicity and fast derivation, they mostly rely on standard setup measurements and provide little information on the noise propagation mechanisms. This makes them more suitable for system-level analysis. In detailed modeling methods, system components are individually represented, mainly based on physics-based models. The main advantage of component-based modeling approach is scalability. It enables applying the same component model to various circuits. Parametric analysis is also more applicable to investigate the effect of each component independently. Yet, this approach usually requires more details about the design features and geometry of the circuit. Those details are not always available or accessible, and the model extraction could be time-consuming specially for complex systems. So detailed modeling appears to be a versatile solution to EMI modeling helping the designers to analyze and mitigate the EMI emissions at the design stage.

Many studies have been conducted on the conducted emissions modeling of motor drive systems. Some simplifications have been applied to tackle the model extraction limitations and develop more robust models. For instance, switching devices, as the source of EMI noise, are approximated by square- or trapezoidal-shaped voltage or current sources [39, 43, 40]. However, for more accurate studies, physics-based models are required to capture the nonlinear behavior of the device [37, 36, 33, 31]. In the literature, frequency domain analysis has also been employed for fast EMI modeling [100].

In this study, a three-phase inverter-fed motor drive is modeled by a device-based approach.

3.2 Time domain model

High values of dv/dt induced by the operation of switching devices introduce the main sources of conducted and radiated EMI emissions in power converters. To obtain a detailed model of the intended traction inverter, each component of the system should be modeled individually. Fig. 3.1 displays the overall view of a typical inverter-fed motor drive along with the dominant stray elements. The inverter is directly connected to a dc power supply to focus on the performance of the inverter only. The line impedance stabilization network (LISN) is then connected to the input terminal of the inverter. The inverter consists of a bulk capacitor, dc busbar and the switching modules. A 7.5 hp induction motor is connected to the output of the inverter through transmission cables. In the following, the modeling process of each part is explained in detail.

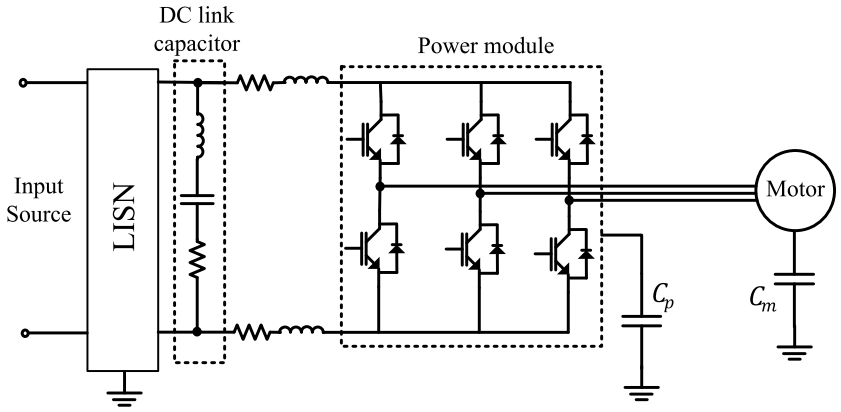

Figure 3.1: Motor drive system including main parasitic elements.

3.2.1 Switching module

Switched voltage and current waveforms with short rise and fall times are the main EMI noise sources. The nonlinear behavior of an IGBT should be considered for more accurate modeling. Circuit simulators such as Saber and SPICE are available for IGBT modeling. Different models have been proposed in the literature for Si and SiC IGBTs [101, 102]. Hefner IGBT model is among the most classical mathematical models implemented in Saber and PSPICE. The model combines a physics-based model of a high-level injection bipolar transistor and an n-channel VDMOSFET (Vertical double Diffused MOSFET). It also considers the nonlinear capacitances between terminals and non-quasi-static effects for capturing the dynamic behaviour of an IGBT [103, 104].

For the drive model analyzed in this chapter, Infineon IGBT power module FF600R06ME3 is used. A device characterization tool provided by Ansys Simplorer is utilized to derive the dynamic model of the IGBT. The characterization tool accepts inputs for various quantities provided in the datasheet and fits the numerical model to the data

and create a dynamic device model over specific range of operating conditions. The user can choose from different levels of abstraction available in the tool. As the level of accuracy increases, the complexity of the model and the calculation time increases. Additionally, convergence problem may arise due to complex calculations.

A double pulse test circuit is used to examine the accuracy of derived dynamic model of the IGBT. Fig. 3.2 shows the test circuit for IGBT characterization. The upper side IGBT is off all the time and the current passes through the antiparallel diode D_1. The double pulse circuit is used to derive the switching characteristics of the lower side transistor T_2. During the first pulse, current is built up to the desired nominal value in the inductive load. At this time, turn-off switching losses and turn-off switching time are measured as the lower side IGBT is turned off. After a short interval, the lower IGBT is turned on so the turn-on switching loss and time are obtained. Switching time and energy measurement criteria are defined by the manufacturer. Following the nominal values of the current, voltage and temperature from the datasheet, the switching characteristics of the IGBT is simulated in Simplorer. The simulation results and the datasheet values are presented in Table 3.1. Three cases are studied: In Case 1, nominal current, voltage and temperature is used. In Case 2, same conditions but a lower current value is tested. In Case 3, the junction temperature of the devices is lower than the nominal case. In Table 3.1, turn-on and turn-off times and energies, denoted as t_{on}, t_{off}, E_{on} and E_{off}, respectively are listed. Some of the information are not available in the datasheet, marked as not applicable (N/A). The switching transients of the IGBT for Case 1 is shown in Fig. 3.3.

The simulation results of the switching characteristics are in agreement with the datasheet values. For further evaluation, the extracted IGBT model is applied in a

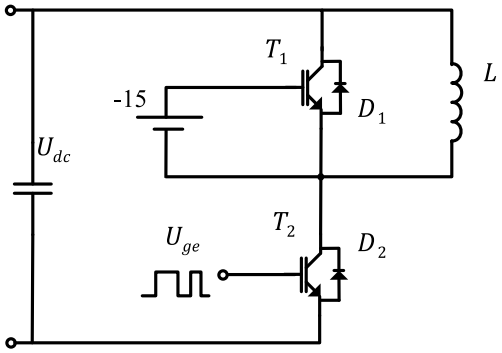

Figure 3.2: Test circuit for IGBT characteristics.

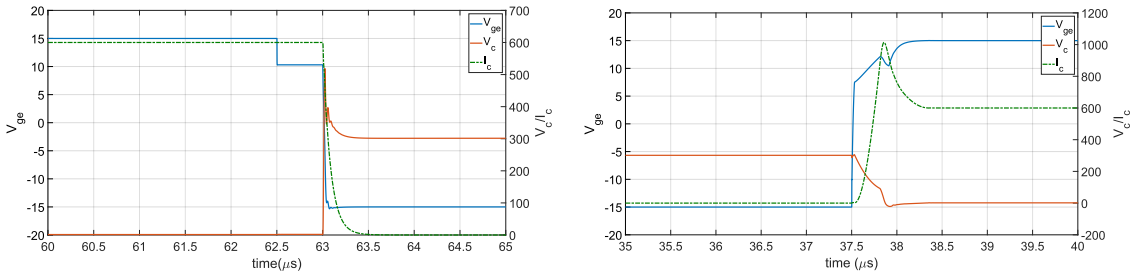

(a) (b)

Figure 3.3: Switching transients of Case 1 a)turn off b)turn on.

Table 3.1: Switching characteristics of the IGBT (Sim: simulation result, Data: datasheet value)

	case1		**case2**		**case3**	
	Sim	***Data***	***Sim***	***Data***	***Sim***	***Data***
$T_{on}(ns)$	225	220	173	190	191	NA
$T_{off}(ns)$	783	785	690	740	727	NA
$E_{on}(mJ)$	9.5	10.5	9	8.9	6.88	7.5
$E_{off}(mJ)$	26.87	26.5	22	21.5	15.9	16

single-phase half-bridge inverter model. Simplorer simulation results are compared to those obtained from the Infineon Online Power Simulation Tool (IPOSIM). The topology, modulation method, output current, dc link voltage, and the junction temperature are the same in both cases. IPOSIM is an Excel-based tool powered by PLECS engine and calculates the conduction and switching power loss of the switches and the diodes. The simulation results of IPOSIM and Simplorer are in good agreement, as presented in Table 3.2.

Table 3.2: Power loss of the single-phase full bridge inverter

	$P_{cond,D}$	$P_{sw,D}$	$P_{cond,T}$	$P_{sw,T}$
IPOSIM	5.8	6.8	22.10	14.00
SIMPLORER	5.5	5.5	24.75	14.25

The stray capacitor capacitance between the power module and the heatsink, C_p in Fig. 3.1, has a significant impact on the common mode emissions. Switched voltage of the IGBTs induce common mode currents in the stray capacitors that flow through the ground.

3D finite element analysis is carried out to extract the stray capacitance of the IGBT module. The construction layers of the IGBT module is depicted in Fig. 3.4. The silicon semiconductor chip is soldered to the direct copper board (DCB) substrate and bond wires form the electrical connection. DCB consists of two layers of copper plates with an insulation layer in between. It conducts current through the copper tracks of the top layer. DCB also provides the electrical insulation between the power components and the cooling medium. The insulation layer is usually ceramic. In this case, the insulation material is Aluminum oxide, Al_2O_3. A copper baseplate layer with 3mm to 8mm thickness is soldered to the DCB to facilitate the power

dissipation to the heatsink. A thin layer of thermal grease is used to make a perfect thermal connection between the module and the heatsink.

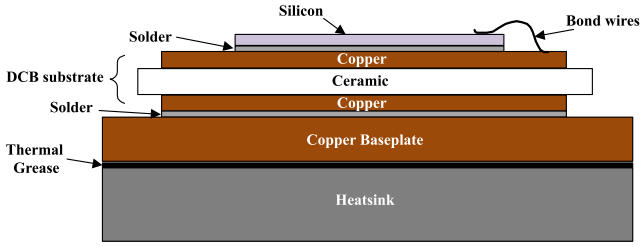

Figure 3.4: Internal construction layers of the IGBT module.

In order to calculate the stray capacitance of the IGBT module, a simplified 3D model of the module, as shown in Fig. 3.5, is developed using the internal construction model of the IGBT model in Fig. 3.4. In this model, bonding wires and silicon chips are neglected. In Fig. 3.5, three copper tracks of DCB are shown on the top. C_1 is connected to the collector of the upper switch and the positive dc input, E_2 is connected to the emitter of the lower switch and the negative dc terminal, and E_1/C_2 is the middle point of the phase leg which connects the emitter of the upper IGBT and the collector of the lower IGBT to the output ac terminal. The bottom layer of DCB and the baseplate are made of copper and soldered together. They are shown as one baseplate in Fig. 3.5. The ceramic insulation layer form three stray capacitances between the top copper tracks and the baseplate. Thermal grease between the baseplate and heatsink, create another stray capacitance that typically has a larger value compared to the other layers. This is mainly because the thermal interface is applied to a larger equivalent surface area and creates a layer and it has a small thickness. Ansys Q3D is used to calculate the stray capacitances listed in Table 3.3.

The total capacitance from each of the top copper tracks to the grounded heatsink,

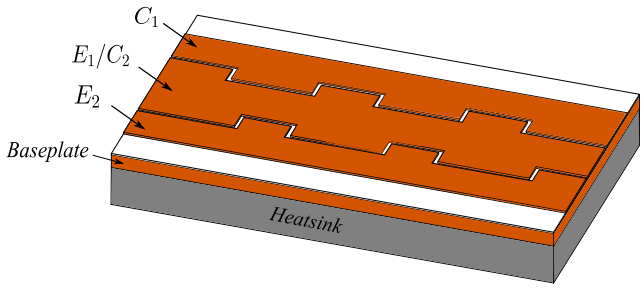

Figure 3.5: 3D simplified model of the IGBT module.

Table 3.3: Stray capacitances of the power module

Capacitance (pF)	E_2	E_1/C_2	C_1	Baseplate	Heatsink
E_2	-	0	0.04	255	0.7
E_1/C_2	0	-	0	441	0.39
C_1	0.04	0	-	292	0.5
Baseplate	255	441	292	-	14.3×10^3
Heatsink	0.7	0.39	0.5	14.3×10^3	-

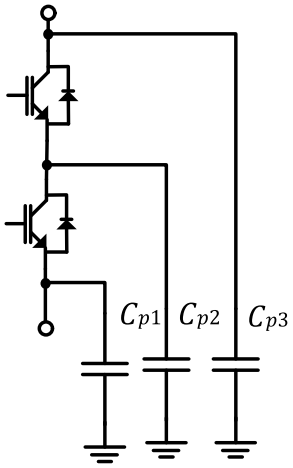

Figure 3.6: Stray capacitances of the power module.

shown as C_{p1}, C_{p2} and C_{p3} in Fig. 3.6, is the equivalent of two stray capacitances in series: (i) the capacitances between the copper tracks and the baseplate (255 pF, 441 pF, 292 pF), and (ii) the capacitances between the baseplate and the heatsink (14.3 nF). Therefore, the total capacitances between the power module and heatsink, C_{p1}, C_{p2} and C_{p3}, are equal to 250 pF, 428 pF, and 286 pF respectively.

The stray capacitances could also be estimated by the equation of parallel plate capacitor given by:

$$C = \epsilon_r \epsilon_0 \frac{A}{d} \tag{3.1}$$

where ϵ_r, ϵ_0 are air permitivity and relative dielectric constant of the insulation material (Al_2O_3), A is the surface area of plate overlap and d is the distance between the conducting layers. Using (3.1), the calculated stray capacitances C_{p1}, C_{p2} and C_{p3} are 267 pF, 422 pF, and 295 pF respectively. The calculation error is less than 7% proving the validity of (3.1) to get the results faster for this application.

3.2.2 Busbars

The power module, input dc source, and the bulk capacitor are connected through a dc busbar that is capable of transmitting large amount of currents. The dc link capacitor requirement, current density limit, and the total impedance are the main factors for a proper busbar design [66]. Conductor plates are tightly coupled together in a laminated busbar resulting in a low impedance profile. The resultant inductance L_{total} is related to the self-inductance of the plates, L_{self1} and L_{self2}, and the mutual inductance between the plates, M as shown in (3.2).

$$L_{total} = L_{self1} + L_{self2} - 2M \tag{3.2}$$

The total stray inductance of the busbar has a proportional impact on the voltage spike across the switches. Therefore, busbars with lower total inductance are desired to limit the voltage spikes and protect the switches. In order to minimize the total inductance, we need to design a pair of busbar plates with low self inductance and high mutual inductance. It has been shown that thin flat plates with large surface areas that are closely coupled together with fewer holes on them provide a low impedance busbar [66]. The holes are commonly used to make the fixture and terminals connecting the components. High coupling can be obtained by reducing the distance between the plates. Moreover, the closer the plates and the coupling between them, the higher the stray capacitance formed between the plates. A higher stray capacitance is also beneficial in terms of EMI suppression as it provides a differential mode filter for high frequency noises.

In this chapter, 3D simulations are conducted in Ansys MAXWELL is used to extract the equivalent model of the busbars. The current flowing through the dc busbar can be represented by the summation of the average of the dc input current and the ac ripple current of the dc link capacitor. At the steady state, the dc component flows between the input terminals and the capacitors while ac component circulates between the dc link capacitor and the power module. The dc and ac components can be calculated using (3.3) and (3.4) where I_{rms} is the rms value of the output phase current, m and $cos\phi$ are the modulation index and power factor, respectively.

$$I_{rms,ripple} = I_{rms}\sqrt{\frac{\sqrt{3}m}{2\pi} + (\frac{2\sqrt{3}m}{\pi} - \frac{9}{8}m^2).cos^2\phi} \tag{3.3}$$

$$I_{avg,in} = \frac{3\sqrt{2}}{4} I_{rms}.m.cos\phi \tag{3.4}$$

The ac current density distribution is displayed in Fig. 3.7 for the maximum input current when the output phase current is equal to 100 Amps. As a rule of thumb for busbar design, the maximum current density should be less than $5A/mm^2$. However, the resulting temperature rise needs to be analyzed, since the thermal limitations is the main requirement.

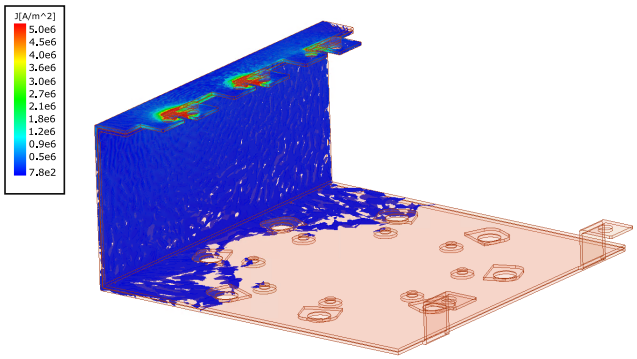

Figure 3.7: AC current density distribution in the dc busbar.

In order to obtain parasitic inductance and resistance of the busbar, positive and negative plates of the busbar are shorted at the capacitor terminals and the ac current is applied at the switching module terminals. The stray resistance and inductance of the busbar are frequency dependent. As the frequency increases, the resistance increases due to skin effect and inductance decreases accordingly. Table 3.4 summarizes the resistance and inductance values of the busbar for different frequencies obtained from the simulation results. The stray capacitance between the positive and negative plates is only a function of the geometry and the material properties of the insulation layer between the plates. In the analyzed case, Amron6 [105] is used as the insulation and the calculated stray capacitance is 4.5nF.

Table 3.4: Stray components of the busbar

	5kHz	10kHz	15kHz	20kHz
R (mΩ)	0.133	0.17	0.2	0.22
L (nH)	15.31	14.59	14.21	14
C (nF)	4.5	4.5	4.5	4.5

3.2.3 Electric machine

IEEE standard 112 T-equivalent circuit can be used for low-frequency modeling of a poly-phase induction machine. However, a high frequency model of motor is required for EMI studies. At lower frequencies, motor behavior is efficiently represented by the inductive impedance of the motor winding while the stray capacitors between the windings and the enclosure dominate at higher frequencies. High frequency equivalent circuit of a motor can be calculated based on the geometry and design details. However, impedance measurement at the motor terminals is commonly implemented for faster derivation. Both distributed and lumped parameter equivalent circuits can be utilized for accurate modeling.

In this thesis, a lumped equivalent circuit approach is employed. The high frequency model shown in Fig. 3.8a is employed to fit the high-frequency measured impedance. Common mode and differential mode impedances are measured using the setups shown in Fig. 3.9. For common mode measurement, three phases are shorted, and the impedance analyzer measures the CM impedance between phases and the frame. For differential mode, the impedance analyzer is placed between one phase and the other two phases connected together. In Fig. 3.8a, R_{g1} and C_{g1} represent the high frequency parasitic impedance between the stator winding and the motor frame. Similarly, R_{g2} and C_{g2} show the parasitic between the neutral and the

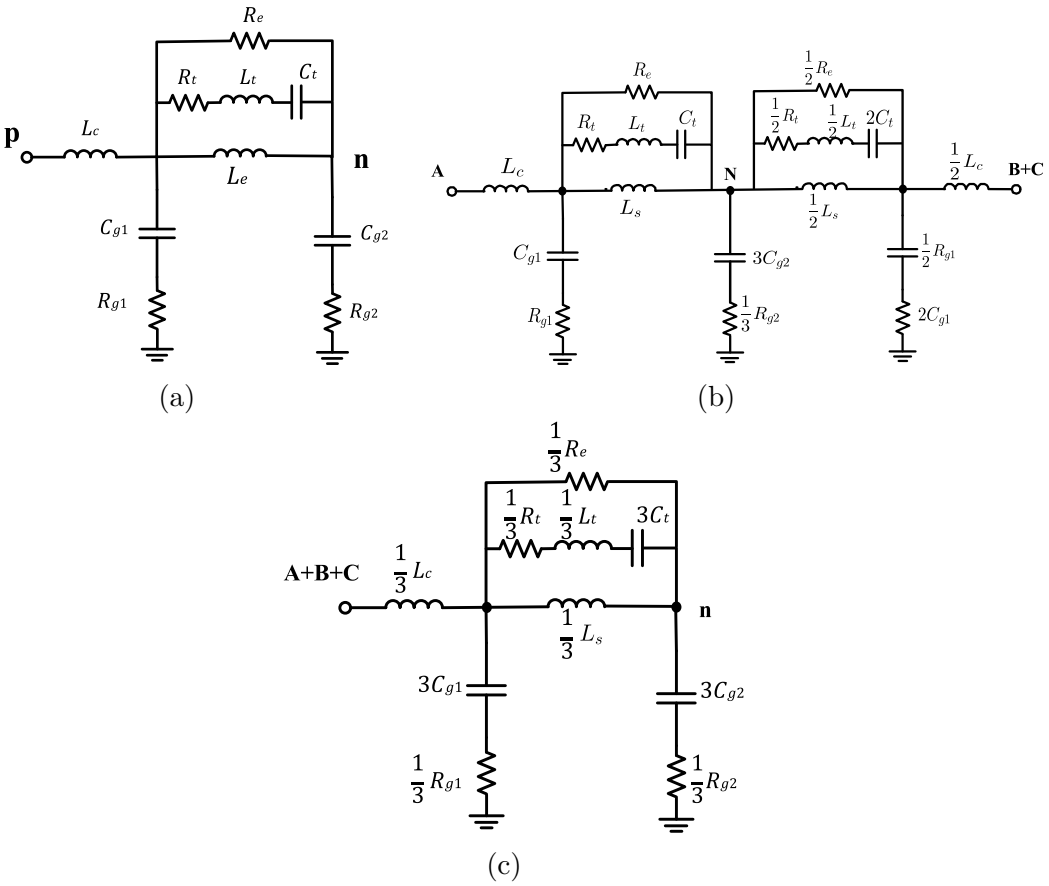

Figure 3.8: high frequency equivalent circuit of the induction motor a) per-phase equivalent circuit b) three-phase differential model c) three-phase common mode model.

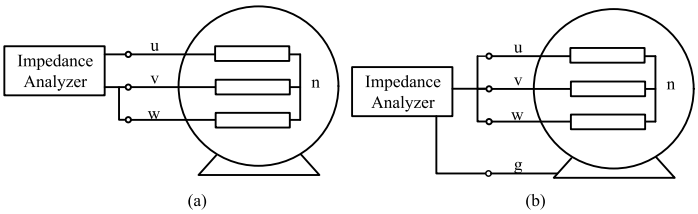

Figure 3.9: Measurement setup for motor impedance measurement a) differential mode b) common mode [73]

motor frame. R_t, L_t and C_t capture the second resonance of the impedance characteristics and represent the interwinding parasitic impedance. L_e models the stator leakage inductance, R_e represents the iron loss, and L_c accounts for the inductance of stator internal feed conductors [106].

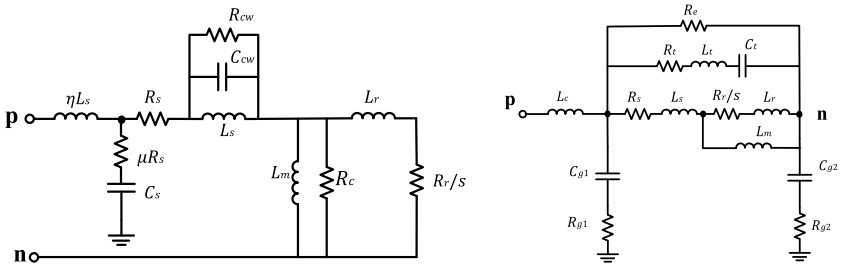

Figure 3.10: Universal per-phase equivalent circuit a) model defined in [68] b) proposed model.

The high frequency model of the motor is not suitable for low frequency studies and should be combined with low frequency models to cover the all frequency ranges. Fig. 3.10a shows a universal induction machine model that combines the low frequency IEEE standard equivalent circuit with the high frequency model [68]. In Fig. 3.10a, R_s, L_s, R_r, L_r, s and L_m denote for stator winding resistance, stator leakage inductance, rotor resistance, rotor leakage inductance, motor slip, and core magnetizing inductance, respectively. In this model, the parameters μ, η and C_s are difficult to express and the second resonance in the differential mode impedance characteristics (see point 2 in Fig. 3.11) is not accurately modeled. Based on the universal equivalent circuit defined in [68] in Fig. 3.10a and the high frequency model in Fig. 3.8, a new improved universal per-phase equivalent is proposed here as shown in Fig. 3.10b. The proposed universal model enjoys the simplicity of the parameter calculation of high frequency model and the generality of the universal model. The parameters of

high frequency model are calculated so that the three-phase DM and CM models (in Fig. 3.8b and Fig. 3.8c) are fit to the measured impedance (see Fig. 3.11) [73]. It is assumed the motor windings are connected in the Y-configuration.

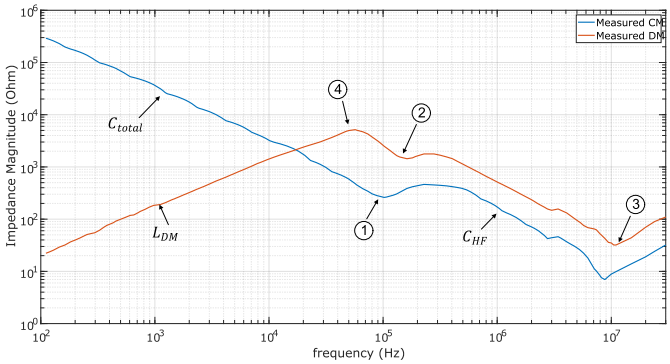

Figure 3.11: Measured CM and DM characteristics.

The measured impedance in Fig. 3.11 are from [73]. C_{total} and C_{HF} are the total and high frequency winding to ground capacitances and are measured from the slopes of the CM impedance. C_{g1} and C_{g2} are calculated based on them ((3.5) and (3.6)). R_{g1} and R_{g2} are obtained from the resonant frequencies of points 1 and 3 in Fig. 3.11. The winding leakage inductance L_s is extracted using both DM and CM characteristics. The iron resistance R_e is calculated from the resonant frequency point 4. C_t is assumed to be one tenth of the total capacitance between single phase winding to the ground. Then, R_t and L_t can be obtained based on the resonant frequency point 2. Finally, L_c is obtained from the resonant frequency point 3.

$$C_{g1} = \frac{1}{3} C_{HF} \tag{3.5}$$

$$C_{g2} = \frac{1}{3}(C_{total} - C_{HF}) \tag{3.6}$$

$$R_{g1} = \frac{2}{3} Z_3 \tag{3.7}$$

$$R_{g2} = 3Z_1 \tag{3.8}$$

$$L_s = L_{CM} + \frac{4}{9} L_{DM} \tag{3.9}$$

$$L_{CM} = \frac{1}{12\pi^2 C_{g2} f_1^2} \tag{3.10}$$

$$R_e = \frac{2}{3} Z_4 \tag{3.11}$$

$$C_t = \frac{1}{10(C_{g1} + C_{g2})} \tag{3.12}$$

$$L_t = \frac{1}{4\pi^2 C_t f_2^2} \tag{3.13}$$

$$R_t = Z_2 \tag{3.14}$$

$$L_c = \frac{2}{3} \frac{3}{8\pi^2 C_{g1} f_3^2} \tag{3.15}$$

Calculated values are used as the initial values of the Genetic Algorithm optimization to minimize the fitting error. Final parameters and motor specifications are listed in Table 3.5. Measured and modeled differential mode and common mode impedance are shown in Fig. 3.12. The rotor impedance has a small effect on the high-frequency performance of the motor. This is demonstrated in Fig. 3.13 where differential mode impedance is depicted for different operating points at different slips.

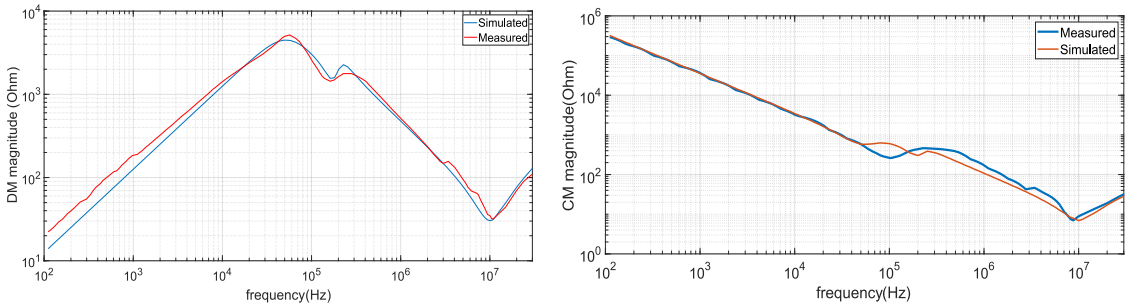

(a) (b)

Figure 3.12: Measured and simulated impedance magnitude a) DM b) CM.

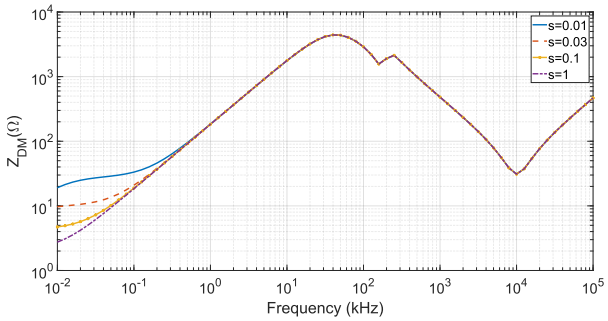

Figure 3.13: Differential mode impedance of the motor for different operating points represented by rotor slip (s).

Table 3.5: Improved universal model parameters and the induction motor specifications

Parameter[a]	Value	Parameter	value
R_s	1.2 Ω	R_e	3 kΩ
L_s	8mH	C_{g1}	492 pF
R_r	0.18 Ω	R_{g1}	20 Ω
L_r	12 mH	C_{g2}	1 nF
L_m	250 mH	R_{g2}	25.57 Ω
C_t	158 pF	L_c	500 nH
R_t	1.98 kΩ	Power	7.5 hp
L_t	5 mH	Poles	2

3.2.4 Capacitor and LISN

Dc link capacitor can be modeled by a stray resistor and an inductor connected in series with the main capacitor, as shown in Fig. 3.14. The equivalent series resistance (ESR), R_s, represents the heat dissipation within the capacitor plates, terminals, and all other conducting parts. The equivalent series inductance (ESL), L_s, represents the total inductance of the leads and conducting parts.

Figure 3.14: Equivalent circuit of the dc link capacitor.

The equivalent circuit of the bulk capacitor can be directly calculated by impedance measurements at the capacitor terminals. The numbers provided in the datasheet is used in the analyzed case. A 500µF ring film capacitor by SBE is used in this application with part number 700D50796-349. The ESR and ESL values of 0.25mΩ and 5nH are used to model the capacitor.

Line impedance stabilization network or LISN is generally used to measure the conducted emissions in the frequency range of 150 kHz to 30 MHz. LISN provides a constant line impedance looking from the inverter into the input ports Z_{LISN} (in Fig. 3.15). Secondly, it blocks and diverts the noises coming from the power means.

The motor is connected to the output of the inverter via short AWG6 wires which have low impedance compared to the induction motor impedance. Therefore, the impedance of the connecting wires is neglected in this study.
[**Although the exact length is unknown to the author, the effect of the wire impedance is negligible.]

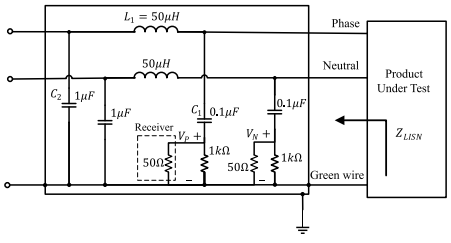

Figure 3.15: Line impedance stabilization network.

3.3 Conducted emissions

Detailed model of the three phase inverter-fed motor drive system is derived by putting together the model of each part, elaborated in the previous section. The motor is running at the speed of 3500 rpm. Input dc voltage source of 300 volts is feeding the inverter directly. Sinusoidal PWM with 10 kHz switching frequency is used. The output frequency is 60 Hz. The output line voltage and motor phase current are shown in Fig. 3.16. The voltages across the LISN resistors are measured to calculate the common mode and differential mode voltages.

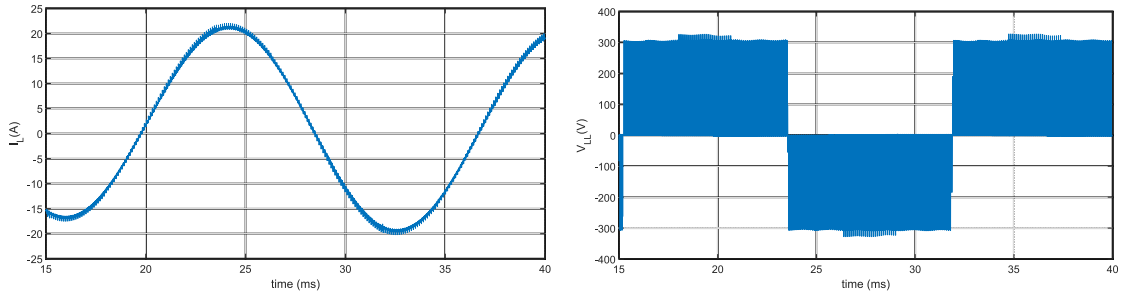

(a) (b)

Figure 3.16: Inverter output a) motor phase current and b) output line voltage.

So far, a time-domain detailed model of the drive system has been derived and simulated (as shown in Fig. 3.1). One major drawback of this model is the small required time step that leads to time-consuming simulation. According to the Nyquist-Shannon sampling theorem, the minimum sampling frequency should be at least twice the maximum frequency of interest. For conducted emissions simulations, 30 MHz is the maximum frequency of interest, resulting in the maximum time step of 16 ns. Frequency domain analysis is a faster approach for EMI modeling. In this approach, based on substitute theorem, switches are replaced by the voltage or current sources, and the rest of the circuit remains the same. This model of the motor drive is shown

in Fig. 3.17. At each phase leg, the upper switch is replaced by a current source whereas the lower switch is replaced by a voltage source. Different combination of noise sources can be used but voltage sources in parallel and noise sources in series should be avoided. The noise sources should have the same time domain waveforms as the original circuit. The frequency-domain model of the noise sources can be calculated by analytical expressions based on Laplace transform, which gets complex for switched waveforms. In some papers, noise sources are approximated by trapezoidal waveforms for simplicity. In the frequency domain model, all noise sources should be combined together to preserve the phase information [107]. Therefore, an equivalent circuit for each mode (CM and DM) is derived in the following. It is assumed that common mode and differential mode noises can be modeled independently i.e. the coupling between them are negligible. Later, the effect of coupling is briefly studied. In order to evaluate the equivalent circuits, noise sources are replaced by their time domain waveforms.

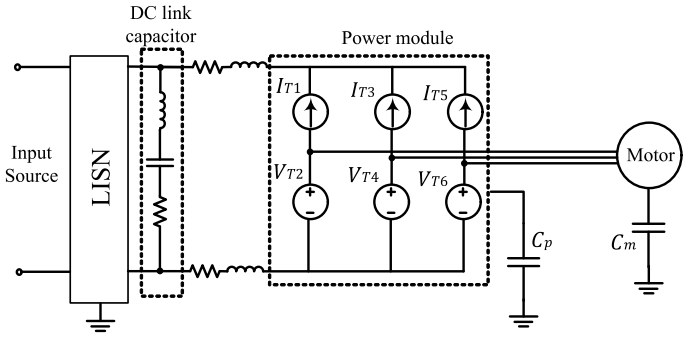

Figure 3.17: Motor drive system where switches are replaced by noise sources.

3.3.1 Common mode

Common mode currents are induced in the stray capacitors of the circuit and flow through the ground. The common mode equivalent circuit of the three-phase motor drive system is shown in Fig. 3.18. All three phases are assumed to be short circuited at the inverter output (a,b,c) since the aim is to find the noise current flowing into the ground wire (g). The common mode equivalent circuit of the motor and cable is placed on the load side and shown as a box in Fig. 3.18. LISN common mode equivalent circuit, normally only the resistor, is put on the input side. Z_b denotes for the busbar impedance and noise source is represented by a voltage source V_s. The total stray capacitance between the three phases of the power module and the ground is summed up together and considered by $3C_p$. C_p is the stray capacitance between the middle point of each phase leg to the ground (C_{p2} in Fig. 3.6). C_{p1} and C_{p2} are not considered since they are connected to the positive and negative busbars and their voltages is almost constant. On the contrary, C_{p2} is connected to the switching node. The voltage of this node switches between positive and negative busbars at each switching transition, which induces major common mode currents in the capacitor C_{p2}. Assuming balanced operation of motor phases, common mode noise source can be expressed as:

$$V_s = \frac{1}{3}[v_{ao} + v_{bo} + v_{co}] \tag{3.16}$$

where v_{ao}, v_{bo} and v_{co} are the phase voltages relative to the dc-link middle point. The spectrum of the common mode conducted emission is the voltage over the LISN resistor (V_{CM}), and is measured at the input side. Based on the derived CM model, the spectrum of V_{CM} is the product of the CM noise source and the propagation path.

It can be expressed as:

$$V_{CM} = V_s \times G_{CM} \tag{3.17}$$

where G_{CM} is the g-parameter of the network and related to propagation path impedance characteristics of the CM equivalent circuit. The characteristics of G_{CM} is shown in Fig. 3.19. The CM noise source (V_s) is replaced by its time domain waveform to assess the derived CM equivalent circuit. The resultant CM emission is shown in Fig. 3.20 along with the time domain results. It can be seen that in most of the frequency range, frequency and time domain results are in good agreement.

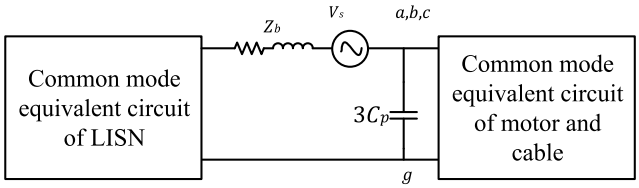

Figure 3.18: CM equivalent circuit of the three-phase motor drive.

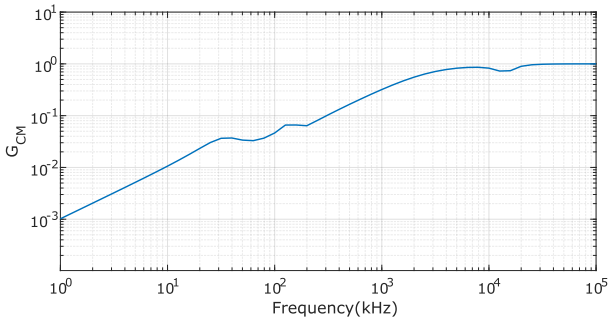

Figure 3.19: CM path g-parameter (G_{CM}) characteristics.

3.3.2 Differential mode

Differential mode current flows in the direction of main current between phase and neutral wires. DM conducted noises are mainly generated due to non-ideal operation

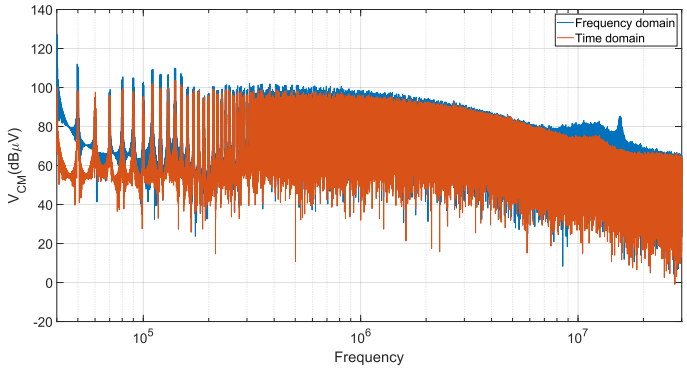

Figure 3.20: CM conducted emissions of the three-phase motor drive.

of components and system unbalances. At high frequencies, ESL of the dc link capacitor dominates, and the high frequency current is shared between the bulk capacitor and the LISN. A general model is displayed in Fig. 3.21 where C_b represents the high frequency stray capacitor between the busbar plates and functions as a differential mode filter. The DM propagation path impedance characteristics is shown in Fig. 3.22. The DM noise source is the sum of current sources of upper switches. The DM noise source (I_s) is replaced by its time domain waveform to assess the derived DM equivalent circuit. The resultant DM emission is shown in Fig. 3.23 along with the time domain results.

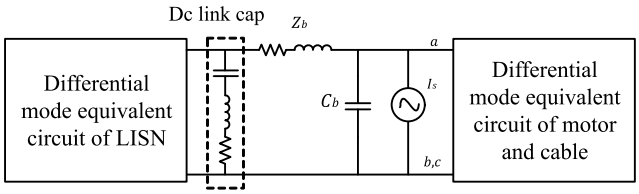

Figure 3.21: DM equivalent circuit of the three-phase motor drive.

It can be seen that in most of the frequency range, there is around a 6 dB difference between the frequency and time domain results for DM emissions. The main reason is the coupling between CM and DM noises, which is not considered in the separated

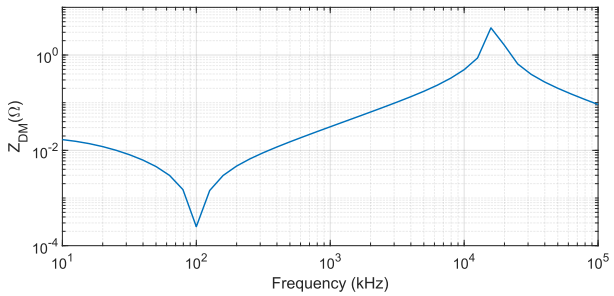

Figure 3.22: DM path impedance characteristics.

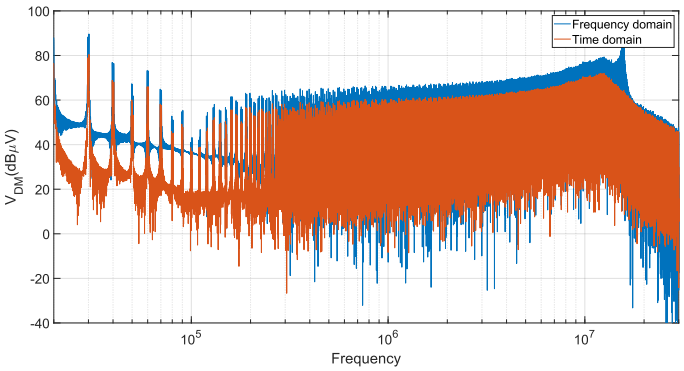

Figure 3.23: DM conducted emissions of the three-phase motor drive.

equivalent circuits. DM noise is a mixture of intrinsic DM noise and mixed-mode noise. Without a ground wire, the measured DM noise is purely intrinsic. However, in the presence of a ground wire, a part of the ground current (or CM noise) contributes to the mixed-mode DM noise. Unbalanced CM currents flowing through the LISN resistors cause a mixed-mode noise. A combined equivalent circuit is used to study the effect of mixed-mode noises, as shown in Fig. 3.24. In this figure, R_1 and R_2 represent the LISN resistors. In order to obtain the MM current, the DM noise source is removed, and the currents flowing in LISN resistors are measured. Then, the DM current is calculated, which is the actual MM current. Next, the calculated MM current is added to the intrinsic DM current, shown in Fig. 3.23. The resultant DM emissions are shown in Fig. 3.25. Considering the effect of MM noise, in most of the frequency range, frequency and time domain results are in good agreement.

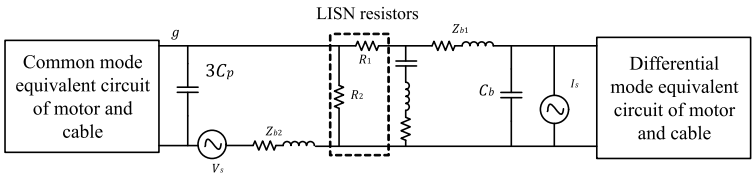

Figure 3.24: Unified equivalent circuit of the motor drive system.

Calculated natural frequencies for each conduction mode, based on the derived equivalent circuits and the simulation results are listed in Table 3.6. It can be seen the extracted equivalent circuits are capable of predicting the conducted emissions and dominant frequencies. Verified equivalent circuits provide an advantageous analysis tool.

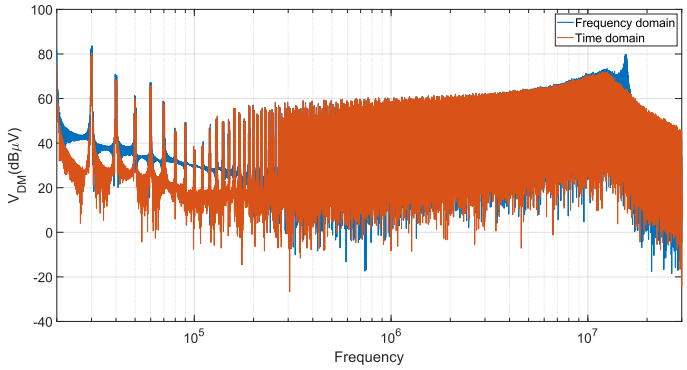

Figure 3.25: DM conducted emissions considering the coupling between CM and DM.

Table 3.6: Natural frequencies of each conduction mode

	Calculated	Simulation
f_{cm1}	125 kHz	132 kHz
f_{cm2}	200 kHz	198 kHz
f_{cm3}	12.5 MHz	11.5 MHz
f_{dm1}	100 kHz	100 kHz
f_{dm2}	15.8 MHz	12.2 MHz

3.4 Summary

A physics-based approach is employed to model a three-phase motor fed inverter drive. Each component is individually modeled considering dominant parasitic components. The IGBT module detailed model is obtained by device characterization tool. The accuracy of the extracted model is verified by a double pulse test circuit and the measured characteristics are in good agreement with datasheet and IPOSIM. Parasitic components of the power module and busbars are extracted by finite element analysis tool. A new universal equivalent circuit is proposed for induction motor modeling. The parameters of the model are easy to calculate and are further optimized by GA. Putting together the detailed model of each part, the conducted emissions of the system is simulated in time domain. Frequency domain is also investigated and common mode and differential mode equivalent circuits are derived. The effect of mixed-mode noise is studied and modeled.

Chapter 4

On the Electromagnetic Compatibility (EMC) Measurement and Testing Procedures for Power Converters

In this chapter, EMC measurement devices and testing procedures are reviewed for power converter applications. The topics discussed here help the reader to obtain an overview of the EMC testing and develop a comprehensive understanding about the EMC measurement device.

4.1 Introduction

Electromagnetic compatibility of power converters is one of the challenging topics emerging in the recent decades. An electromagnetically compatible device does not

introduce significant amount of electromagnetic pollution into the surrounding environment and itself and it is capable of functioning properly in the designated area. EMC is concerned with the generation, transmission, and reception of electromagnetic energy.

Sources of EMC, manmade or natural, generate continuous or transient electromagnetic interference that are transmitted to another device through conduction and/or radiation coupling paths. Sources of continuous EMI including power amplifiers, radars, transmitters, computers, and industrial radio frequency systems emit EM energy over a period of time and usually at a repetitive rate. On the other hand, transient sources of EMI such as electrostatic discharge (ESD), lightning, electromagnetic pulses (EMP), electrical fast transients (EFT), power line faults and surges are released over a short period of time and at unpredictable times. The received energy at the receiving device, may or may not cause major disturbance. Immunity indicates how resistant the device is against the unwanted EMI emission.

EMC standards are legal requirement that are nationally regulated for different type of products. Standards normally define emission limits, acceptable measurement devices, test methods and setups for different categories of devices. EMC standards are represented in four main topics: conducted emission (CE), conducted susceptibility (CS), radiated emission (RE), and radiated susceptibility (RS). Typical transient tests such as ESD, EFT and surges, are usually discussed in a separate section of the standards. EMC compliance test is required for all electronic equipment before marketing.

EMC testing types can be classified as: development testing, model evaluation testing, pre-compliance, and compliance testing. Compliance testing is the last step

of production and formally confirms whether the equipment meet the legal requirement or not. This test is performed in approved test houses. The manufacturers should be prepared for the final official compliance test as it is usually expensive. An EMC failure may cost a lot of time and money to address the EMI issues which may even require a redesign of the product. Pre-compliance tests, performed at the manufacturer's site, can reduce the overall development cost. The more the conditions and equipment are representative of actual compliance testing conditions, the more accurate and reliable the test results would be. A cost-friendly test setup can be built to test a complete subsystem for the prototype. It is more cost effective to address the EMI issues at the earlier stages of a product development. Such approach requires a comprehensive modeling of the system. Some quick tests with the available equipment could facilitate the modeling process. Development testing is performed at the design stage to obtain the characteristics of the specific components such as a cable, a switching device, or an electric motor. Model evaluation testing helps the engineers to assess their modeling approach so that the prediction results are meaningful and accurate.

When it comes to power converters EMC requirements of power converters can be diverse for the wide applications such as appliances, computers, aerospace, automotive, marine, medical, military, industrial installations, power generation and distribution, hybrid and electric vehicles, solar and wind energy conversion, and switched mode power supplies. Special care must be given when designing a product with certified subsystems. Although it might seem probable to manufacture an EMC-compatible device by assembling EMC-approved modules, one needs to consider the effect of emissions adding up [108]. While it is recommended to use EMC certified

modules, the EMC performance of the whole product should be assessed. For instance, LMQ61460-Q1 automotive dc-dc converters from Texas Instrument meet the EMC requirements of Federal Communications Commission (FCC) [109]. The module is can be used in automotive infotainment system or advanced driver assistance systems. The total design compliance should be tested even if all the modules are EMC certified.

This chapter intends to provide an overview of EMC testing and measurement procedures especially for power converters.

4.2 EMC test procedures

In order to achieve a successful compliance test at the first attempt, EMC needs to be considered in different stages of production. At the early stage of design, EMI modeling along with following some practical tips could be beneficial. At this stage, some basic development tests are also advantageous to facilitate the modeling process. Large manufacturers such as Ford, Jaguar and General motors that face tough automotive EMC requirement, perform the EMC design review during the last design evaluation of the product and right before the first or second prototype [110, 111, 112, 113]. It has been shown that reviewing the design requirement right before the manufacturing reduces the design errors and helps to pass the EMC testing at the first time. Once the first prototype is ready, pre-compliance tests can be performed to assess the EMC performance of the equipment. At this point, based on the required level of accuracy and the budget size, companies run the EMC tests at their own site or EMC test labs. The closer the test environment to the standard compliance test arrangements, the more trustful are the test results. The final compliance EMC test

are required before marketing launching the product.

4.2.1 Test plan

The first step for a comprehensive EMC test process is to create a test plan. A test plan defines the EMC requirements based on the application and intended family of standards. For a given application type and the target market, specific test certificates are required. In some cases, such as in Federal Communications Commission (FCC) standards, only emission tests should be passed, and no immunity tests are mandatory. However, immunity tests are required if the equipment is manufactured in or shipped to Europe or Australia. Safety issues may introduce more strict test requirements in military, medical or aerospace applications. Although there is not one standard format, a test plan usually begins with the product description and power supply requirement. The main part indicates a list of product ports along with required test specifications. The test and related standard are described and pass and fail criteria are also distinctly defined. Safety related issues, required software and support tools are mentioned in notes section.

Pass and fail criteria for emission tests, whether conducted or radiated, shows that the emission level of the equipment is below or above a frequency-based certain limit. Fig. 2.2 shows CISPR32 conducted limits for class B products [6]. In case of immunity tests, the equipment is exposed to specific electromagnetic phenomenon and its performance is rated based on a predefined performance criterion. EMC standards define the evaluation criteria, generally in four categories. Criterion A indicates that the device functions normally during and after the immunity test. So, the equipment is totally immune to the applied phenomenon. Criterion B implies that

the performance of the equipment is degraded or stopped during the test but once the EM energy is removed, the device is capable of going back to normal operation without any intervention from outside. Criterion C is similar to criterion B except that the device needs the operator intervention for recovery. In criterion D, the damage to the device is not recoverable. The damage could be a component breakdown, damaged integrated circuit (IC) or permanent loss of data [114, 115]. A sample EMC test plan for immunity requirements is depicted in Table 4.1 [116]. Another useful resource for preparing a test plan is to check out the similar products. Some of the manufacturers provide a list of EMC certifications. Table 4.2 shows a number of EMC certificates for a three-phase solar inverter by SolarEdge [117].

Table 4.1: A sample EMC test plan

Port	**Aspect**	**Frequency range**	**Applicable standard**	**Performance Criteria**	**Note**
Dc power input and output	RF common mode	0.15-80 MHz	EN61000-4-6	A	notes
Ac power input and output	Fast transient	Not applicable	EN61000-4-4	B	notes

Table 4.2: List of EMC certificates of a three-phase solar inverter

STANDARD COMPLIANCE	
Safety	IEC-62103 (EN50178), IEC-62109
Grid Connection Standards	VDE 0126-1-1, VDE-AR-N-4105, AS-4777, G83 / G59
Emissions	IEC61000-6-2, IEC61000-6-3 , IEC61000-3-11, IEC61000-3-12, FCC part15 class B
RoHS	Yes

4.2.2 EMC tests

As discussed in the previous section, the EMC test plan specifies the types of tests the product need to pass. Using the test plan, we would know what to expect at the final compliance test. In this section, some of the most common EMC tests are presented.

Radiated emissions and immunity

Radiated emission test can be performed in either an open area test site (OATS) or a semi-anechoic chamber (SAC). The equipment is placed on a turntable to capture the radiated EMI in different directions. An antenna is also required for EM measurement connected to an EMI receiver for the data analysis and recording. The antenna measures the radiated field strength at various standard distances, typically three, ten and thirty meters away from the equipment. The inside of a SAC is covered with EM absorber material to minimize the signal reflection. Although OATS is the most common radiated emission test site, the measurement errors are higher and the comparison of measurement results at different sites are difficult due to ambient noises. SAC is more expensive but it creates a chance to measure radiated emissions in a cleaner environment [8]. A sample standard for radiated emissions test is FCC part 15, subpart B [5].

In a real world environment, it is highly probable that the equipment is exposed to electromagnetic field such as when operating near a cellphone or an electric motor. Any conducting part of the device can pick up the radiated EM field and this may lead to measurement errors, wireless interference, or even digital logic errors. Radiated immunity ensures that the device is able to function properly at the presence of

such fields. In this test, uniform electric field of various levels, typically 1, 3 and 10 V/m, are applied to the equipment under test (EUT) over a range of frequencies. A power generator, radio frequency (RF) power amplifier and an antenna are required to generate the required electric fields.

Conducted emissions and immunity

This test is carried out to measure the emission conducted back to the power cord. The frequency range is usually between 150 kHz to 30 MHz. The impedance of power network is usually not consistent within different locations and conditions. So, a device is put between the power cord and the equipment to stabilize the line impedance. Different types of Line Impedance Stabilizer Network or LISN are recommended by EMC standards. LISN basically is a low pass filter that blocks the noise coming from the power cord. It defines a specific impedance characteristic to the equipment. A LISN may seem simple which can be to be built by individuals. However, commercially-available LISNs on the market is usually used for safety reasons as they operate with the line current and voltage. The measurement port of the LISN is connected to a spectrum analyzer or an EMI receiver. Conducted emission and immunity test should be performed on any device connected to AC or DC power supply. A sample standard for conducted emissions test is FCC part 15, subpart B [5].

Conducted immunity test simulate the real-world voltage and current conditions of a power network. Radio transmitting systems and harmonic currents of a nearby power converter or a motor drive are typical sources of radio frequency disturbances. In the conducted immunity test setup, RF signals are applied to the EUT using a coupling/decoupling network. A sample standard for conducted immunity test is IEC

61000-4-6 [118].

The fundamental component of switching power converters including dc-dc, dc-ac and ac-dc converters is the switching devices. Although switching devices including diodes, IGBTs and MOSFET transistors make the energy conversion more efficient, they are the main source of EMI noise. Switched voltage and current waveforms with short switching transition and high dv/dt and di/dt trigger many EMC issues including common mode and differential mode conducted and radiated emissions. For instance, the diode reverse recovery charge generates a negative voltage spike at turn-off leading to differential mode noise. This is a common scenario since diodes are a basic component of power converters.

Current harmonic and voltage flicker testing

These two power quality tests are often required by European standards. Current harmonic test is performed to make sure that emitted harmonics are below the standard limits. Current harmonic limits for class A products are specified in IEC61000-3-2 standard [119] and listed in Table 4.3. This standard applies to the equipment that are directly connected to a public low voltage network (public 230V AC mains) with maximum current rating of 16 A per phase. IEC61000-3-12 is the alternative standard applied to equipment with higher current ratings (up to 75A) [120]. Class A incudes balanced three-phase equipment, household appliances, tools, dimmers, and audio equipment. The standard also specifies the acceptable voltage source requirement such as voltage and frequency tolerances and the voltage harmonic contents. The current harmonics can be measured and analyzed via a power analyzer. In case of power converters, especially inverters, input currents have highly rich harmonic

content and the current harmonic requirements should be considered in the early stages of design. In some cases, it is almost impossible to pass EMC requirements without line filters.

Table 4.3: Harmonic limits for class A equipment EN61000-3-2

Harmonic number	Maximum permissible harmonic current (A)
Odd harmonics	
3	2.3
5	1.4
7	0.77
9	0.4
11	0.33
13	0.21
$15 \leq n \leq 39$	$0.15 \times 8/n$
Even harmonics	
2	1.08
4	0.43
6	0.3
$8 \leq n \leq 40$	$0.23 \times 8/n$

Voltage flicker testing is one the earliest EMC tests that was introduced as a standard requirement. This test limits the AC supply rms voltage fluctuations and the visual effect of the equipment on filament lamps sharing the same supply. In Europe, standard EN61000-3-3 controls the voltage fluctuations and limits the inrush current [121]. In the inrush current test, the power supply is manually turned on and off several times and the average inrush current over the first 10 milliseconds is measured. The test is repeated for about 24 times and the average inrush current value is reported as the final inrush current value. The setup is simple for this category of tests. A simple oscilloscope or a power analyzer can be used for measurement.

Electrostatic discharge

Electrostatic discharge (ED) is a very common transient EM phenomenon happening which happens when the equipment contacts with human body and other tools carrying electrostatic charges. This short burst of energy may cause integrated circuit resetting, Liquid Crystal Display (LCD) damage, memory corruption or digital logic errors. An ESD generator is used to apply the ESD to a device at the points that can be touched by a human being. The ESD generator can have two types of tips: air discharge tip where the ESD happens through an arc in the air or contact discharge tip that needs to be in contact with the device to apply ESD. Based on the discharge method, standards define different test voltage level, typically 2, 4, 6 and 8 kV. The ESD is applied at least ten times, at a specific frequency, to different parts of the device and the performance of the EUT is monitored to locate the weak points. Any ESD protection should react fast since the ESD waveform occurs very short, in the order of few tens of nanoseconds. A sample standard for ESD is IEC 61000-4-2 [122].

Electrical fast transient

Electrical fast transient (EFT) is another transient immunity test that ensures the device can handle the EFT energy emitted by electrical switches, inductive load switching, motor, or relays. Predefined EFT disturbance is applied to the power ports through direct coupling and to any signal/control ports exceeding 3 meters lengths through indirect coupling (using capacitive clamps). The required immunity test generator is simple but expensive. The EFT is applied to the EUT in forms of burst sequences, typically at the frequency of 50 kHz for 15 ms and recurring after a 300 ms pause. A sample standard for EFT is IEC 61000-4-4 [123].

Magnetic field

Magnetic field test is similar to radiated immunity test but it has a lower frequency range. One of the common types of magnetic field test is the AC power line in which the 50/60 Hz signal is used to create the field. A current transformer is placed between the signal generator and the antenna creating a uniform magnetic field. This test is not required if the device does not have any component sensitive to magnetic field. Hall effect elements, relays, and CRT monitors are amongst sensitive components.

In power converters, and especially switched mode power supplies, current loops and switching transformers are main sources of magnetic field. Loop area and the rate of change of current are proportional to the amplitude of emitted magnetic field. Therefore, special care must be taken in the layout design to minimize the loop area. The loop areas are also good receivers picking up the magnetic fields. The best practice to improve the immunity of circuits is to reduce the loop areas by a proper layout design such as routing signal line and its return close to each other or twisting them together. Switching transformer with minimum magnetic field leakage is also desirable to reduce emissions [3].

Surges

Voltages surges can be harmful to the devices and can easily burn ICs, damage motor windings, and cause serious thermal issues. They contain a large amount of energy and emitted from a power grid fault or a nearby lightning strike. Surge immunity test ensures the functionality of devices connected to AC or DC power sources. An immunity signal generator with a surge module is used in full compliance tests to generate the required surge signal and is directly coupled through a simple capacitive

coupling to the power cord and signal ports longer than 3 meters. A sample standard for surge test is IEC 61000-4-5 [124].

Voltage dips, drops and interruptions

These tests monitor the performance of devices under voltage dips and drops, where the power supply drops to a certain value, and AC/DC power supply brownouts where a complete but short disconnection of power supply happens. Equipment directly connected to AC or DC power supply may have issues to pass these tests. An autotransformer with fixed taps creates required levels of input signal. Then, a simulator provides the standard dipped input power for the EUT using the transformer output [114]. A sample standard for voltage dips and interruptions is IEC 61000-4-11 [125].

4.3 EMI receivers and analyzers

Two types of measurement are well-known for EMI applications. Conventionally, frequency domain measurement has been used for radiated and conducted emission tests. Spectrum analyzers are the most common EMI receiver in EMC test labs. Most of the spectrum analyzers operate based on the frequency domain measurement technique. The operating principle of this method, also known as swept-tuned method, is shown in Fig. 4.1. The input signal (f_s) is combined with a local oscillator (LO), oscillating with the frequency of f_{LO}, through a mixer. The output signal is actually the input signal translated to an intermediate frequency (f_{IF}) containing both f_s and f_{LO} signals plus their differences, $f_s \pm f_{LO}$. Then, it is filtered by a bandpass filter with a defined resolution bandwidth (RBW) and center frequency of f_{IF}. In the next

step, a detector captures the signal magnitude to be displayed at the output screen. This process is repeated for all frequencies of interest by sweeping the LO frequency. The sweep generator simply controls the frequency of LO and synchronizes the frequency axis of output display with the tuned frequency [126]. Most of the spectrum analyzers work based on this measurement method. If the frequency spectrum of the input signal (f_s) contains frequencies up to 30MHz and the IF filter operates at 200MHz (f_{IF}), the frequency of local oscillator (f_{LO}) should sweep from 200MHz to 230MHz.

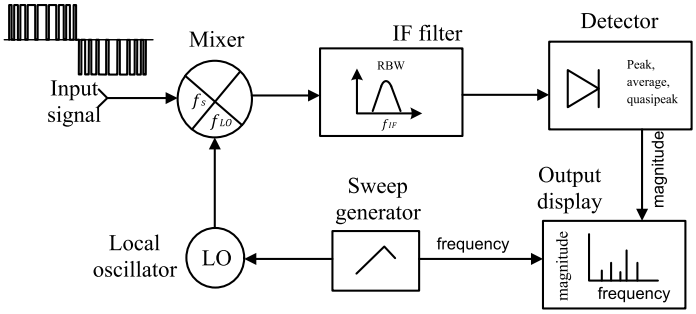

Figure 4.1: Block diagram of operating principle of frequency domain EMI measurement.

All harmonics within the RBW of IF filter are summed together and reported as the noise level at the center frequency. So, the narrower the RBW, the lower the noise level will be. Minimum value of RBW is defined by the standard. FCC and CISPR use RBW of 9kHz for the frequency range of 150kHz to 30 MHz, 120kHz for 30 MHz to 1GHz, and 1MHz for frequencies higher than 1GHz. Different types of detectors including peak, average and quasi-peak detectors can be used. Peak detector is the simplest one that is commonly used as the first option. A quasi-peak detector measures the frequency weighted signal to account for the energy that the noise signal carries.

Frequency domain and time domain representation of a signal are related together by Fourier transform. However, the frequency swept-tuned method is different from Fast Fourier Transform (FFT) which is widely used for signal transformation. All the steps are performed in analog circuit and the analog-to-digital (ADC) conversion only happens right after the detection and before displaying the result. The input signal is assumed to be stationary and the process is repeated for all frequencies of interest (e.g. 150kHz to 30MHz for conducted emission). This method can be slow for fast transient signals that are rich in harmonics. Another method, especially suitable for fast transient EMI measurement, is based on FFT results and known as time domain EMI measurement (TDEMI). Fig. 4.2 depicts the general process of TDEMI. In this method, the time domain signal is obtained by an analog EMI measurement device. Next, the data is converted to digital data with an ADC module. The ADC module can be embedded in the measurement device or it can be an external module. The rest of the process is signal processing including windowing, resolution enhancing, resampling, spectrum calculation based on FFT and detector simulation that is performed at a computational platform, such as personal computers [127, 128, 129], field programmable gate array (FPGA) board [130, 131], or digital signal processors (DSP) [132, 133, 134].

TDEMI measurement has been studied in the literature and is also available in standards as a viable solution so that the general requirement of such a system is specified. At the first step of TDEMI, data is normally obtained by a digital oscilloscope allowing for multichannel and advance triggering capabilities. With a multichannel receiver, it is possible to build a multi antenna setup and make the measurement of various antennas simultaneously. It also allows full spectrum calculation with a

single measurement. It is the best option for fast disturbances with low repetition. Frequency domain measurements, on the other hand, are the best for high frequency disturbances.

In order to achieve a comprehensive modeling of the system, it is reasonable to consider the effects of EMI measurement [127, 128, 135, 136, 137]. The effect of IF filter gain is considered in [127] where the filter model is fitted to the experimental results. So, the predicted values are more realistic and closer to the measured values from the spectrum analyzer. TDEMI method has been employed for different applications including measuring conducted emission of a signal generator, a personal computer, and a commercial dimmer [128]. The method has also been applied to radiated emission measurement [138, 139]. One of the main advantages of TDEMI method is the possibility of fast measurement. This feature makes the TDEMI a more suitable method when the ambient noise changes so fast such as railway vehicle applications [140].

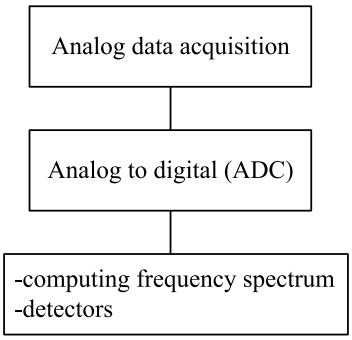

Figure 4.2: Time domain measurement process.

Another advantage of TDEMI over frequency domain measurement, is the ease of postprocessing and data analysis. All the signal information is recorded as a function of time. Then, the data is digitized and stored in a digital processor where one can

readily start the automated analysis including compliance check, mode decoupling analysis, statistical analysis, and other signal analysis techniques [136, 141, 142, 143]. One of the signal processing methods that provides more insight about the measured EMI is decomposition. Decomposition, similar to Fourier series, breaks down the complicated signal into a number components known as intrinsic mode functions. An empirical mode decomposition is proposed in [143] to extract the narrow band and broadband signals of the measured EMI in time domain. This method is also beneficial for removing the background noise of in situ EMI measurement system where EMI emissions of a fixed equipment needs to be measured at the site. EMI receivers need to be calibrated before the measurement. Otherwise, the measurement results might not be reliable or valid. Although EMC standards usually mandate the requirement of calibration pulses, the exact waveform or calibration method is not specified [134, 144, 145]. Pulse generators specifically manufactured for calibration of EMI receivers are commercially available. There are also some more cost-effective solutions in the literature that use an arbitrary waveform generator to produce the required waveforms [144, 145].

4.4 Measurement devices

In this section different measurement devices are introduced. An EMI measurement setup normally requires a number of devices including sensors to sense the EMI disturbance, typically in forms of voltage, current or electromagnetic fields. Another important part of an EMI measurement setup is the coupling and decoupling devices to apply the target signal to a specific line of part of a system. They also ensure that the rest of the system is immune and decoupled from the disturbance.

4.4.1 Conducted emissions

Measurement devices used for conducted emission and susceptibility testing can operate either in direct contact with the EUT or without a direct connection and through inductive coupling. LISN is the most common device for conducted emission testing with direct connection. The main function of LISN is to define a given impedance into the EUT as a function of frequency. Moreover, LISN filters the radio frequency noise coming from the power mains. LISN is placed between the EUT and each line of the power mains. Fig. 2.3 shows the schematics of a typical 50 µH LISN and the impedance characteristics.

Another important category of direct contact measurement devices are voltage probes. An acceptable voltage probe should not introduce extra load to the circuit so that it can measure the true signal. Therefore, the input impedance of voltage probes should be high over the frequency range of interest, i.e. 150kHz to 30MHz for conducted emission. Voltage probes are available as active and passive probes. Passive probes, typically used in oscilloscopes, work based on impedance division and have limited bandwidth. Active probes, providing higher bandwidth, are suitable for low level RF signals, in the range of mV. RF coupling capacitors are commonly employed in EMI immunity test setups for signal injection. High quality low impedance capacitors are required for coupling purposes. A typical immunity test setup is shown in Fig. 4.3. The RF coupling capacitor ensures the signal is applied properly to the EUT. At the same time, a decoupling network, sometimes a blocking inductor, is employed to protect the power mains. Engineers must ensure that the power line high voltage does not couple back through the coupling capacitor to the signal generator causing malfunction and damage to the device. Some high-quality RF capacitors

contain internal filters to block the high voltage power line and protect the signal generator and the measurement device. In some applications, capacitor clamps are used to avoid a direct contact. They are usually more cost-effective, easy to setup and introduce less load to the circuit [4].

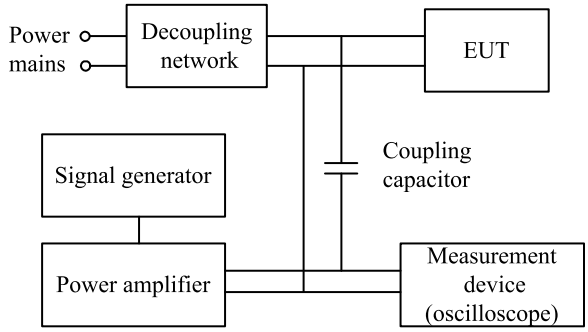

Figure 4.3: Coupling capacitors in an immunity test setup.

Transformers are also used as a directly connected device. They are mostly used in immunity test setups especially for high voltage and low frequency signal injection. Magnetic field immunity test and voltage dip immunity test are amongst EMC tests that require a transformer. Cable current probes are the most common type of contactless measurement devices. The current flowing in a conductor creates a magnetic field around the conductor. A current probe, at its simplest form, contain magnetic field pickup coils that induces a voltage proportional to the current value. It is worth mentioning that a current probe, measures the total current flowing in the bundle. So, common mode and differential mode currents can be measured directly by proper cable arrangement. For accurate measurement, it is best to keep a distance of few centimeters between the current probe and adjacent cables. The current probe could also be used for signal injection. Current probe can also be in the form of current clamp as a distributed measurement device. Several research studies have been conducted

on the electric and magnetic probes including probe design [146, 147, 148, 149, 150], modeling, and calibration of measurement probes [151, 152].

4.4.2 Radiated emissions

Antennas are the fundamental measurement devices of radiated emission and susceptibility testing. Based on the frequency range, field strength, and the application, various types of antennas are used. Loop antenna is amongst the most common and inexpensive ones for low frequency measurement, up to 30MHz. Biconical, log periodic and horn antennas are also common. They are designed for higher frequency measurement setups. Fig. 4.4 shows three common antenna used in radiated EMI tests. The antenna should have enough gain to boost the signal into a reasonable measurable level that can be accurately captured in an EMI receiver. Sometimes, an amplifier is also required. Measurement of antenna gain is required to ensure the calibration of the antenna that has been studied in the literature [153, 154, 155].

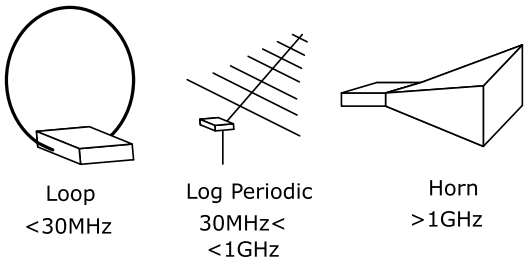

Figure 4.4: Common antennas for radiated emissions measurement.

4.5 Test equipment on the market

In this section, some of the manufacturers of common EMC measurement tools are listed. Research centers, universities and EMC testing lab could use the list as a

guide [156].

∗This table is updated but will be removed in the final version.

4.6 Summary

EMC measurement needs to be considered from the early stages of design and prototyping. In this chapter, a review of most common EMC tests, required during the final compliance testing, is presented. In summary, the first step is to prepare a test plan to know the EMC requirement of the target application. Once the first prototype is prepared, pre-compliance test can be performed at the site or in EMC testing labs. Moreover, an introduction into measurement devices is provided along with potential research areas. A table of manufacturers of commercially available EMC testing instruments are also listed.

Table 4.4: EMC equipment manufacturers

Manufacturer	**Antenna**	**RF Amplifier**	**Spectrum analyzer**	**LISN**	**Signal generator**	**Current probes**	**Oscilloscope**
Aaronia	×	×	×		×		
A.H. Systems	×	×				×	
Aim and Thurlby Thandar			×		×	×	
Ametek	×	×			×	×	
Anritsu			×		×		
AR RF/microwave instrumentation	×	×	×	×	×		
BHD test and measurement		×	×	×			
BK Precision			×		×		×
ComPower	×	×	×	×	×	×	
GwInstek			×		×		×
Hantek			×		×		×
Kent Electronics	×						
Keysight Technologies			×	×	×		×
PMM Test	×	×	×	×		×	
Rigol Technologies			×		×	×	
Rohde & Schwarz	×	×	×	×	×	×	×
Tekbox Technologies	×	×		×			
Teledyne lecroy			×		×	×	×
Siglent			×		×		×
Solar Electronics	×			×	×	×	
Tektronix			×				×
Teseq	×	×		×	×	×	
Test Equity		×	×	×	×		

Chapter 5

Analytical EMI Modeling of an Active Neutral Point Clamped Inverter

This chapter studies the electromagnetic interference (EMI) noise modeling for a three-level active neutral point clamped inverter. Although time-domain detailed modeling leads to more accurate results, frequency-domain modeling techniques are commonly used as a faster prediction method. Compared with the conventional differential mode (DM) EMI modeling of power inverters that use only one current source, it is shown that two current sources are required for more precise modeling. A new unified model is proposed for an active neutral point clamped inverter based on the existing equivalent circuit models for common mode (CM) EMI and the developed DM model. Both CM and DM EMI emissions are predicted by the proposed model and compared with the time-domain results. Simulation results indicate that the modeling precision is improved by 56%.

5.1 Introduction

Multilevel power converters are commonly used in the industry to extend the power and voltage ranges of conventional two level converter [157, 158]. The three-level neutral point clamped (3L-NPC), also known as diode clamped inverter topology is amongst the most popular multilevel inverters. The uneven power loss distribution between the switching devices leading to different temperature rises is the major disadvantage of this topology. Active NPC is used to overcome the unbalance problem [159]. In an ANPC, controllable switching devices are used instead of clamping diodes, as shown in Fig. 5.1.

The recent advances in semiconductor technologies have led to faster switching devices, higher switching frequencies, and more compact designs. At the same time, electromagnetic compatibility (EMC) has become a new issue that should be addressed properly. Various national standards set the limits of electromagnetic interference (EMI) emissions that should be met by all electronic devices. In addition to the EMC regulations, the EMC is an important aspect of design that is capable of enhancing the performance in terms of reliability.

The primary source of EMI emissions is the switching operation of the switching devices that induce high dv/dt and di/dt. The generated noise flows in the system through the conduction paths as the conducted emissions. At higher frequencies, radiation emissions are also concerned. In this chapter, the conducted EMI emissions in the frequency range of 150 kHz up to 30 MHz are the main interest.

In order to investigate the EMC characteristics of power converter systems, EMI models are required. There are mainly two approaches for EMI modeling: time domain and frequency domain modeling [160]. In the time domain approach, also

known as detailed modeling, each device is modeled based on its physical behavior [31, 36, 37]. The system model is made up by putting each device model together. The frequency-domain approach can be further classified as behavioral modeling (BM) and equivalent circuit or filter-oriented modeling. In BM, the behavior of the system is characterized at the input ports by multi-port networks [20, 19, 24, 25]. EMI measurements are required in BM, which means it is not an actual *prediction* model. In the equivalent circuit modeling, the noise sources are approximated by analytical/mathematical expressions, while the passive components are modeled by their physical model or a simplified version of them.

Time-domain EMI modeling is the most precise technique since it can capture the nonlinear behavior of switching devices. It can precisely model the switching transients and ringing effect of the power devices. However, there are two major drawbacks to time-domain modeling. First, it is time-consuming due to the required small time step. Moreover, as the number of switches and nonlinear devices increases, the convergence problem may arise due to the complexity of the system. Therefore, the frequency-domain approach is commonly used for faster modeling of complex systems.

Although there are several studies on the modeling of a conventional 2-level inverter, few chapters are related to the 3-level NPC topology. While there is only one switching node in the 2 level inverter, there are three switching nodes in a 3L-NPC. A CM model of 3L-NPC with three voltage sources for each switching node is proposed in [107, 161, 162]. The accuracy of the model is evaluated with measurement results. However, the DM model of the 3L-NPC is not studied in the literature.

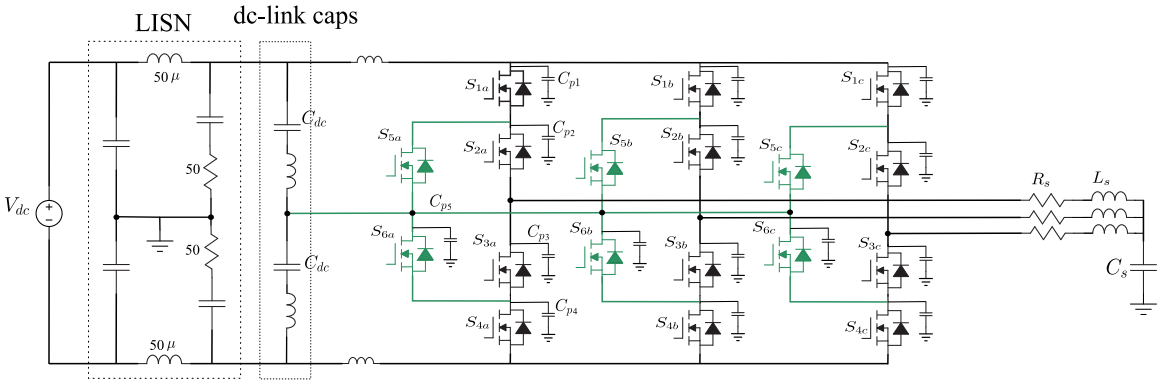

Figure 5.1: The detailed model of the ANPC considering main parasitic elements.

5.2 Time domain model

In order to evaluate the performance of the EMI noise models, a detailed model of the ANPC is required. The circuit diagram of the three-level ANPC is shown in Fig. 5.1. The ANPC that is investigated in this study is designed for electric vehicle (EV) application and it utilizes silicon carbide (SiC) switching devices. The design parameters of the ANPC are listed in Table 5.1.

A physics-based model of the SiC MOSFET (UJ4C075018K4S by United SiC), as the primary EMI noise source, is derived using Ansys Simplorer device characterization tool. The performance of the extracted dynamic model of the MOSFET is assessed in a half-bridge circuit and compared to the datasheet values. Table 5.2 summarizes the comparison results that show a good agreement between the simulation and the datasheet values.

The parasitic elements of different parts of the circuit should also be considered. In Fig. 5.1, the main parasitic elements are shown, including the stray inductance of the dc-link capacitors, the stray inductance of the Printed Circuit Board (PCB) traces, and the stray capacitance between the MOSFETs and the heatsink. 3D finite

Table 5.1: The Design Parameters of the Active Neutral Point Clamped Converter

parameter	**description**	**value**
$P_{o,c}$	Continuous output power	70 kW
$P_{o,T}$	Transient output power (10 s)	120 kW
f_s	Carrier frequency	60 kHz
f_o	Output frequency	60 Hz
V_{dc}	dc-link voltage	600 V

Table 5.2: Switching characteristics of the SiC Mosfet (sim: simulation result, data: datasheet value)

		T_{on} (ns)	T_{off} (ns)	E_{on} (μJ)	E_{off} (μJ)	Q_{RR} (nC)
T=150	Data	52	172	453	304	109
	Sim	53	174	421	305	109
T=25	Data	48	163	407	255	102
	Sim	49	161	385	254	103

element analysis (FEA) is used to calculate the stray inductance of the PCB traces along with the mutual inductance between them. Discrete power MOSFET is used in the ANPC circuit. Therefore, the stray capacitance between the case and the heatsink is placed between the drain and the ground. C_{p1}, C_{p3}, C_{p4} and C_{p5} represent the stray capacitance between S_1, S_3, S_4, S_6 and the ground, respectively. The stray capacitances of S_2 and S_5 are summed up and shown as C_{p2}. Therefore, the stray capacitances of the upper and lower parts of a phase leg are not the same. Each of the semiconductor stray capacitances can be determined by FEA or analytical calculations. The stray elements of the dc-link capacitors are obtained from the datasheet.

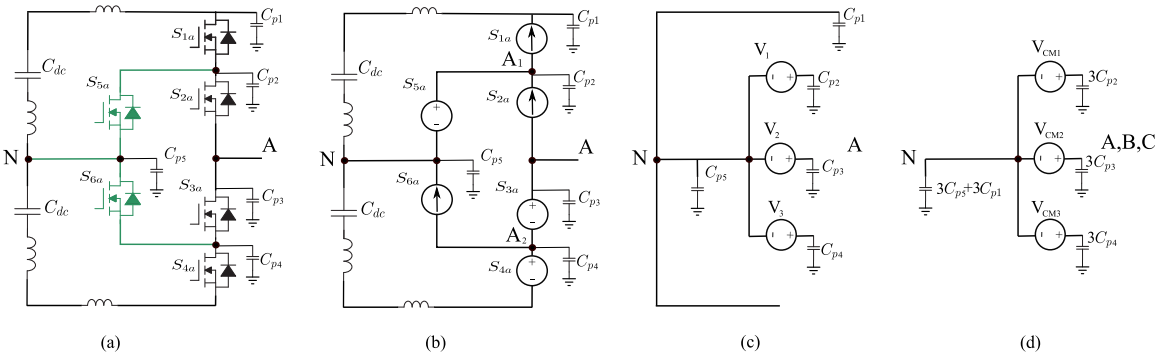

Figure 5.2: Common mode modeling of the ANPC a) Phase A leg, b) Substituting MOSFETs with voltage and current sources, c) Short circuiting the dc link capacitors and sources are merged, d) Three phase CM model of the inverter.

5.3 Frequency domain model

As mentioned earlier, frequency-domain modeling is a faster approach for EMI prediction. In this method, the substitution theorem is applied to the EMI noise sources while the rest of the circuit remains the same as the time-domain model. The noise sources, i.e., switching devices, are replaced by the voltage and current sources. As long as the substituted sources and switched devices have the same time-domain waveform, modeling results would be the same. However, obtaining the waveforms could be challenging in some cases. In some chapters, switching waveforms are assumed to be trapezoidal [163, 43, 39]. The ringing effect of the switching devices is also considered in some papers to improve the EMI noise source model [40, 33]. In another approach, direct time-domain waveforms from the detailed model or the measurement setup can be used, which is the method utilized in this chapter. First, the EMI noise source model is developed for CM and DM emissions. Next, the equivalent circuits are combined together to obtain a unified model.

5.3.1 EMI noise source modeling

To begin with the three-phase modeling of the 3L-ANPC, a single-phase leg is considered. Fig. 5.2a shows phase A of the inverter along with the parasitic elements. In the next step, MOSFETs are replaced by voltage and current sources, as shown in Fig. 5.2b. Any combination of current and voltage sources can be used as long as the voltage sources are not placed in parallel and current sources are not placed in series. In this model, S_{1a}, S_{2a} and S_{6a} are substituted with current sources while voltage source substitution is applied to S_{3a}, S_{4a} and S_{5a}. It should be mentioned that all the noise sources have the same time-domain waveforms as the original MOSFET.

Fig. 5.2 shows the process of developing the CM equivalent circuit. High dv/dt of switches induce CM currents into the ground through the parasitic capacitance of the circuit. One factor that contributes the most is the stray capacitance of MOSFETs to the heatsink/ground, $C_{p1}, \ldots, C_{p5}$ and they should be considered carefully in the CM equivalent circuit model.

The circuit can be further simplified. For CM modeling, the dc-link capacitors are assumed to be short circuited due to the small impedance. Current sources can also be treated as open circuit since they have no impact on the CM emissions. CM voltage sources of phase A can be arranged in Fig. 5.2c where:

$$V_1 = V_{S5a} \tag{5.1}$$

$$V_2 = V_{S3a} + V_{S4a} \tag{5.2}$$

$$V_3 = V_{S4a} \tag{5.3}$$

Hence, the CM model of the three-phase ANPC can be shown as in Fig. 5.2d with

three CM voltage sources, $V_{CM1}, V_{CM2}, V_{CM3}$, for each of the switching nodes that induce CM currents into the stray capacitors.

$$V_{CM1} = \frac{V_{A1N} + V_{B1N} + V_{C1N}}{3} \tag{5.4}$$

$$V_{CM2} = \frac{V_{AN} + V_{BN} + V_{CN}}{3} \tag{5.5}$$

$$V_{CM3} = \frac{V_{A2N} + V_{B2N} + V_{C2N}}{3} \tag{5.6}$$

In order to develop the DM model, we begin with a single phase. In the same manner, we can perform some simplifications. DM currents flow between the input ports and in the same direction as the main current. Ideally, dc-link capacitors can generate all the high-frequency ac currents required by the inverter. However, at higher frequencies, nonideal capacitors have comparable impedance due to their stray inductance and resistor. Therefore, a part of the high frequency ac current flows back to the input source as DM noise current.

A current source in parallel with the dc-link capacitor is commonly used as the DM equivalent circuit for the conventional 2 level inverter [39]. Unlike the 2L inverter, 3L-ANPC requires two current sources. The neutral current charges and discharges the capacitors during the switching transients and its contribution to DM emissions should be considered.

Fig. 5.3 shows DM modeling process. The current and voltage source substitution is shown in Fig. 5.3a, which is the same as Fig. 5.2b except for the stray capacitance. The stray capacitance between the MOSFETs and the ground can be ignored since

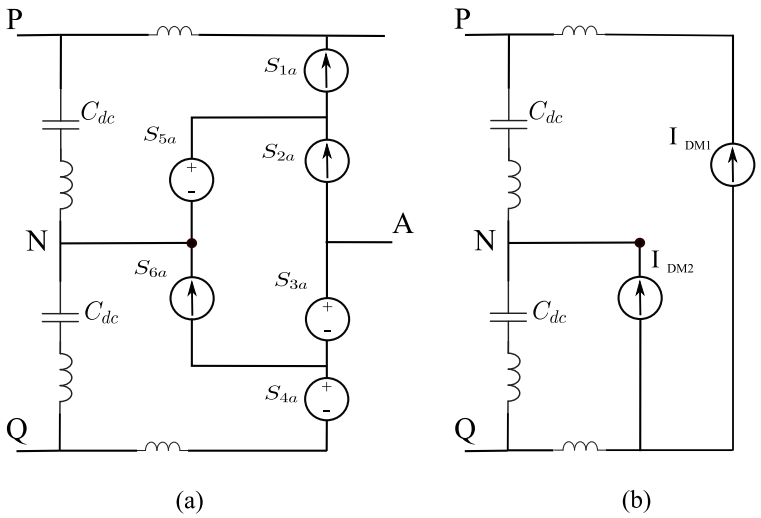

Figure 5.3: Differential mode modeling of the ANPC, a) substituting MOSFETs with current and voltage sources, b) DM model of the inverter.

they have little effect on DM emissions. The final DM noise source model of the 3-phase 3L-ANPC is simplified in Fig. 5.3b. DM current sources can be determined as follows:

$$I_{DM1} = I_{S1a} + I_{S1b} + I_{S1c} \tag{5.7}$$

$$\begin{aligned} I_{DM2} = I_N = I_{S6a} + I_{S2a} - I_{S1a} + \\ I_{S6b} + I_{S2b} - I_{S1b} + I_{S6c} + I_{S2c} - I_{S1c} \end{aligned} \tag{5.8}$$

5.3.2 Unified equivalent circuit model

DM and CM equivalent circuits have been developed separately. It has been assumed that DM and CM noises are decoupled, meaning they have a negligible effect on each other. However, it has been shown that the asymmetric impedance paths of power converters lead to some level of coupling between DM and CM emissions [164].

Converter asymmetric impedance results in an uneven flow of CM current in the input ports, ultimately contributing to the DM noises. This is known as mixed-mode (MM) emissions.

Conventional 2L inverter and 3L-ANPC are amongst the balanced structures, and mixed-mode emissions are usually low. However, the inverter impedance is not symmetric during the switching transients due to different switching states. This phenomenon is demonstrated in Fig. 5.4 for phase A only. The upper switches S_{a1}, S_{a2} are ON while the lower side MOSFETs S_{a3}, S_{a4} are switched off. CM currents are shown in red arrows, and intrinsic DM currents are shown in blue arrows. It can be seen that the upper and lower parts of the phase leg are not symmetric. Hence, I_{CM} is not flowing equally in the LISN resistors, i.e. $I_{CM1} \neq I_{CM2}$. So, CM currents contribute to DM noise according to the following:

$$I_{MM} = \frac{I_{CM1} - I_{CM2}}{2} \tag{5.9}$$

Therefore, the effect of MM should be studied, especially when the inverter is operating in a fault condition. In Fig. 5.5, a unified equivalent circuit for 3L-ANPC is developed that can model CM and DM emissions simultaneously. In this model, LISN resistors and the load are also considered.

5.4 Conducted emissions

The developed equivalent circuit models should be evaluated. First, the EMI noise source is obtained from the time-domain simulation results and calculated using (5.4)-(5.8). The reference emissions are the results from the time-domain model. The

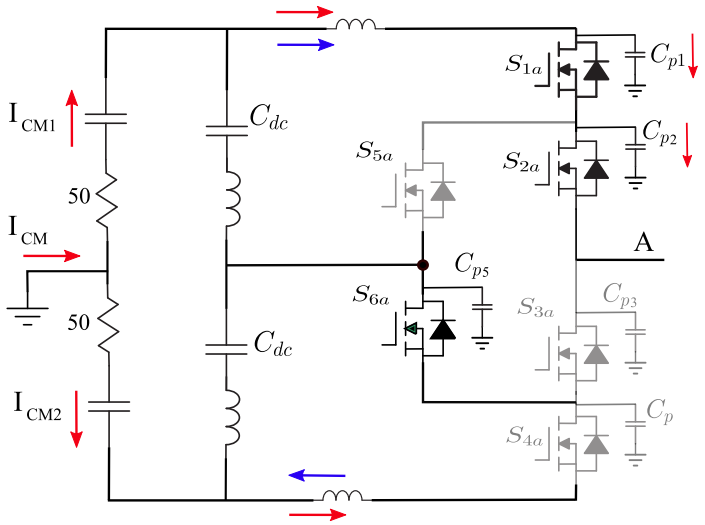

Figure 5.4: Asymmetric impedance paths of CM currents leading to MM emissions (state P in phase A). Red arrows: CM currents, blue arrows: DM currents.

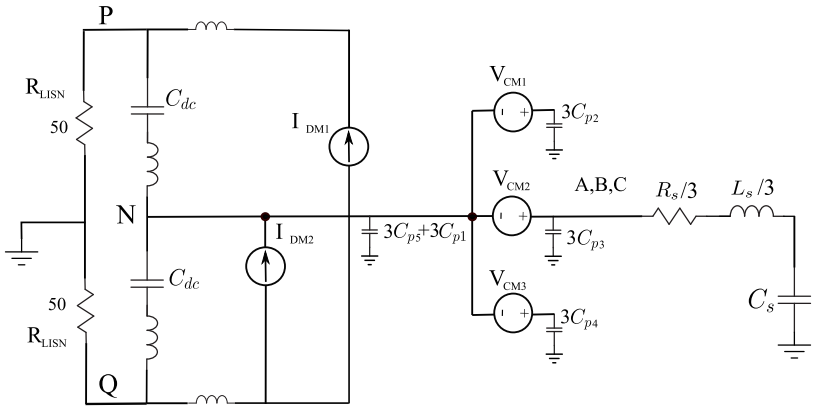

Figure 5.5: Unified equivalent circuit of the system.

minimum time step for the time-domain model is 16 nanoseconds since the maximum frequency of interest for conducted emissions is 30 MHz.

The simulation results of the unified equivalent circuit model are compared to those of the time-domain model, demonstrated in Fig. 5.6. It is observed that a good agreement exists between them. In order to investigate the DM model more closely, three models are considered. The first one is the developed unified model with two DM noise sources. In the second case, the neutral current source I_{DM2} is removed, and only I_{DM1} is used. This case is similar to the DM model of the 2L inverter and aims to study the effect of neutral current. The third model only considers the intrinsic DM current without considering the impact of MM emissions. The results of each case are compared to the DM emissions of the time-domain model and the results are presented in Fig. 5.7. Root mean square error (RMSE) is used to evaluate the numerical results. RMSE of the second and third cases are 8 and 8.5 $dB\mu V$ while the developed unified model with two current sources can reduce the RMSE to 3.5, around 56% improvement.

5.5 Summary

In this chapter, EMI modeling of a 3-level ANPC inverter is studied. Both time-domain and frequency-domain modeling techniques are investigated. First, a detailed time-domain model is developed. The dynamic model of the SiC MOSFET is obtained by a characterization tool, and its performance is evaluated in a test circuit. The passive components are carefully modeled in FEA, and the primary parasitic elements are considered. Then, a unified equivalent circuit model is developed for a faster modeling approach.

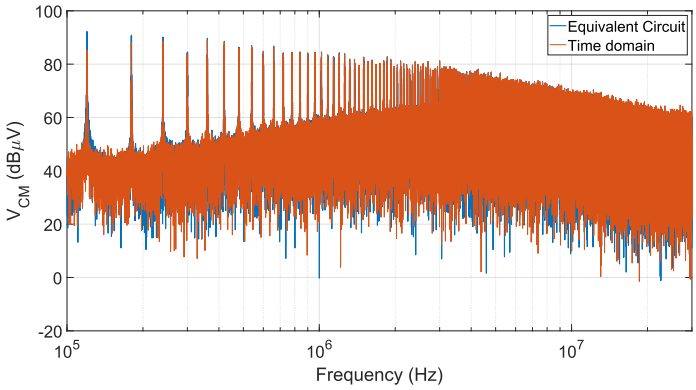

(a)

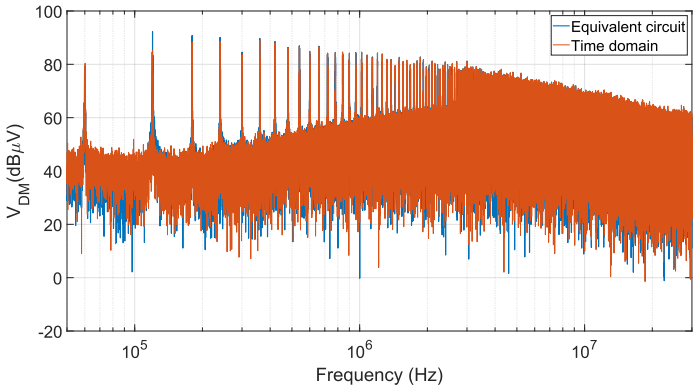

(b)

Figure 5.6: Comparison between the prediction of unified equivalent circuit and the detailed model a) V_{CM}, b) V_{DM}.

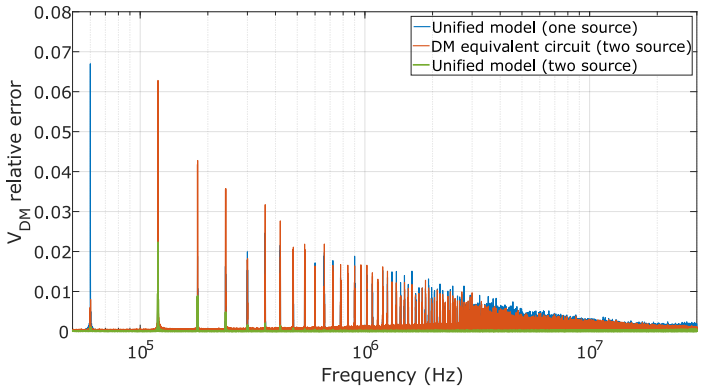

Figure 5.7: Prediction error of V_{MD} in different models.

The process of CM and DM equivalent circuit models is elaborated. Finally, the unified model performance is compared with the time-domain simulation results. It has been shown that unlike DM modeling of the 2L inverter, two current sources are required for 3L ANPC modeling. The accuracy of the DM model improved by 56% when neutral current is also considered. As the future work, the simulation results should be verified by the measurement results.

Chapter 6

Mitigating Conducted Electromagnetic Interference of an Active Neutral Point Clamped Inverter by Spread Spectrum Modulation

Spread spectrum modulation techniques have been proven to be an effective solution to suppress the conducted electromagnetic emissions of power converters. These methods spread the power spectrum in the frequency range thus reducing the harmonic spikes. In this chapter, different modulation methods are investigated for an active neutral point clamped (ANPC) inverter with electric vehicle application. A random pulse width modulation (RPWM) scheme and different periodic PWM

techniques are applied to the ANPC and their effectiveness on the conducted EMI mitigation are compared. (Theoretical analysis of power spectrum is also carried out.) The effect of EMI receiver and intermediate filter bandwidth is considered in the modeling. The validity of simulation results and calculations are confirmed by experimental results.

6.1 Introduction

Electromagnetic compatibility (EMC) is one of the challenges needs to be addressed in any electronic device before placing in the market. Based on the target market, certain EMC regulations should be met by the manufacturers. It is more cost effective to consider the EMC during the design stage. There are several methods to suppress the excessive EMI emissions. Beginning with the topology, the inverter structure can be optimize to minimize the emissions. Having in mind that the main source of electromagnetic emissions is high dv/dt and di/dt induced by semiconductor switching, multilevel topologies provide lower noise source [165]. More EMI suppression can be achieved through balancing structures such as bridge balancing principle [166], optimizing the transformer with lower stray inductance [167], and component selection [94]. Once the structure and components are selected, EMI suppression methods are limited to optimizing noise source and coupling paths. It has been shown in the literature that EMI noise source can be controlled by shaping the switching transients. Snubber circuits and active gate drivers are common tools to modify the switching transients and ultimately lower the noise spectrum [91, 168, 91]. Spread spectrum modulation methods are another solution to improve the noise source spectrum by lowering the harmonic spikes. Last but not least, active and passive EMI filters are

the conventional remedy to mitigate the conducted EMI emissions and to comply with EMC regulations [169, 170]. Specific shielding and grounding techniques further contribute to a EMC compliant design. A classification of EMI suppression methods is shown in Fig. 6.1.

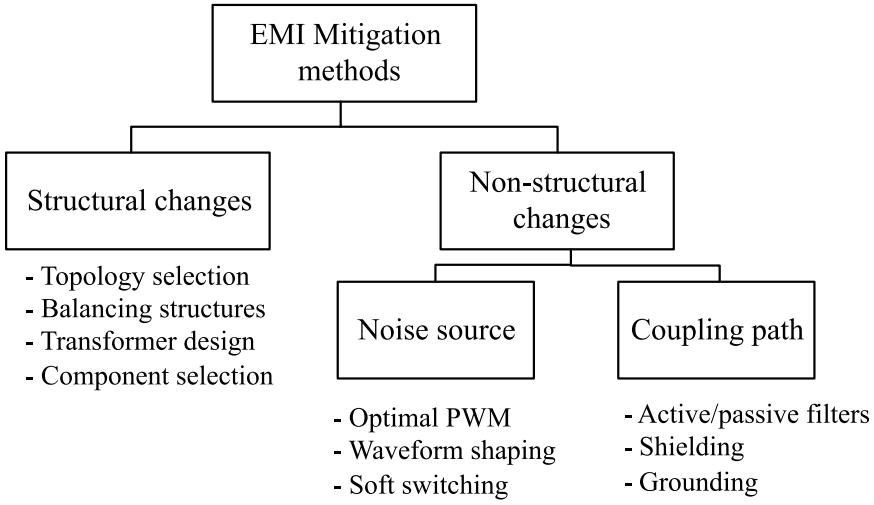

Figure 6.1: EMI suppression methods.

EMI filters usually consume a considerable volume of the system since huge input current passes through the filter elements. Towards a more compact design, it is desirable to minimize the EMI emissions at the source. Harmonic spectrum of the common mode voltage source of a three phase conventional inverter is depicted in Fig. 6.2 when constant frequency pulse width modulation or CSFPWM is applied. It is observed that the power spectrum is concentrated around the switching frequency multiples. The idea behind the spread spectrum modulation techniques is to spread the harmonic content over a wide frequency range so that the harmonic spikes are lowered. Two contributing factors are the PWM pulses and the transient specifications such as rising/falling times and ringings. Switching waveforms basically consist of trapezoidal shape pulses and some ringings. According to the harmonic spectrum of

a trapezoidal pulse, pulse width determine the harmonic behaviour at lower frequency ranges and switching transients are more contributing at higher frequencies. The harmonic content of the CM voltage for two cases is shown in Fig. 6.2. In both cases, the PWM pattern is the same but different IGBTs are used such that the switching transients are the main difference. It can be seen that the PWM pattern is dominant contributing factor up to a few MHz and transient behaviour is more important after that point. The switching frequency has the key role in the harmonic spectrum of the EMI emissions especially in case of CSFPWM. The lower the switching frequency, the lower is the effect of PWM pattern in the conducted EMI frequncy band (150 kHz-30 MHz). In case of a low switching frequency, such as 5kHz, the harmonic spikes are already low in 150 kHz and the switching transients are the dominant contributing factor. Therefore, the proper suppression technique can be selected based on the switching frequency and the harmonic spectrum of the conducted EMI emissions.

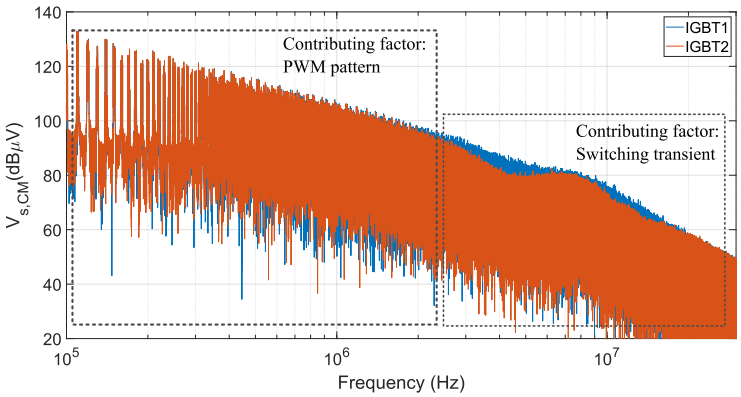

Figure 6.2: Harmonic spectrum of the CM voltage of a three phase conventional inverter using two IGBTs.

Spread spectrum modulation techniques can be classified in three groups: periodic modulation, random modulation, and programmed modulation. A classification of

spread spectrum modulation methods is shown in Fig. 6.3. In a programmed PWM method, specific design goals are achieved through calculating the optimal PWM pattern. Current ripple reduction is used as the optimization goal in [171] to calculate the desired switching frequency. So, the switching frequency is varying at each time step smoothing out the harmonic spectrum. Selective harmonic elimination targets removing specific harmonics and shapes the PWM pattern.

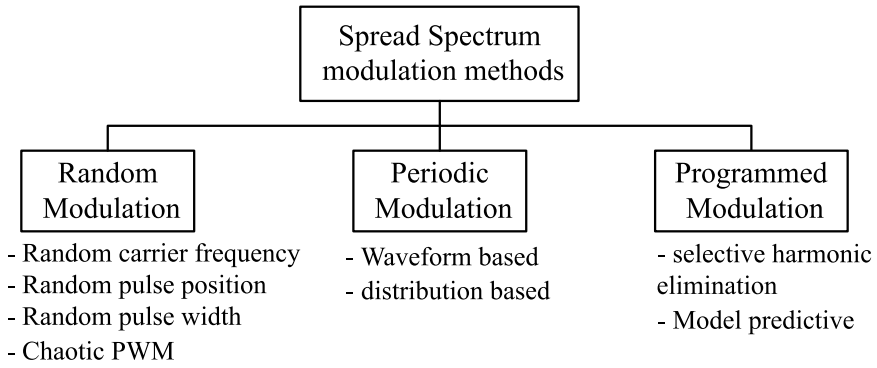

Figure 6.3: A classification of spread spectrum modulation techniques.

Random modulation techniques enjoy the non-deterministic properties of random numbers. In a PWM pattern, three parameters are normally subject to random numbers: switching frequency (or the switching period), the phase shift, and the width of the pulses [86, 172]. A different combination of the three parameters is used to obtain a spread spectrum EMI emissions. Although different researches has been made on random PWM methods, practical limitations and unpredictable Chaotic PWM is also proposed in the literature as a solution to the implementation limits of random PWM [173, 174].

In periodic modulation methods, carrier frequency is modulated based on a determined function rather than random pattern. So, the harmonic spectrum can be

mathematically calculated and the implementation is rather easier compared to random PWM. The conventional periodic PWM, carrier frequency is modulated based on the common waveforms, namely sinusoidal, triangular and exponential functions. In the other category, the switching frequency expression is derived based on the probability distribution function of the switching frequency. Uniform, normal and exponential distributions are implemented in the literature.

SS modulation methods have been applied to the switched mode power supplies largely. There are also several researches on the conventional three phase inverter. However, there are only a few papers related to the SS modulation of NPC inverters. The main focus of this study is the application of the SS methods to a three level Silicon Carbide (SiC) based ANPC inverter in an electric vehicle application. Also, most of the researches simply neglect the effect of EMI receiver on the final spectrum. As it is shown in this chapter, the resolution bandwidth of the intermediate filter has an important role at the final measured spectrum that should be considered in the analysis.

6.2 Analysis of spread spectrum modulation techniques

A typical PWM waveform $g(t)$ in a switching power converter is shown in Fig. 6.4. The output frequency is f_o and the nominal switching frequency is denoted by f_s and T_s is the switching period ($T_s = 1/f_s$). The switching pulse width is shown by DT_s where D is the duty cycle and the phase shift is presented by ϵ. The pulse is switched between A_1 and A_2 as the minimum and maximum, respectively. In case

of traditional constant frequency modulation, this PWM pulse can be expressed by double Fourier series since the signal is modulated in the time domain [175]:

$$G(t) = \sum_{m=0}^{\infty} \sum_{n=-\infty}^{\infty} C_{mn} \exp\left(j\theta_{mn}\right) \tag{6.1}$$

where C_{mn} is the magnitude of each harmonic and $\theta_{mn} = (mf_s + nf_o)t$ is the phase of each harmonic. The time varying function can be rewritten in trigonometric form as:

$$\begin{aligned} G(t) = \frac{A_{00}}{2} + \sum_{n=1}^{\infty}[A_{0n}cos(n\omega_o t) + B_{0n}sin(n\omega_o t)] + \\ \sum_{m=1}^{\infty}[A_{m0}cos(m\omega_s t) + B_{m0}sin(m\omega_s t)] + \\ \sum_{m=1}^{\infty}\sum_{\substack{n=-\infty \\ n\neq 0}}^{\infty}[A_{mn}cos((m\omega_s + n\omega_o)t) + B_{mn}sin((m\omega_s + n\omega_o)t)] \end{aligned} \tag{6.2}$$

The first line, represent the dc component, the fundamental and its baseband harmonics. The carrier frequency harmonics are represented by the second line and the third line shows the side bands of the carrier frequency harmonics. As it can be seen, harmonics appear at the multiples of fundamental frequency, multiples of carrier frequency and the combination of them. The next step is to solve for the coefficients which give the magnitude of each harmonic. Equation (6.3) is used to obtain the coefficients.

$$C_{mn} = A_{mn} + jB_{mn} = \frac{1}{2\pi^2}\int_{-\pi}^{\pi}\int_{-\pi}^{\pi} g(t)e^{j(m\omega_s + n\omega_o)t)}d\omega_o t d\omega_s t \tag{6.3}$$

For the desired switched signal of $g(t)$, the magnitudes (A_1, A_2), the phase shift (ϵ)

and pulse duty cycle (D) is required to solve (6.3). The solution is usually represented as a series of Bessel function.

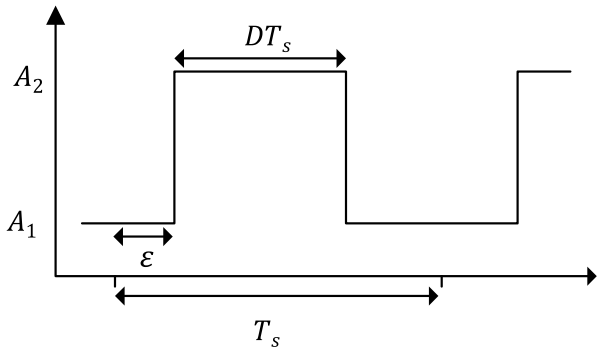

Figure 6.4: A typical PWM waveform.

6.2.1 Periodic CFM

In the traditional constant carrier frequency modulation, the signal is periodic with two parameters, f_s and f_o. In a periodic carrier frequency modulation, another parameter, normally the carrier frequency, is modulated in the time domain. So, the signal is dependant on three periodic parameters. In a waveform-based PCFM, carrier frequency is modulated based on well known functions, usually sinusoidal, triangular and cubic functions. The general form of the carrier frequency of PCFM is as below.

$$f_s(t) = f_{s0} + \Delta f_s f_m(t) \tag{6.4}$$

where f_{s0} is the nominal carrier frequency and $f_s(t)$ is the instantaneous carrier frequency which is deviated by the function of $f_m(t)$ and the maximum value of Δf_s.

So, the phase of each harmonic in (6.1) can be replaced by:

$$\theta_{mn} = 2\pi \int_0^t f_s(t)d\tau = 2\pi(mf_{s0} + nf_o)t + 2\pi m\Delta f_s \int_0^t f_m(\tau)d\tau \tag{6.5}$$

Function $f_m(t)$ is the periodic function with frequency of f_m and can be represented by Fourier series. Final harmonic spectrum of $g(t)$ with periodic CFM can be expressed by triple Fourier series as below:

$$G(t) = \sum_{l=-\infty}^{\infty} \sum_{m=0}^{\infty} \sum_{n=-\infty}^{\infty} C_{lmn} e^{(j2\pi(lf_m + mf_s + nf_o)t)} \tag{6.6}$$

It can be seen from (6.6) that distinct harmonics appear at the combination of multiples of fundamental frequency f_o, the nominal carrier frequency f_s and the modulating frequency of carrier frequency, f_m.

Recently, another class of periodic CFM has been proposed in the literature [176]. In this method, the periodic function is derived such that the probability density function (pdf) of the carrier frequency follows a specific distribution profile. First, the ruling differential expression is derived based on the relationship of switching frequency ($f(\theta)$) and its derivative ($f'(\theta)$) with the distribution density function ($D[f(\theta)]$). By defining the upper and lower bound of switching frequency, denoted by f_{cu} and f_{cl} respectively, the carrier frequency bound can be divided into finite equal sets. The pdf of the switching frequency indicates how many times each frequency set is repeated relative to the total number of times that frequency sets are chosen in a fundamental period.

For simplicity, let us consider an increasing linear switching frequency function, i.e. linear $f(\theta) \propto |k|\theta$. As the switching frequency increase, i.e. switching period

decreases, the number of times that the respective frequency set is chosen, increases. So, the higher the switching frequency, the higher is the pdf, i.e. $D[f(\theta)] \propto f(\theta)$. In order to understand the relationship between $f'(\theta)$ and $D[f(\theta)]$, let us assume two linear switching frequency function with different slopes ($|k_1| > |k_2|$). In a fixed period of time, more frequency sets are available with the higher slope function, $|k_1|$. So, the number of samples from each frequency set will be lower when the slope is higher. In other words, the density function is inversely proportional to the derivative of the switching frequency function, i.e. $D[f(\theta)] \propto 1/f'(\theta)$. So, with k being the scale factor, the differential equations for uniform, normal and exponential distribution density functions are formulated in (6.7).

$$k\frac{f(\theta)}{f'(\theta)} = \frac{1}{f_{cu} - f_{cl}} \tag{6.7a}$$

$$k\frac{f(\theta)}{f'(\theta)} = \lambda \exp\left(-\lambda f(\theta)\right) \tag{6.7b}$$

$$k\frac{f(\theta)}{f'(\theta)} = \frac{1}{\sqrt{2\pi\sigma^2}} \exp\left[-\frac{(f(\theta)-\mu)^2}{2\sigma^2}\right] \tag{6.7c}$$

In order to solve (6.7) and obtain the switching frequency function, boundary conditions are required. The boundary conditions can be selected such that a certain design criteria is satisfied. In this case, reduced switching power loss within a fixed frequency range is taken into account. The switching loss is proportional to the switching frequency. So, the switching loss can be minimized when the minimum switching frequency (f_{cl}) coincides with the maximum current value and vice versa. In a three phase inverter, the maximum value of three phase current should be considered. This has been shown in Fig. 6.5. It can be seen that the switching frequency

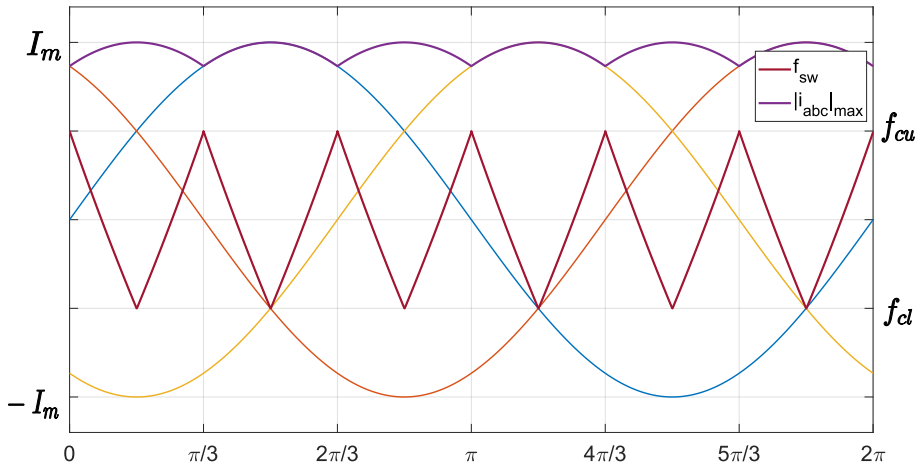

Figure 6.5: Relationship between the current and the switching frequency.

function should be solved only between 0 and $\pi/6$. So, the boundary conditions can be set as below:

$$\begin{aligned} f(0) &= f_{cu} \\ f(\frac{\pi}{6}) &= f_{cl} \end{aligned} \tag{6.8}$$

Fig. 6.6 demonstrates the resulting carrier frequency functions for three common distribution based PCFM.

6.2.2 Random PWM

In a random modulation, one of the parameters is chosen randomly confined to a specific interval. Although the random number usually follow a uniform distribution, it is not limited to only uniform distribution. Three major parameters of a PWM pulse are the pulse period (T_s), the phase shift (ϵ), and the pulse width (D), as shown in Fig. 6.4. The most effective solution is shown to be the random switching frequency

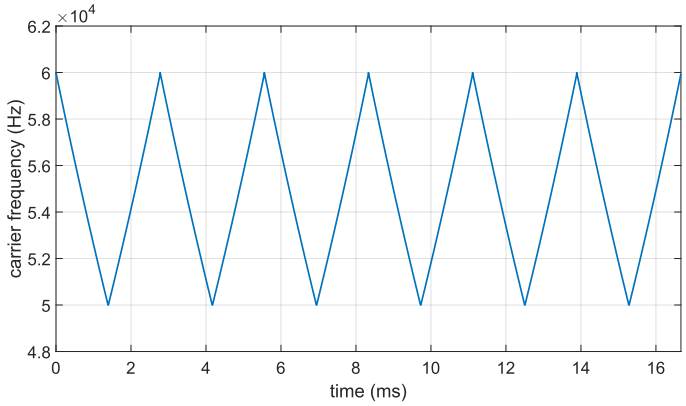

(a)

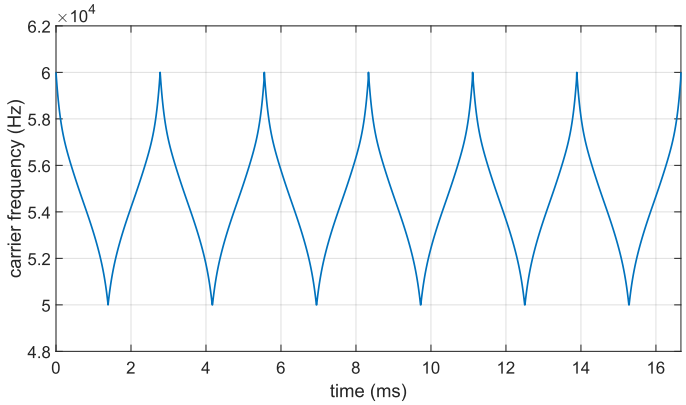

(b)

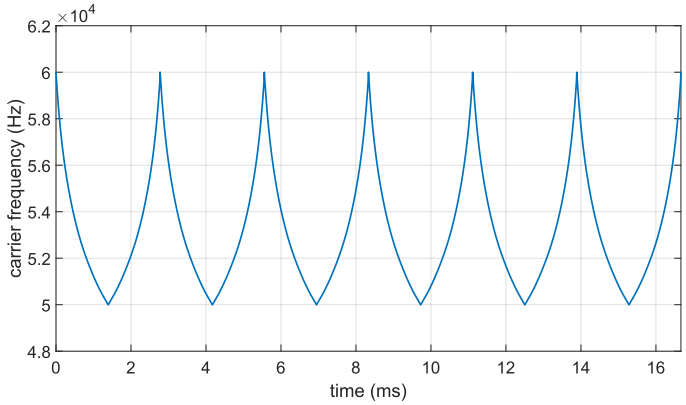

(c)

Figure 6.6: Carrier frequency functions of distribution-based PCFM a) uniform b) normal and c)exponential.

that will be applied here [177].

It has been shown in (6.6) that the harmonic spectrum of PCFM contains distinct harmonics at the combination of multiples of fundamental frequency f_o, the nominal carrier frequency f_s and the modulating frequency of carrier frequency, f_m. In the harmonic spectrum of a randomly modulated signal, an auto correlation term will appear [178, 179]. Power spectrum density is used instead of power spectrum and can be calculated as:

$$\begin{aligned} S_g(f,R) = \frac{1}{E\{T_k\}}[E\{|G(f)|\}^2 \\ + 2Re(\frac{E\{G(f)e^{j2\pi fT_k}\}E\{G^*(f)\}}{1-E\{e^{j2\pi fT_k}\}})] \end{aligned} \tag{6.9}$$

$E\{.\}$ is the expected value of the quantity inside the bracket. The instantaneous switching period in denoted by T_k and R determines the randomness of the random process. The pdf of T_k usually follows the uniform distribution:

$$P(T_k) = \frac{1}{T_2 - T_1} = \frac{1}{RT_s} \tag{6.10}$$

where $T_1 = 1/f_{cu}$ and $T_2 = 1/f_{cl}$ are the minimum and maximum switching periods, respectively. As it can be seen in (6.9), RPWM spreads the power over the frequency spectrum as opposed to PCFM that only contains discrete harmonic spectrum. Fig. 6.7 shows the harmonic spectrum of the conducted emissions of the ANPC when constant carrier frequency modulation, random carrier frequency, and sinusoidal periodic modulation are applied.

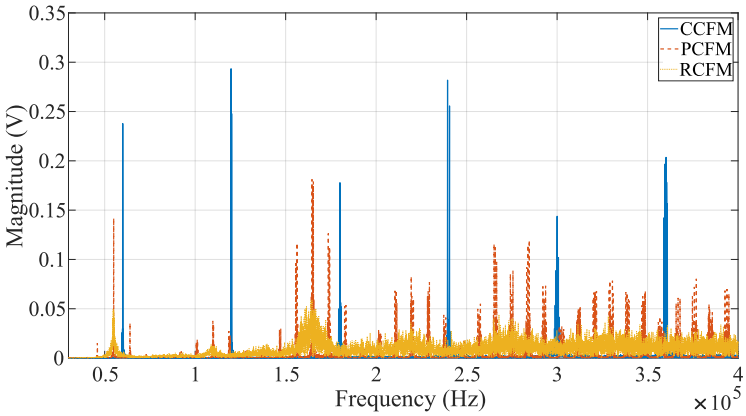

Figure 6.7: Harmonic spectrum of EMI conducted emissions of the ANPC.

6.3 EMI receiver model

Apart from limits and standards, EMC regulations also define a standard measurement procedure. A conducted EMI measurement setup consists of a Line Impedance Analyzer Network (LISN) and an EMI receiver. LISN is placed between the device under test and each of the input power cords. Two LISNs are required to measure the ANPC conducted emissions since the dc input is used. The main function of LISN is to define a known line impedance for the DUT looking into the power network. It also filters the noises coming from the network.

Most of the EMI receivers, normally a spectrum analyzer, work based on the swept-tuned method. In this method, the signal is mixed with a swept local oscillator. Then, it goes through a band-pass filter with a standard resolution bandwidth (RBW). Lastly, a peak, average or quasi-peak detector is used to obtain the final measured values. Fig. 6.8 shows the calculation process that is used here to model the behaviour of a swept-tuned based spectrum analyzer. In the first step of this algorithm, Fast Fourier Transform (FFT) is used to transfer the time domain measured signal ($g(t)$)

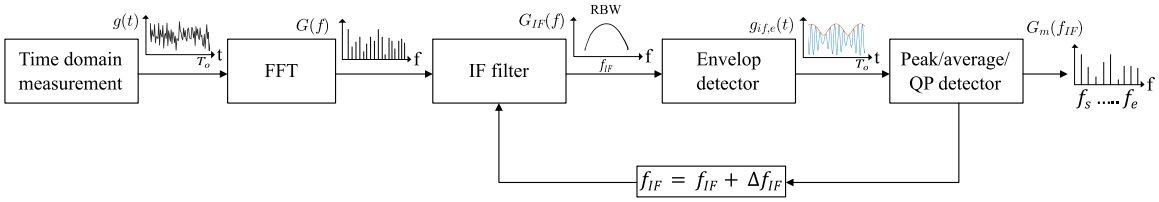

Figure 6.8: The calculation process to model a swept-tuned spectrum analyzer.

to the frequency domain ($G(f)$). Next, the intermediate frequency filter narrows down the broadband spectrum based on the defined RBW and the output is denoted by $G_{IF}(f)$. Using the magnitudes and phases of the selected frequency band, the time domain waveform of the calculated narrowband signal is rebuilt in a fundamental cycle (T_o). In the detection section, first, an envelope detector finds the envelope of the time domain narrowband signal which is denoted by $g_{if,e}(t)$. Then, a peak, average or quasi-peak detector can be used to find the amplitude of output spectrum at the center frequency of IF filter, f_{IF}. Then, the IF frequency is incremented by Δf_{IF} and the calculation is repeated until the whole frequency range of interest ($f_s - f_e$) is covered.

The bandwidth of the intermediate filter is defined by EMC regulations and plays an important role in the final measured emissions. It basically adds up the harmonics that fall within the RBW and puts them together in the center frequency. So, the output measured spectrum will not be the same as the output of the FFT. The attenuation of this filter has a Gaussian characteristics. The standard RBW of conducted emissions in the frequency range of 150kHz-30MHz is 9kHz. Table 6.1 shows the FCC standard minimum 6 dB resolution bandwidths where the filter response is reduced by 6 dB relative to the center frequency. The Gaussian filter gain of the spectrum analyzers is shown in Fig. 6.9. It is worth mentioning that in this thesis, $2RBW$ is

Table 6.1: FCC minimum 6 dB resolution bandwidth (RBW_6)

Band	**Frequency range**	**RBW**
A	9 kHz-150 kHz	200Hz
B and C	150 kHz-30 MHz	9kHz
D	30 MHz-a GHz	120 kHz
E and beyond	>1 GHz	1 MHz

considered as the effective bandwidth of the filter since the attenuation beyond this bandwidth is too high, higher than 25 dB, hence negligible.

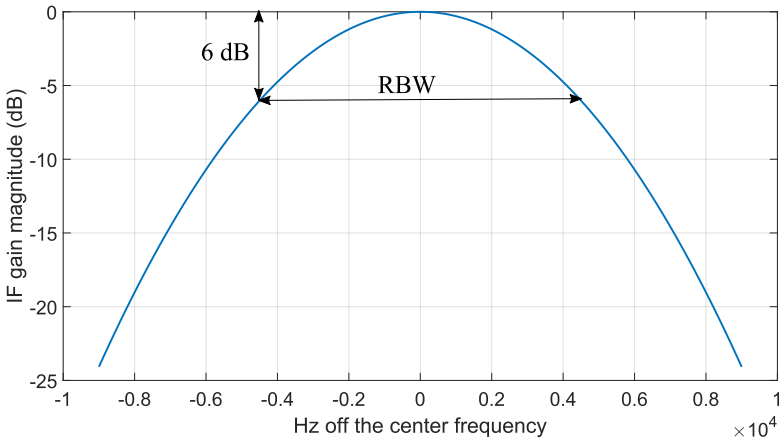

Figure 6.9: The Gaussian intermediate filter gain.

In the swept-tuned spectrum analyzer (STSA), each frequency is calculated at a specific time. So, the calculation process is time consuming. This method is also known as the frequency domain EMI measurement. Time domain EMI measurement is another approach proposed in the literature [127, 136] and also applied in commercial EMI receivers. This method is based on the Short Time Fourier Transform (STFT). As the signal is measured in the time domain, the segments of signal are transferred to the frequency domain by FFT. In this manner, all the frequencies are

calculated in parallel leading to a much faster calculation process. The TDEMI measurement process is shown in Fig. 6.10. The first step is to digitize the measured signal and divide the signal into equal chunks of time. The frequency response of the window function is the same as the IF filter used in the STSA method to emulate the same effect. It is worth mentioning that the signal chunks are overlapped to improve the calculation precision. Then, the FFT is applied to all the signal chunks at the same time. The process can be expressed as:

$$G_w(m,k) = \sum_{n=0}^{N_w-1} g(n)w(n - m(1-o_f)N)e^{-j2\pi k\frac{n}{N_w}} \tag{6.11}$$

where $k = 1, 2, ..., N$ is the frequency index and $m = 1, 2, ..., M$ indicates the number of time frames. Window function is denoted by w with the length of N_w. The overlapping factor is shown by o_f which is normally between 0.8-1. The output of the FFT block in Fig. 6.10, is a $[M \times N]$ matrix where each column contains M values for a specific frequency (see (6.12)). The detector block, easily calculates the peak or average value using M components for each frequency.

Fig. 6.11 demonstrate an example of comparison between the output of simple FFT and the processed signal using two mentioned algorithms. It can be seen that the FFT cannot represent the measured EMI by EMI receivers. Furthermore, the calculated spectrum by STSA and TDEMI methods are in good agreement. In this case, the calculation time of STSA is around 2 hours whereas the TDEMI can provide a similar result in a much shorter time, in the range of a couple of minutes. So, TDEMI is used in the rest of the thesis where multiple calculations are required to examine

different PWM techniques.

$$G_w(m,k) = \begin{bmatrix} G_w(1,0) & G_w(1,1) & \cdots & G_w(1,N) \\ G_w(2,0) & G_w(2,1) & \cdots & G_w(2,N) \\ \vdots & \vdots & \ddots & \vdots \\ G_w(M,0) & G_w(M,1) & \cdots & G_w(M,N) \end{bmatrix} \tag{6.12}$$

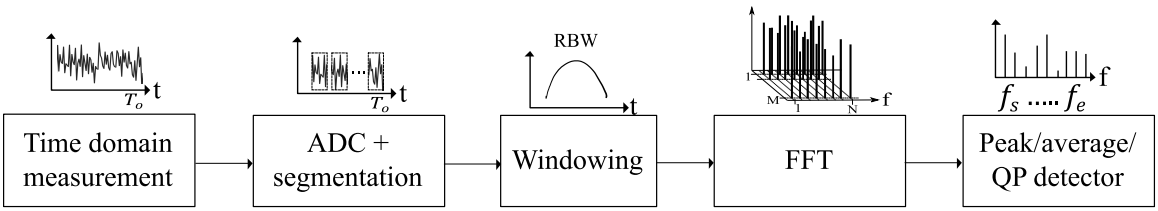

Figure 6.10: The calculation process of time domain EMI measurement.

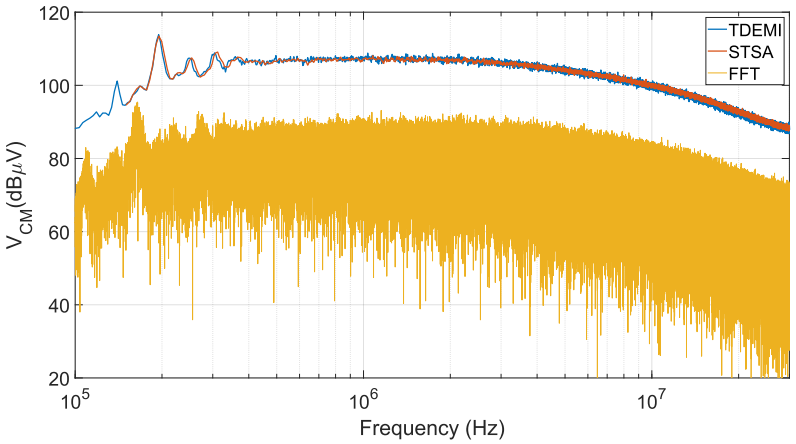

Figure 6.11: Comparison between the FFT output, swept-tuned spectrum analyzer, and TDEMI.

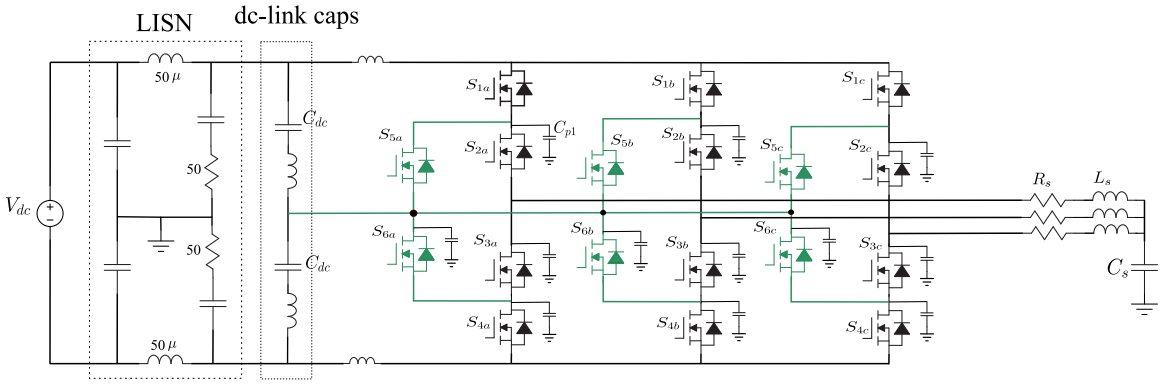

Figure 6.12: The detailed model of the ANPC considering main parasitic elements.

6.4 Evaluation of spread spectrum modulations

In order to evaluate the performance of different SS modulation techniques, a detailed model of the ANPC is required. The designed three level SiC-based ANPC for EV applications is shown in Fig. 6.12 and some of the key parameters are listed in Table 6.2. A physics-based model of the SiC MOSFET (UJ4C075018K4S from United SiC), as the main EMI source, is derived using characteristics extraction tools. The performance of the extracted MOSFET model is evaluated in a half bridge circuit and compared to the datasheet values. Table 6.3 summarizes the comparison results that show a good agreement between the simulation and the datasheet. Next, the parasitic elements of different parts of the circuit should be considered. In Fig. 6.12, the main parasitics are shown including the stray inductance of the dc-link capacitors, the stray inductance of the Printed Circuit Board (PCB) traces, and the stray capacitance between the MOSFETs and the heatsink.

The nominal carrier frequency is 60 kHz and the minimum allowable carrier frequency is 50 kHz. The minimum frequency is set according to the dc-link capacitor

Table 6.2: ANPC parameters

parameter	**description**	**value**
$P_{o,c}$	Continuous output power	70 kW
$P_{o,T}$	Transient output power (10 s)	120 kW
f_{s0}	Nominal carrier frequency	60 kHz
Δf_s	Maximum deviation of Carrier frequency	10 kHz
f_o	Output frequency	60 Hz
V_{dc}	dc-link voltage	600 V

Table 6.3: Switching characteristics of the SiC Mosfet (sim: simulation result, data: datasheet value)

		T_{on} (ns)	T_{off} (ns)	E_{on} (μJ)	E_{off} (μJ)	Q_{RR} (nC)
T=150	Data	52	172	453	304	109
	Sim	53	174	421	305	109
T=25	Data	48	163	407	255	102
	Sim	49	161	385	254	103

limitations. In this chapter, only downspread approach is implemented, i.e. the carrier frequency is always reduced. The main reason for such approach is that the EMI emissions are proportional to the switching frequency. So, there is no benefit in increasing the switching frequency. Furthermore, as the carrier frequency increases, the computation time decreases which may be in contrast with the original design specifications [180]. In the following, the performance of the ANPC is evaluated under different SS modulation techniques. As mentioned in Section II, SS modulation techniques have different classifications. In the periodic modulations, sinusoidal waveform-based, and three common distribution based methods are applied to the detailed model of the ANPC. Furthermore, constant and random carrier frequency modulations are also applied and compared with each other.

6.4.1 Conducted EMI emissions

Two LISN are used to measure the conducted EMI emissions of the ANPC, as show in Fig. 6.12. Fig. 6.13 shows the common mode conducted EMI emissions of the ANPC for periodic, random and constant carrier frequency modulation. It is worth mentioning that the effect of RBW is demonstrated in Fig. 6.13a. Although the FFT outputs indicate maximum suppression of around $20dB\mu V$, the measurement results considering the effect of EMI receivers show that the suppression is limited to around only $7dB\mu V$.

In order to closely evaluate the EMI performance of the modulation methods, a filter-based approach is applied. In spite of applying different suppression methods, EMI filters are usually required to comply with the EMC regulations. There are a few international organizations that have developed standards for commercial vehicles. The U.S. Society of Automotive of Engineering (SAE), International Organization for Standardization (ISO), and the International Special Committee on Radio Interference (CISPR) are among them. The standards usually regulate the EMC requirements in the vehicle level and/or the component/module level. CISPR25 deals with the radio disturbance characteristics for the protection of receivers used on board vehicles, boats and on devices and ensures that the components do not interfere with the on-board devices.

The EMI filters are designed to provide enough suppression for EMC compliance in the whole frequency range of interest. The filters are normally bulky and their size will be minimized as the required suppression is lowered. Therefore, the maximum required suppression is the basis of the design. In this chapter, the CISPR25 limits are compared to the EMI emissions and the maximum required suppression in the

frequency range of 150 kHz-30 MHz is chosen as the evaluation index.

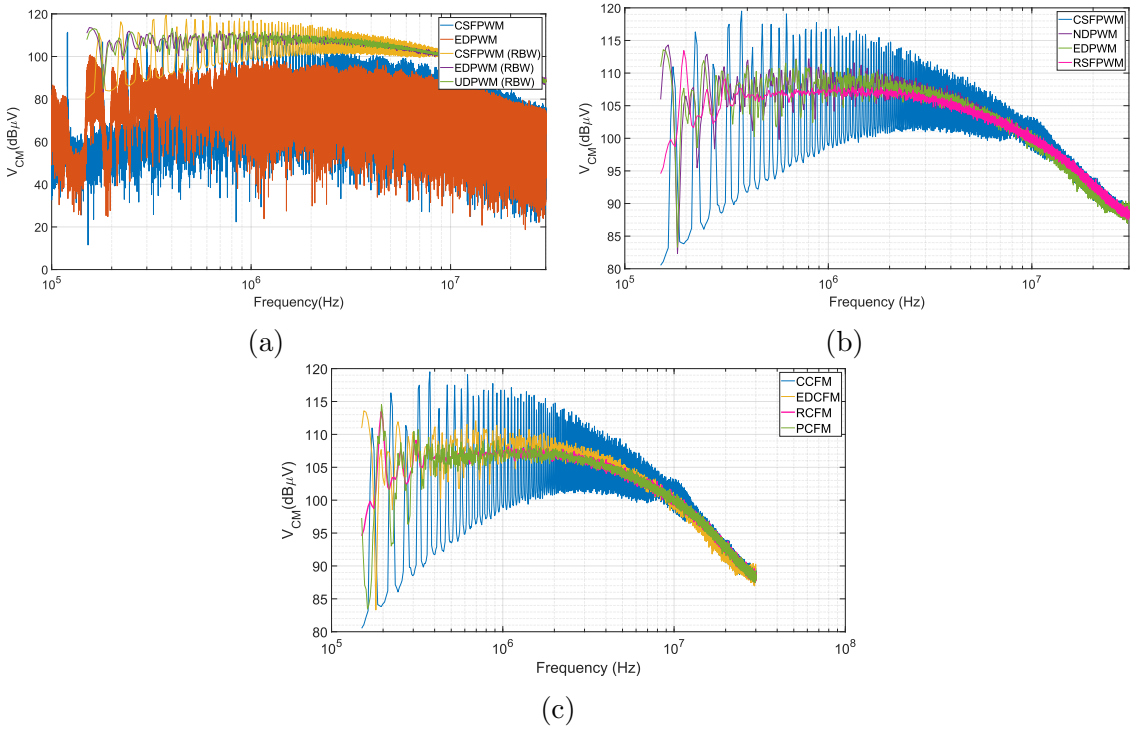

Figure 6.13: Common mode emissions of the ANPC applying different modulation methods.

In the first category of SS modulation methods, sinusoidal PCFM is applied to the ANPC. According to (6.4), the carrier frequency varies in time as follows:

$$f_s = f_{s0} + \Delta f_m \sin(2\pi f_m t) \tag{6.13}$$

The ratio between the frequency deviation and the modulating frequency, also known as modulation index, is defined as $\beta = \frac{\Delta f_m}{f_m}$. It has been shown that the theoretical suppression effect increases for higher modulation indices [181]. However, in practical applications, the effect of RBW and hardware limitations need to be considered.

Higher modulation index means higher deviation (Δf_m) and lower modulation frequency (f_m). PCFM methods disperse each concentrated harmonic into side bands with smaller magnitude that are f_m apart. As f_m decreases to values lower than the RBW, the effectiveness of the modulation drops since the successive harmonics fall into the same RBW. In this chapter, the maximum frequency deviation is used with different modulation frequency to investigate the effect of the EMI receiver. Table 6.4 summarizes the maximum suppression that each SS modulation method provides in comparison to the constant carrier frequency modulation. It can be seen that although the magnitude of individual harmonics is lower for lower f_m, $f_m = 9kHz$ provides the highest suppression in practice. Therefore, for a specific frequency deviation, maximum suppression level can be achieved when the modulation frequency is the same as the bandwidth of the EMI receiver, $f_m = RBW$. Furthermore, a higher frequency deviation is desirable which is more achievable for higher nominal carrier frequencies.

Three distribution-based PCFM; uniform, normal, and exponential distributions; with the same modulation index provide a similar suppression level. Two random CFM with different frequency deviation Δf_m is also applied to the ANPC. The simulation results that the RCFM is the most effective method providing the highest suppression.

6.4.2 Overall evaluation

Apart from the effective suppression level, other performance indices of the system should also be considered for a comprehensive evaluation. The output current THD and the efficiency of the inverter are taken into account. The simulation results are

Table 6.4: Maximum suppression of CM EMI emissions for different SS modulation methods

modulation method	**conditions**	**suppression** ($dB\mu V$)
Sinusoidal PCFM	$f_m = 360Hz$	6.4
	$f_m = 1080Hz$	8.3
	$f_m = 9kHz$	10.3
	$f_m = 12.6kHz$	9
Distribution-based PCFM	Uniform	7
	Normal	7
	Exponential	7.1
Random CFM (RCFM)	$\Delta f_m = 10kHz$	12
	$\Delta f_m = 5kHz$	9

summed up in Table 6.5. It is apparent that the lower carrier frequency lowers the switching loss leading to higher efficiency. In all cases, the average carrier frequency is lower than the CCFM due to the down-spread approach. So, the efficiency of the inverter in all SS methods is higher than CCFM. Meanwhile, a higher carrier frequency produces a smoother output current. Therefore, the output current THD is the highest when CCFM is applied. It is worth mentioning that the current THD for all cases are within 0.77%. The RCFM with $\Delta f_m = 10kHz$ has the best suppression performance and the lowest power loss. However, it produces the highest current THD at the same time. The distribution-based PCFM methods have similar results, EDCFM being the most effective.

The implementation complexity is another important factor to be considered. In general, the periodic CFM methods are easier to implement in comparison to the random techniques. The main reason is the complexity of random number generation.

Table 6.5: Current THD and power loss of the ANPC for different SS modulation methods

modulation method	**conditions**	**Current THD (%)**	**Power loss (W)**
CCFM	-	1.99	1550
Sinusoidal PCFM	$f_m = 360Hz$	2	1520
	$f_m = 1080Hz$	2.02	1515
	$f_m = 9kHz$	2.4	1510
	$f_m = 12.6kHz$	2.7	1500
Distribution-based PCFM	Uniform	2.02	1512
	Normal	2.01	1515
	Exponential	2.05	1510
Random CFM (RCFM)	$\Delta f_m = 10kHz$	2.77	1500
	$\Delta f_m = 5kHz$	2.15	1535

6.5 Experimental evaluation

6.5.1 Experimental setup

The experimental setup is shown in Fig. 6.14. The input dc power supply is connected to the inverter through the LISNs. Two single path vehicle LISN, model number NNBM 8124 by SCHWARZBECK is used for each line. An aluminum sheet is laid beneath the setup as the ground plane. The LISNs are connected to the ground plane through short braided strips to ensure a very small impedance coupling. Short cables are used to connect the front panel of the LISNs to the inverter. RF output of the LISNs are connected to the EMI receiver. In this setup, SIGLENT 3021X plus spectrum analyser is used as an EMI receiver.

6.5.2 EMI receiver model verification

First, the performance of the developed EMI receiver model should be verified. Therefore, the SA measurement results are compared to the results obtained by the TDEMI

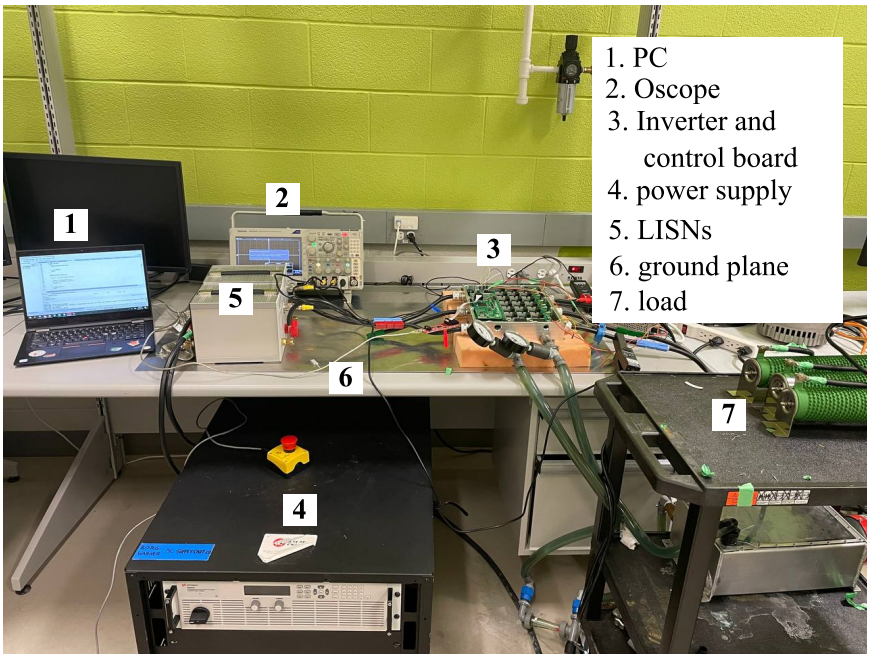

Figure 6.14: The experimental setup of the 3-L ANPC.

algorithm. To do so, one of the LISN voltages are measured by Tektronix MDO4024C oscilloscope with the sampling rate of 100 Ms/s. The measured time domain voltage is fed to the TDEMI algorithm and the comparison results are shown in Fig. 6.15. In this figure, the SA measurement (in frequency domain), the fft of time domain measurement by the oscilloscope, TDEMI model output, and the frequency domain measurement by the oscilloscope are shown. It can be seen that the results are in good agreement. Therefore, the developed TDEMI model can be applied to the time domain measurements of the oscilloscope.

6.5.3 Detailed model verification

In the next step, the performance of the detailed model of the system should be evaluated. In order to do so, the DM and CM emissions of the inverter are measured

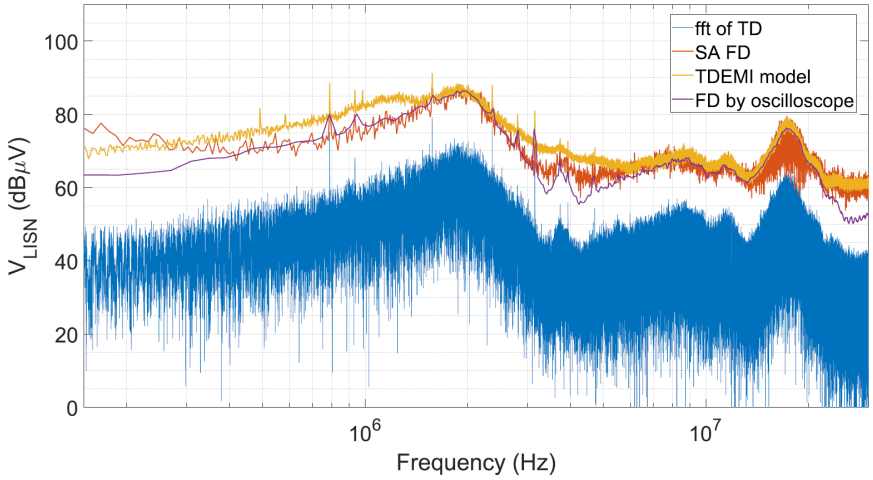

Figure 6.15: Comparison between the measurement results of the SA and the Oscilloscope.

Table 6.6: Experimental parameters

symbol	description	value
V_{dc}	input DC voltage	100 V
f_{sw}	constant switching frequency	60 kHz
Δf_{sw}	switching frequency variations	10 kHz
f_m	modulation frequency of PCF	9 kHz
m	modulation index	0.75
R	load	10 Ω

and compared to those obtained from the simulation. The comparison results are shown in Fig. 6.16.

6.5.4 Experimental results

The experimental parameters are shown in Table 6.6. Constant carrier frequency PWM along with two typical spread spectrum modulation, sinusoidal periodic and random carrier frequency modulation, are applied to the inverter. Output line voltages, U_{ab} and their harmonic content are depicted in Fig. 6.17. It can be seen that line-to-line voltages are similar to each other with insignificant difference in total

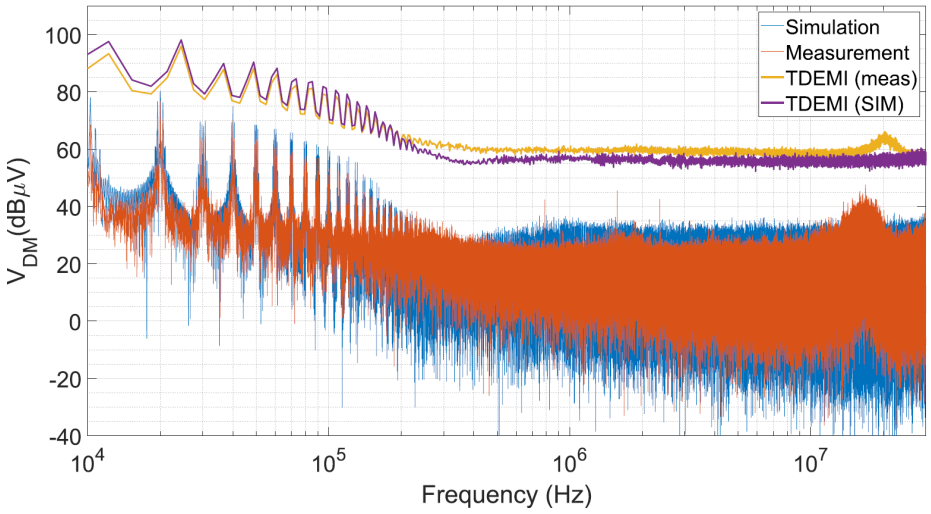

(a)

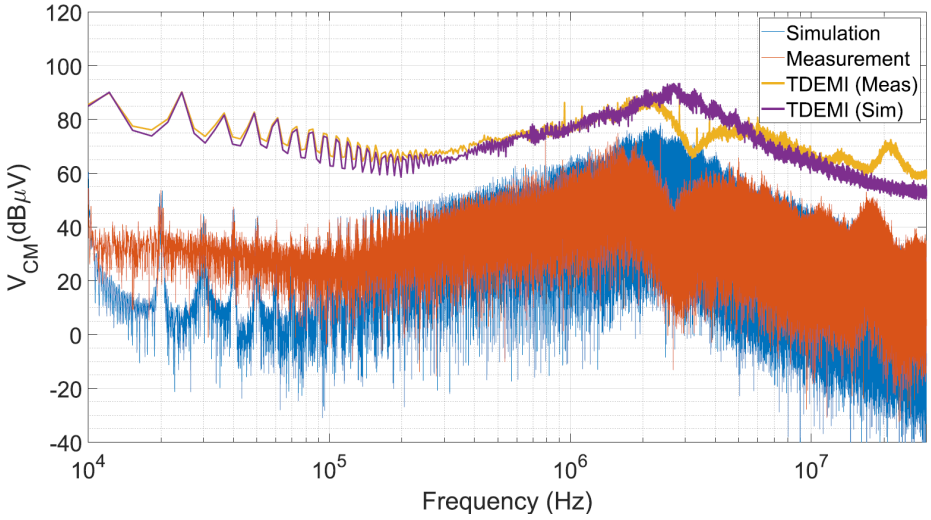

(b)

Figure 6.16: Conducted emissions of the inverter, measurement and simulation results a) DM, b) CM.

harmonic distortion values. However, the harmonic spikes are notably reduced when spread spectrum modulation techniques. Furthermore, the conducted EMI emissions are effectively spread between the frequencies such that the maximum EMI noises are reduced, as shown in Fig. 6.18.

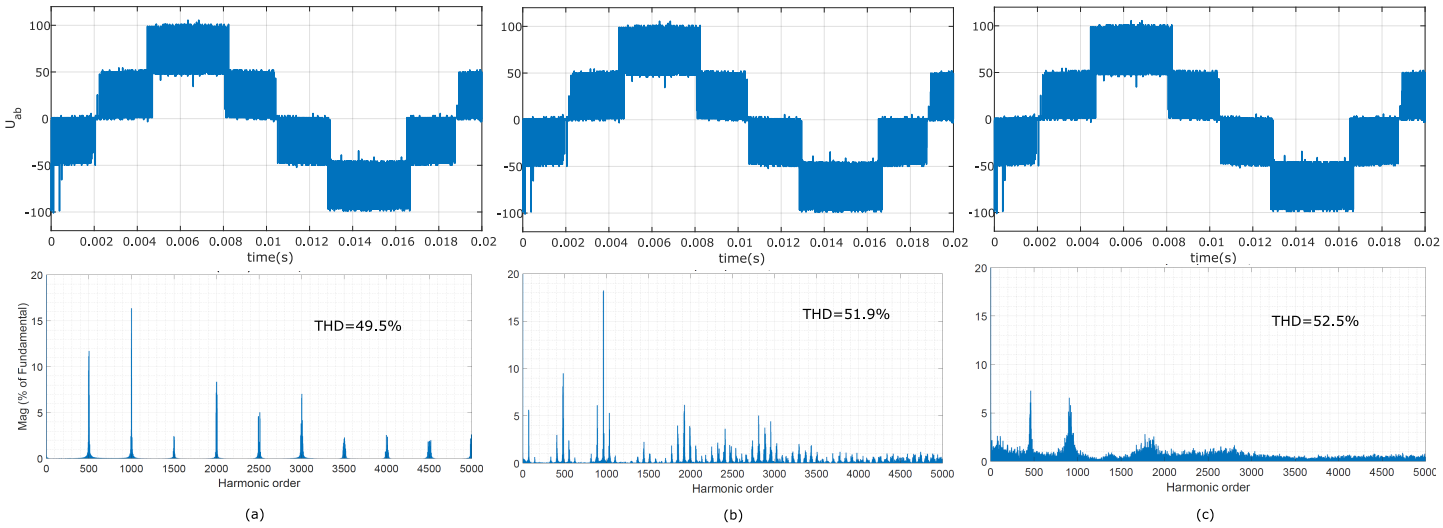

Figure 6.17: Measured line-to-line voltages with harmonic spectrum a) CCFM, b) PCFM, c) RCFM.

6.6 Summary

This chapter investigates various spread spectrum modulation methods for an ANPC inverter system with RL load. First, a time domain EMI simulation model is implemented to model the EMI receiver. It is shown that the TDEMI method can provide a similar results in comparison with the frequency domain method. Meanwhile, TDEMI is a much faster calculation method that enables us to consider the effect of EMI receiver bandwidth in the simulation results. Three categories of SS modulation techniques are studied: sinusoidal PCFM, CCFM, distribution-based PCFM,

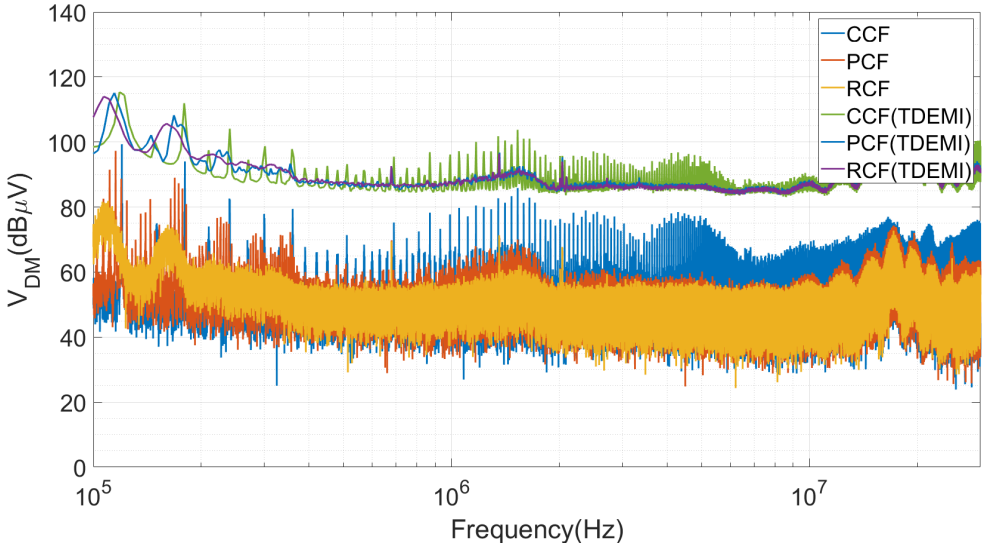

(a)

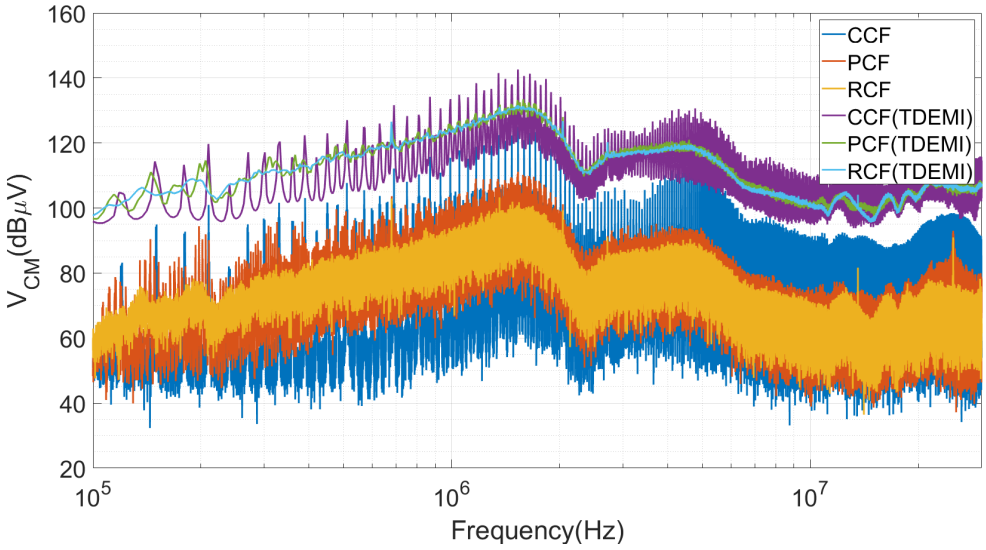

(b)

Figure 6.18: Conducted emissions of the inverter, measurement results a) DM, b) CM.

and RCFM.

The performance of the ANPC is evaluated under various modulation methods. Without considering the conducted emissions, CCFM has the best performance in terms of output current THD. There is a tradeoff between the current THD and the inverter efficiency. The distribution-based PCFM methods have similar performance which are also similar to the sinusoidal PCFM with low modulation frequency. The reason is the low modulation frequency of the distribution-based methods. Taking into account the effect of RBW, there is an optimum point where the PCFM methods can provide their best performance. Random CFM approaches can provide a smooth harmonic spectrum with the highest EMI suppression. However, the implementation of RCFM methods are more complex compared to PCFM.

Chapter 7

An Improved Carrier Based PWM Strategy with Reduced Common Mode Voltage for a Three Level NPC Inverter

Double modulation wave carrier-based pulse width modulation (CBPWM) is a solution for eliminating the deviations of the neutral point voltage (NPV) in three-phase neutral point clamped inverters. In this chapter, a new hybrid CBPWM strategy is proposed that not only eliminates the neutral point voltage oscillations but also reduces the common mode voltage (CMV) by half. Furthermore, the harmonic content of the output voltage is reduced by adjusting the modulation waves based on the location of the reference vector in the space vector diagram. An active neutral point voltage controller is also presented and applied in order to maintain the performance

of the modulation strategy under the NPV perturbations. The performance of the proposed algorithm is compared to the conventional CBPWM and another CBPWM with reduced CMV that is already available in the literature. Finally, experimental results are presented to evaluate the proposed modulation strategy.

7.1 Introduction

A three-level neutral point clamped inverter is amongst the most common multi-level inverters used in medium voltage industrial applications. Compared with the two-level inverter, lower harmonic content and reduced voltage stress across the semiconductor devices are the main benefits [182]. Various modulation techniques have been proposed in the literature that are generally categorized as either carrier-based pulse width modulation (CBPWM) or space vector PWM (SVPWM).

Despite the simple implementation, conventional CBPWM leads to low frequency fluctuation of the neutral point voltage (NPV). NPV deviations lead to the distortion of output voltage and current and induce larger overvoltages across the switches, which may cause a permanent damage. In order to compensate for the NPV fluctuations, bigger dc-link capacitors can be used. As another solution, two separate dc sources or split batteries can be used to stabilize the voltage of the neutral point [183]. To minimize the neutral point fluctuations, feedback control can be implemented where the neutral point voltage is detected and controlled [184]. All the solutions demand more hardware costs. As a more cost-effective solution, improved CBPWM or SVPWM strategies are proposed in the literature.

Busquets et al. adopted a nearest three virtual space vector PWM (VSVPWM) approach to balance the NP voltage [185]. The idea is to maintain a zero average

NP current in a switching period. This is achieved by combining small vectors and medium vectors to create virtual medium vectors. Although zero average NP current can be achieved in all operating points, harmonic content and the effective switching frequency are increased. Besides, in practical applications, balanced NP voltage cannot be maintained due to non-ideal operating conditions such as the leakage current flowing in the ground, unequal dc link capacitors, and the differences in switching behavior of the devices [186]. Therefore, an active NPV controller is required. The authors realize a closed loop controller in [186], and an optimization is performed to lower the harmonic content of the output voltage in [187]. The effect of unbalanced capacitors can be taken into account by repartitioning the virtual vector diagram [188, 189].

A carrier based PWM based on the concept of virtual vectors has also been proposed, which is simple and easy to implement [190, 191]. Active neutral point controller for this strategy is developed in [192]. In all of the previous researches, the main objective is to maintain a low NPV oscillation through zero average NP current while the generated common mode voltage is disregarded.

High common mode voltage (CMV) induces more leakage current and increases the electromagnetic interference (EMI) emissions. In motor drive applications, CMV results in shaft voltage and bearing current that may damage the motor insulation [193]. So, CMV suppression is an important issue that needs to be addressed.

In the space vector diagram (SVD), each switching state will generate a specific CMV. By properly selecting the space vectors, CMV can be either eliminated or reduced [194]. Keeping that in mind, an efficient solution is to use the vectors that would generate lower CMV to build the virtual vectors [195, 196]. Although reduced

CMV virtual space vector PWM (RCMV_VSVPWM) strategy in [195] effectively reduces the CMV, the self balance ability is lost, and an active NPV controller is required all the time. In another RCMV_VSVPWM approach, self balance capability is maintained at the expense of increased harmonic content [197]. An improved version of VSVPWM is introduced in [198] to reduce the NPV oscillation and CMV simultaneously. However, an active NPV controller is not realized, the CMV suppression is not achievable for all operating points, and the algorithm is not easy to implement.

A double modulation wave CBPWM with reduced CMV is introduced in [199] which is easy to implement. The major issues of this strategy are high harmonic content, and the incompetent NPV controller that fails to maintain the CMV suppression in all operating points. Furthermore, the effectiveness of this modulation deteriorates in lower power factors. In this chapter, a hybrid carrier based PWM technique is introduced along with an active NPV controller that ensures effective CMV suppression and elimination of NPV fluctuations at all operating points. Furthermore, this modulation is relatively easy to implement and the harmonic content of the output voltage is improved.

7.2 NP current and CMV of the three-level NPC

A three-level Active Neutral Point Clamped (ANPC) inverter is shown in Fig. 7.1(a). In comparison with the NPC inverter, the diodes are replaced with two MOSFETs, S_5 and S_6. This feature can be used to evenly distribute the power loss among the switching devices. Note that the space vector diagram remains the same as depicted in Fig. 7.1(b). The corresponding switching states of phase A are listed in Table 7.1.

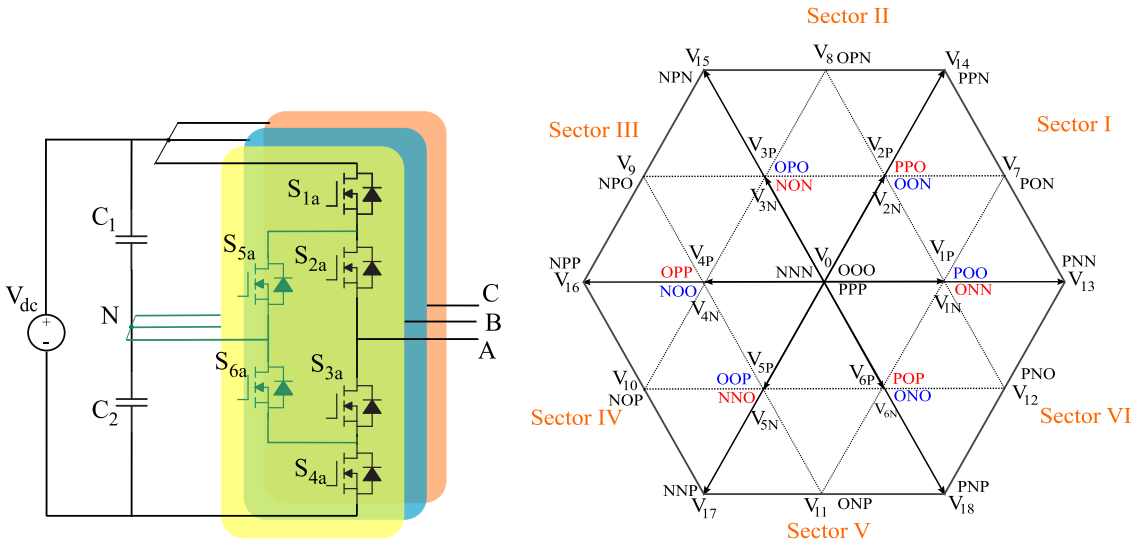

Figure 7.1: Topology of the ANPC and its space vector diagram.

Table 7.1: Switching states of a 3L-ANPC

Switching State		Device switching status						Output phase voltage (V_{AN})
		S_1	S_2	S_3	S_4	S_5	S_6	
[P]		1	1	0	0	0	1	$V_{dc}/2$
[O]	OU1	0	1	0	0	1	0	0
	OU2	0	1	0	1	1	0	
	OL1	1	0	1	0	0	1	
	OL2	0	0	1	0	0	1	
[N]		0	0	1	1	1	0	$-V_{dc}/2$

Table 7.2: The effect of medium and small vectors on the NP

meduim vectors		small vectors			
V_7	i_b	V_{1P}	$-i_a$	V_{4P}	i_a
V_{10}		V_{1N}	i_a	V_{4N}	$-i_a$
V_8	i_a	V_{2P}	i_c	V_{5P}	$-i_c$
V_{11}		V_{2N}	$-i_c$	V_{5N}	i_c
V_9	i_c	V_{3P}	$-i_b$	V_{6P}	i_b
V_{12}		V_{3N}	i_b	V_{6N}	$-i_b$

7.2.1 Neutral point current

Two dc-link capacitors, C_1 and C_2, ideally have equal voltages ($V_{dc}/2$). The neutral point voltage balance is essential for the decent performance of the ANPC. Each switching state affects the neutral point voltage depending on whether a phase current flows through the NP or not. Large vectors have no 'O' state, i.e., do not connect any phases to the NP. Therefore, they have no effect on the NPV. Likewise, zero vectors have no effect on the NPV as well. On the other hand, medium and small vectors each have a specific effect on the neutral point current. Table 7.2 shows the neutral point current for the medium and small vectors. It is assumed that the three-phase load is balanced:

$$i_a + i_b + i_c = 0 \tag{7.1}$$

In order to avoid the NPV fluctuations, one solution is to keep the average of the neutral point current in one switching period at zero. It can be mathematically put as:

$$i_{NP} = i_a d_{a,0} + i_b d_{b,0} + i_c d_{c,0} = 0 \tag{7.2}$$

Where $d_{x,0}$ denote the duty ratio of the zero state for phase x, likewise, the duty ratio of the other states is shown by $d_{x,1}$ and $d_{x,-1}$. By comparing (7.1) and (7.2), one can

conclude that as long as the zero state ratio of all phases are equal, the neutral point current is kept at zero, i.e.:

$$d_{a,0} = d_{b,0} = d_{c,0} \tag{7.3}$$

Virtual vectors are a linear combination of medium and small vectors that balance out their effect on the neutral point current. In Fig. 7.2(a), the conventional virtual vectors in sector I is depicted [185]. In the new space vector diagram, large and zero vectors are the same as conventional SVD while V_{VS1}, V_{VS2} and V_{VM2} are the new small and medium virtual vectors. Virtual small vector, V_{VS1} is obtained by an equal combination of the p-type and n-type space vectors, V_{1P}(POO) and V_{1N}(ONN), respectively. When V_{VS1} is applied for a specific period of time, t_1, each of the constitutive vectors, POO and ONN, are active for $t_1/2$. The average neutral point current can be calculated using Table 7.2 :

$$i_{NP} = \frac{t_1/2 \cdot i_a + t_1/2 \cdot -i_a}{t_1} = 0 \tag{7.4}$$

The average neutral point generated by the other small virtual vector, V_{VS2}, is similarly zero. V_{VM1} is an equal share of the medium space vector, V_7(PON), one p-type, and one n-type small vectors, V_{1N}(ONN) and V_{2P}(PPO) respectively. Notice that the generated neutral point current of the constitutive vectors is i_b, i_a, and i_c, respectively. Therefore, the resultant neutral current will be $(i_a + i_b + i_c)/3 = 0$.

As an example, switching sequence, the neutral point current and the NP voltage deviations is graphically shown in Fig. 7.2(b) for the reference voltage shown in Fig. 7.2(a). In this case, the nearest three virtual vectors are V_{14}, V_{VM1}, and V_{VS2}. So, five different space vectors are applied: V_{1N}, V_{2P}, V_{2N}, V_7, and V_{14}. The switching

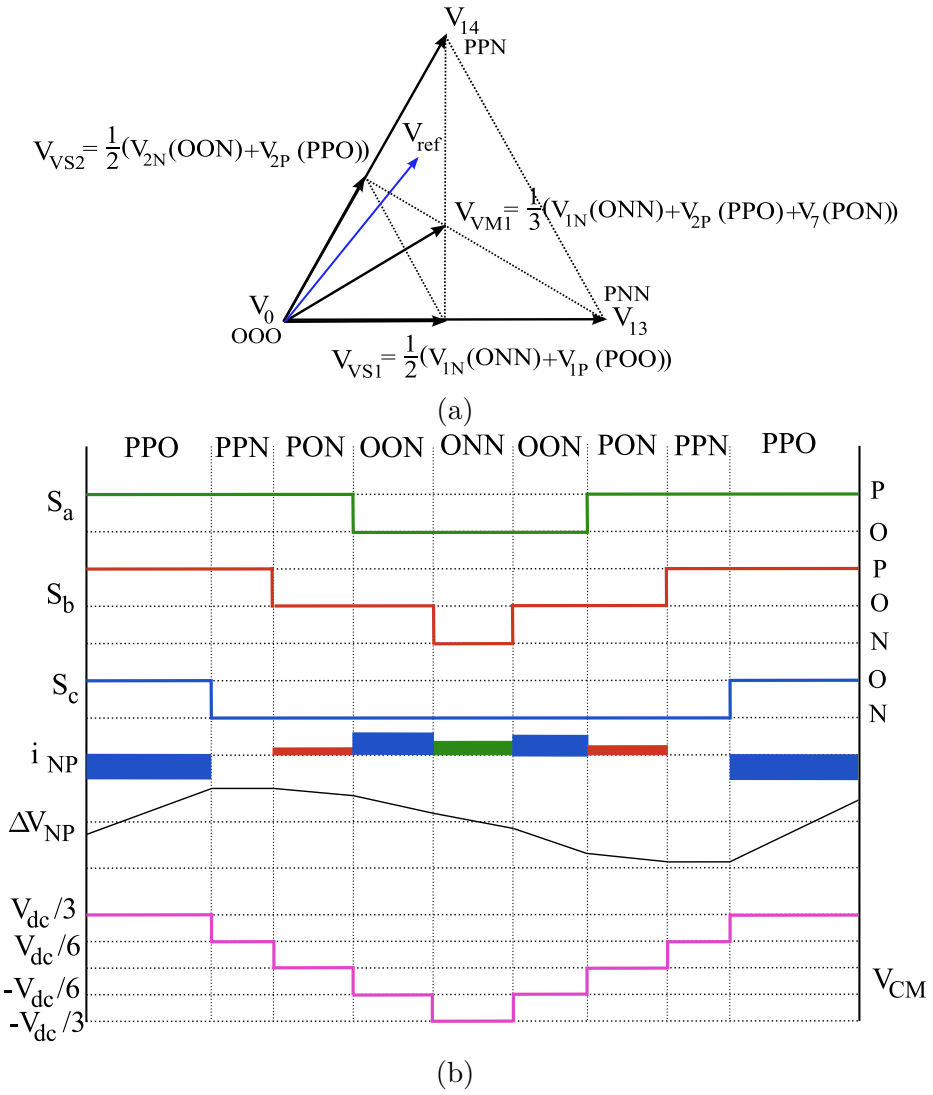

Figure 7.2: a) Virtual space vector diagram in sector I, b) switching sequence of V_{ref}, resultant NP current, the NPV variations, and the generated V_{CM}.

sequence are arranged to minimize the switching power loss. Please note that it is assumed $i_c < 0$, $i_b > i_a > 0$, and $|i_c| > |i_b|$.

In the new virtual space vector diagram, all the vectors have an average NP current of zero. Although various versions of SVD have been proposed in the literature, all of them are based on the concept of zero average NP current.

7.2.2 Common mode voltage

As discussed in the Introduction, CMV induces CM current in the parasitic capacitors resulting in EMI emissions. Moreover, higher CMV leads to higher leakage current that may damage the bearings and the motor insulation. So, the CMV should be analyzed and considered in the design stage.

Common mode voltage in a three level inverter is defined as:

$$V_{CM} = \frac{V_{AN} + V_{BN} + V_{CN}}{3} \tag{7.5}$$

Table 7.3 summarizes the generated CMV by different space vectors. Generated CMV of the sample switching sequence of the VSVPWM is depicted in Fig. 7.2(b). We can reduce the CMV to $V_{dc}/3$ if only 'OOO' is used as a zero vector. In the same manner, CMV can be reduced to $V_{dc}/6$ when small vectors type 2 are eliminated. CMV can be theoretically kept at zero by only using medium vectors and zero state ('OOO'). However, this strategy is not applied in practical applications since we lose the major benefits of the three level inverter.

Table 7.3: Generated CMV by different space vectors

	Vectors	CMV
zero vector	V_0(OOO)	0
zero vector	V_0((PPP),V_0(NNN)	$\pm V_{dc}/2$
small vectors1	V_{1P}(POO),V_{2N}(OON),V_{3P}(OPO) V_{4N}(NOO),V_{5P}(OOP),V_{6N}(ONO)	$\pm V_{dc}/6$
small vectors2	V_{1N}(OON),V_{2P}(PPO),V_{3N}(NON) V_{4P}(OPP),V_{5N}(NNO),V_{6P}(POP)	$\pm V_{dc}/3$
medium vectors	V_7(PON), V_8(OPN), V_9(NPO) V_{10}(NOP), V_{11}(ONP), V_{12}(PNO)	0
large vectors	V_{13}(PNN), V_{14}(PPN), V_{15}(NPN) V_{16}(NPP), V_{17}(NNP), V_{18}(PNP)	$\pm V_{dc}/6$

7.3 Derivation of the proposed HCBPWM

Compared to SVPWM, carrier based PWM is simpler to implement, especially for multi-level inverters where the calculations are more complex. Moreover, it has been shown that CBPWM can be equivalent to SVPWM []. A conventional CBPWM where two carrier waves are compared with the three-phase modulation waves is shown in Fig. 7.3. Modulation waves can be written as:

$$\begin{aligned} u_a &= m \cdot \cos(2\pi f_o t) \\ u_b &= m \cdot \cos(2\pi f_o t - 2\pi/3) \\ u_b &= m \cdot \cos(2\pi f_o t + 2\pi/3) \end{aligned} \tag{7.6}$$

Where m and f_o are the modulation index and the output frequency, respectively. When the zero sequence is added to the carrier waveforms, modulation index can be greater than 1. The main disadvantage of this modulation is large NPV deviations.

A double modulation CBPWM with the elimination of the NPV fluctuations is first developed in [200]. This strategy is practically equivalent to the conventional

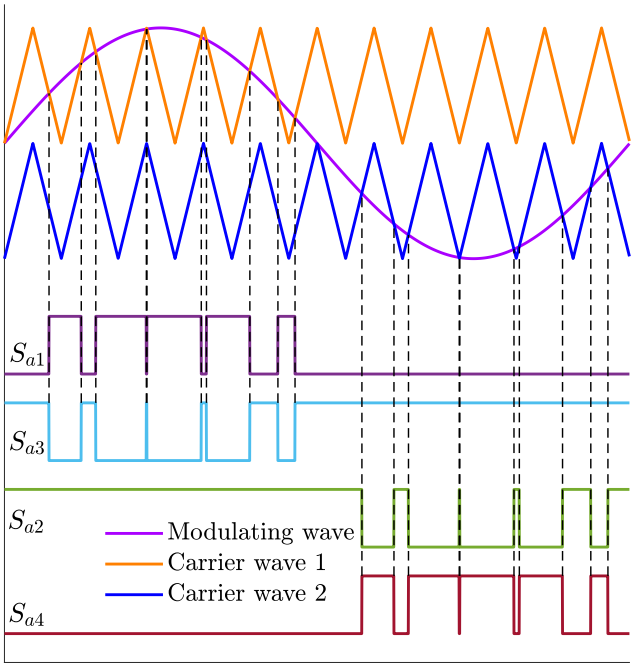

Figure 7.3: Conventional CBPWM with two carriers.

VSVPWM studied earlier. Two modulation waves, known as positive and negative modulations, are compared with the carrier for each phase. The positive modulation wave, u_{xp} $(x = a, b, c)$, is used to control the S_{x1} and S_{x3} and toggle the switching state of the phase leg between the 'O' and 'P' states. At the same time, the negative modulation wave, u_{xn} is used to control the S_{x2} and S_{x4} and toggle the switching state of the corresponding phase leg between the 'N' and 'O' states. The final switching state of the phase leg is obtained by combining the corresponding positive and negative switching states, as displayed in Fig. 7.4.

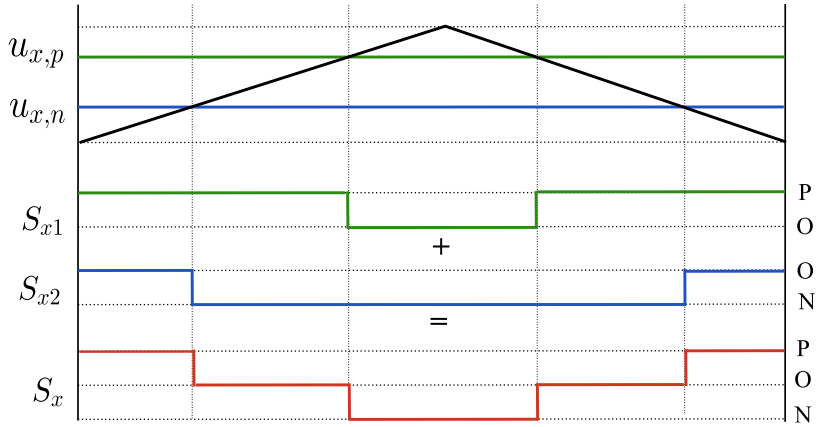

Figure 7.4: Construction of the phase leg state using positive and negative modulation waves.

7.3.1 Principle of the operation

The positive and negative modulation waves are obtained from the three phase modulation waves in (7.6). In order to derive the positive and negative modulation waves,

the main reference voltages are rearranged as follows:

$$\begin{aligned} u_{max} &= max(u_a, u_b, u_c), \\ u_{min} &= min(u_a, u_b, u_c), \\ u_{mid} &= mid(u_a, u_b, u_c). \end{aligned} \tag{7.7}$$

Where u_{max} is the maximum of the three modulation waves, u_{min} is the minimum, and u_{mid} is the median modulation wave. Based on the Volts-seconds product, the following can be written for the line voltages:

$$\begin{aligned} \sum_{k=-1,0,1} (kd_{max,k} - kd_{mid,k}) &= u_{max} - u_{mid} \\ \sum_{k=-1,0,1} (kd_{mid,k} - kd_{min,k}) &= u_{mid} - u_{min} \\ \sum_{k=-1,0,1} (kd_{max,k} - kd_{min,k}) &= u_{max} - u_{min} \end{aligned} \tag{7.8}$$

Where $k = -1, 0, 1$ is the switching states corresponding to 'N', 'O', 'P', respectively, and $d_{x,k}$ denote the duty ratio of state k of phase x. In other forms:

$$\begin{cases} (-d_{max,-1} + 0 \cdot d_{max,0} + d_{max,1}) - (-d_{mid,-1} + 0 \cdot d_{mid,0} \\ \qquad +d_{mid,1}) = u_{max} - u_{mid} \\ (-d_{mid,-1} + 0 \cdot d_{mid,0} + d_{mid,1}) - (-d_{min,-1} + 0 \cdot d_{min,0} \\ \qquad +d_{min,1}) = u_{mid} - u_{min} \\ (-d_{max,-1} + 0 \cdot d_{max,0} + d_{max,1}) - (-d_{min,-1} + 0 \cdot d_{min,0} \\ \qquad +d_{min,1}) = u_{max} - u_{min} \end{cases} \tag{7.9}$$

Since the last equation can be achieved by adding up the first two, we only have two

equations with six unknowns. So, more information is needed to solve the equations. Another restriction is the fact that the sum of the duty ratios of the three states for each phase is equal to one:

$$d_{x,-1} + d_{x,0} + d_{x,1} = 1, \quad x = min, mid, max \tag{7.10}$$

We also know that in order to achieve a zero average NP current, the zero state ratio of the all phases should be the same ($d_{max,0} = d_{mid,0} = d_{min,0}$).

Two more restrictive conditions are required to uniquely solve the equations. Considering the space diagram (see Fig. 7.1), in any Sectors, the maximum voltage (u_{max}) switches between states 'P' and 'O'. Similarly, the minimum voltage (u_{min}) switches only between 'O' and 'N', while the median voltage (u_{mid}) has all three states in every switching period. This can be seen for Sector I in Fig. 7.2. In other words:

$$d_{max,-1} = d_{min,1} = 0 \tag{7.11}$$

This limitation helps us to lower the switching power loss by reducing the total number of switching transients. It is worth mentioning that different restrictions can be applied to achieve other design objectives. The resultant duty ratios are obtained

as follows:

$$\begin{cases} d_{max,1} = \dfrac{u_{max} - u_{min}}{2}, d_{max,-1} = 0, \\ d_{max,0} = 1 - \dfrac{u_{max} - u_{min}}{2} \\ d_{mid,1} = \dfrac{u_{mid} - u_{min}}{2}, d_{mid,-1} = \dfrac{u_{max} - u_{mid}}{2}, \\ d_{mid,0} = 1 - \dfrac{u_{max} - u_{min}}{2} \\ d_{min,1} = 0, d_{min,-1} = \dfrac{u_{max} - u_{min}}{2}, \\ d_{min,0} = 1 - \dfrac{u_{max} - u_{min}}{2} \end{cases} \tag{7.12}$$

By comparing (7.12) and Fig. 7.4, the positive and negative modulation waves can be obtained:

$$\begin{aligned} u_{max,p} = \frac{u_{max} - u_{min}}{2}, & u_{max,n} = 1, \\ u_{mid,p} = \frac{u_{mid} - u_{min}}{2}, & u_{mid,n} = 1 - \frac{u_{max} - u_{mid}}{2}, \\ u_{min,p} = 0, & u_{min,n} = 1 - \frac{u_{max} - u_{min}}{2} \end{aligned} \tag{7.13}$$

So, in general, the modulation waves of each phase can be expressed as:

$$\begin{aligned} u_{x,p} &= \frac{u_x - u_{min}}{2} \\ u_{x,n} &= 1 - \frac{u_{max} - u_x}{2}. \end{aligned} \tag{7.14}$$

Positive and negative modulation waves for phase A, when $m = 0.8$ is shown in Fig. 7.5.

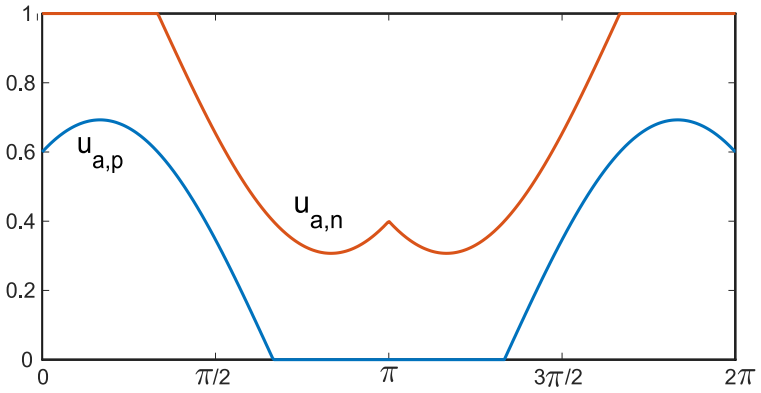

Figure 7.5: Positive and negative modulation waves of phase A, $m = 0.8$.

7.3.2 CMV reduction

The generated common voltage of the double modulation wave PWM is similar to the conventional VSVPWM shown in Fig. 7.2, as long as the switching sequences are similar. The CMV can be reduced by rearranging the switching sequences. However, the calculated duty ratios in (7.13) must be the same in order to eliminate the NPV deviations.

In Fig. 7.4, each switching state follows the {*high, low, high*} pattern. The resultant switching state would be *ponop* for u_{mid}, *pop* for u_{max}, and *ono* for the u_{min}. Another switching pattern is also possible when a carrier with opposite phase is implemented. As shown in Fig. 7.6, with the {*low, high, low*} pattern, the resultant switching sequence, $S_x^{'}$, is reversed in comparison with the previous case, S_x, while the duty ratio of each state remains the same.

In case that only one of the carriers are used, the generated CMV will have the same magnitude. In order to eliminate the vectors with higher CMV, both carriers should be used. With three phases and two carriers, six different combinations can be expected: two of the phases are compared to carrier1, and the remaining phase

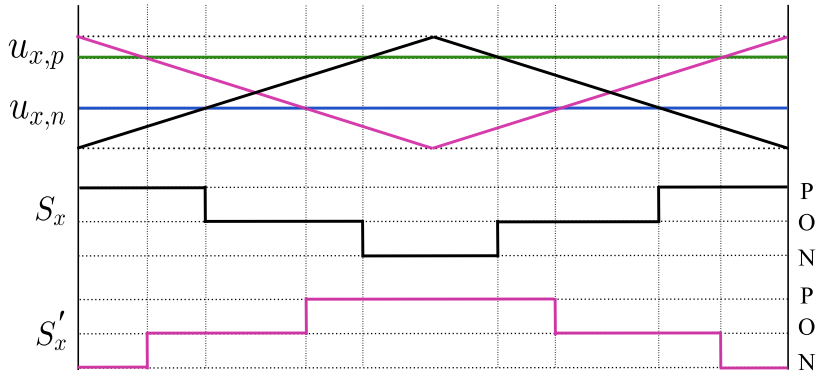

Figure 7.6: The reversed switching patterns using two carriers with opposite phases.

is compared with carrier2 (three combinations), or only one phase compared with carrier1, and the other two phases are compared with carrier2 (three combinations) that are all depicted in Fig. 7.7 along with the generated V_{CM}. Notice that all six cases can reduce the CMV to $\pm V_{dc}/6$.

Considering that all the combinations can ideally eliminate the NPV fluctuations and reduce the CMV, other aspects should be considered to compose the most efficient modulation scheme. In Fig. 7.7, it is notable that the average CMV in a switching cycle is higher when u_{mid} is reversed. Higher average CMV results in higher leakage current leading to more NPV deviations. Furthermore, there are nine switching segments, and only two devices are switching in the same phase. In other cases, when either u_{min} or u_{max} has the reversed switching, although there are only seven segments, four devices are switched in one of the transitions. Therefore, the switching losses are similar in different cases. Another factor is the harmonic content of the output voltage, which is studied next. It is worth mentioning that all three phases (a,b,c) should be reversed equally in a fundamental cycle in order to have balanced line-to-line voltages.

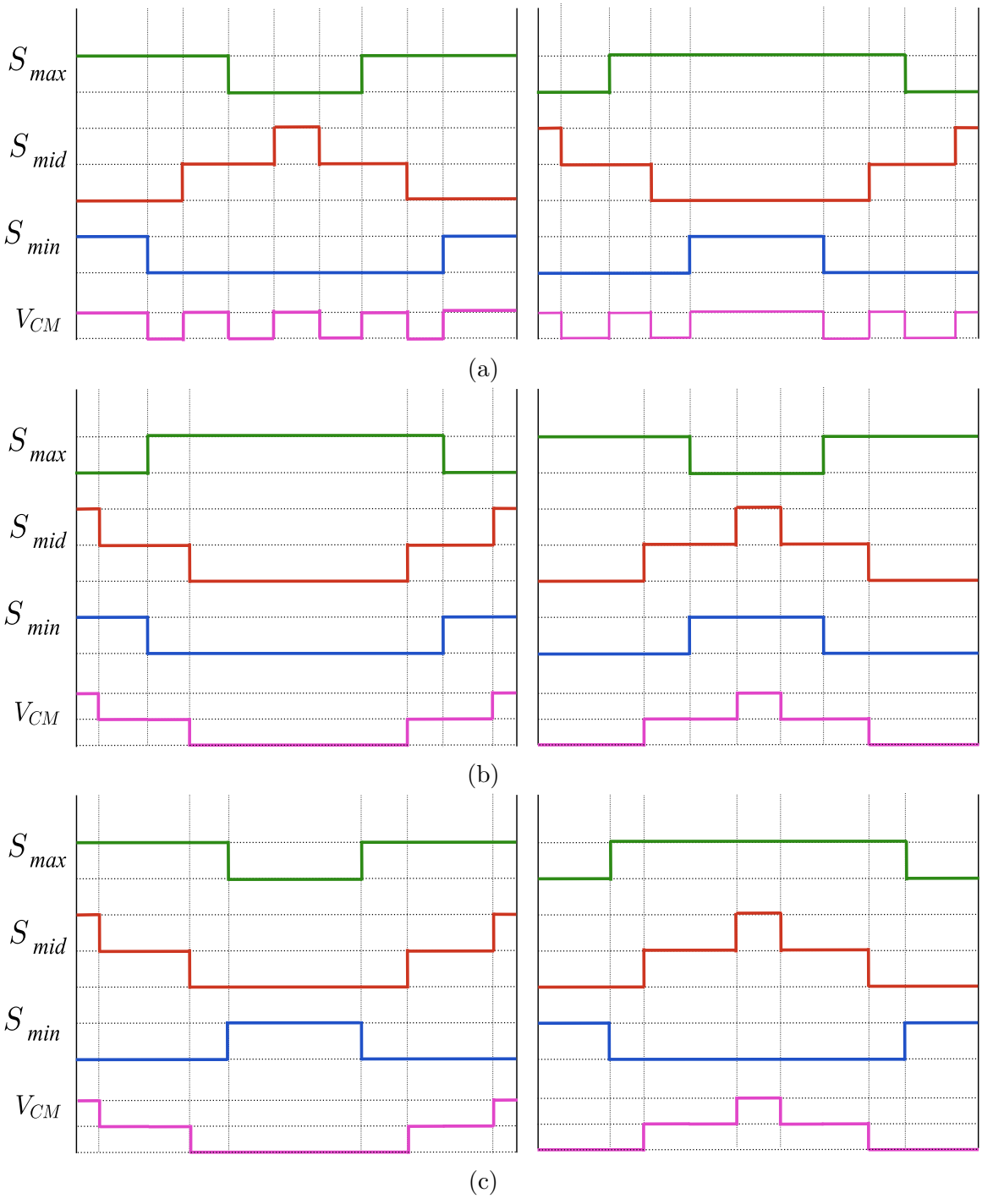

Figure 7.7: Different combination of switching sequences to reduce CMV when only a) u_{mid}, b) u_{max}, c) u_{min} has different switching pattern.

7.3.3 Harmonic content

The quality of the output line voltage is another important performance index. One of the most intuitive analytical approaches to evaluate the harmonic content is the harmonic flux trajectory (HFT) that uses the space vectors [201, 202]. The harmonic flux in a switching period for modulation index m is calculated as follows [203]:

$$\lambda(m,\theta) = \int_0^{T_s} (V_k - V_{ref})dt \tag{7.15}$$

Where V_{ref} is the reference voltage with the angle of θ, and V_k is the space vectors that are used to build the reference voltage. The RMS value of the flux in each switching cycle is a scale of the harmonic distortion and can be calculated as follows:

$$\lambda^2_{rms}(m,\theta) = \frac{1}{T_s}\int_0^{T_s} (\Re(V_k - V_{ref})^2 + \Im(V_k - V_{ref})^2)dt \tag{7.16}$$

HFT of the conventional CBPWM is shown in Fig. 7.8a in Sector I for different modulation index. In Fig. 7.8b, where the HFT of the RCMV-CBPWM with only reversed switching of $u_m in$, it can be seen that the HFT does not have a same pattern in all Sectors. Therefor, the root mean square of HFT in a fundamental cycle, as calculated in (7.17), is used as a more intuitive parameter.

$$\lambda^2_{rms}(m) = \frac{1}{2\pi}\int_0^{2\pi} \lambda^2_{rms}(m,\theta)d\theta \tag{7.17}$$

Two of the RCMV-CBPWM cases are compared with the conventional CBPWM for different modulation indices in Fig. 7.9. One case is where only one of the phases (phase a) is reversed switched all the time, and the other case is where u_{min} is reversed all the time, which means all three phases are reversed equally in a fundamental cycle.

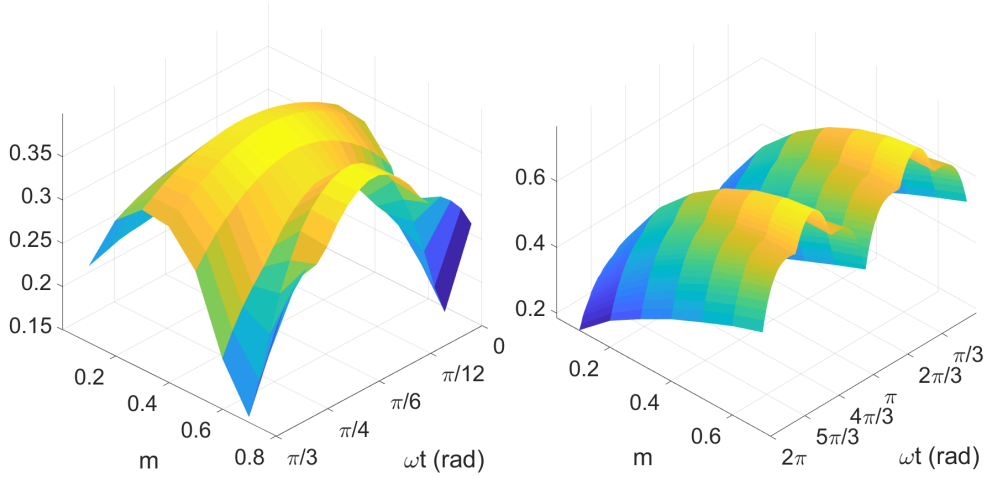

Figure 7.8: Harmonic flux trajectories of a) conventional CBPWM in Sector I, b) double modulation RCMV-CBPWM when u_{min} is reversed in all Sectors.

It can be seen that in both cases, the harmonic content is increased in comparison with the conventional CBPWM. Moreover, the second case where the three phases are equally reversed switched results in lower harmonic content.

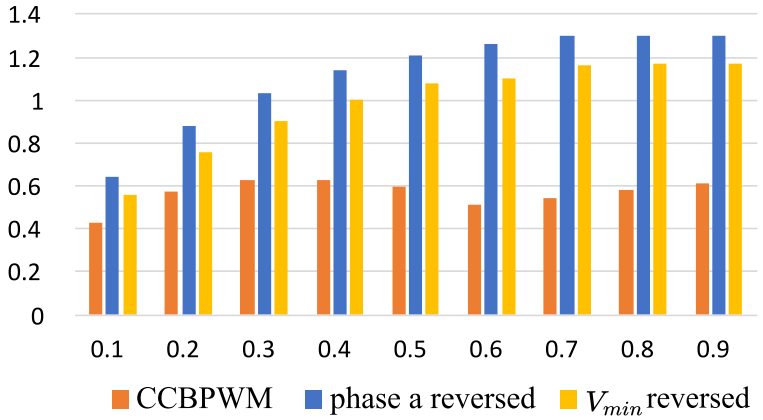

Figure 7.9: RMS value of the HFT in a fundamental cycle for three different modulation.

7.3.4 Neutral point voltage deviation

So far, we have learned that the best results are achieved when either u_{min} or u_{max} is reversed, shown in Fig. 7.7(b) and Fig. 7.7(c). More criteria are required to come up with the best combination of reversed switching. Therefore, the variations of neutral point current are taken into account. Although the average of NP current in a switching cycle is equal to zero in all cases, the lower the RMS value, the lower would be the NPV fluctuations within a switching cycle. The instantaneous neutral point current is expressed as [204]:

$$i_{NP} = -(|S_a|i_a + |S_b|i_b + |S_c|i_c) \tag{7.18}$$

Where S_x is the switching state of phase x. The RMS value of the neutral point current in each switching cycle is chosen as a performance criterion. For unity power factor, the neutral point current deviation in the first Sector is shown in Fig. 7.10 when either u_{max} or u_{min} is used for the reversed switching all the time. The asymmetric pattern of the NP current is notable in both figures. It is assumed that the maximum output current is equal to one.

In this chapter, a new hybrid modulation is applied by combining the two mentioned cases. In the first half of Sector I, u_{max} is used for the reversed switching, while u_{min} is used for the reverse switching in the second half. Therefore, the total neutral point current variation is minimized. The resultant NP current in the first Sector is depicted in Fig. 7.11. The SVD of the proposed hybrid modulation is shown in Fig. 7.12.

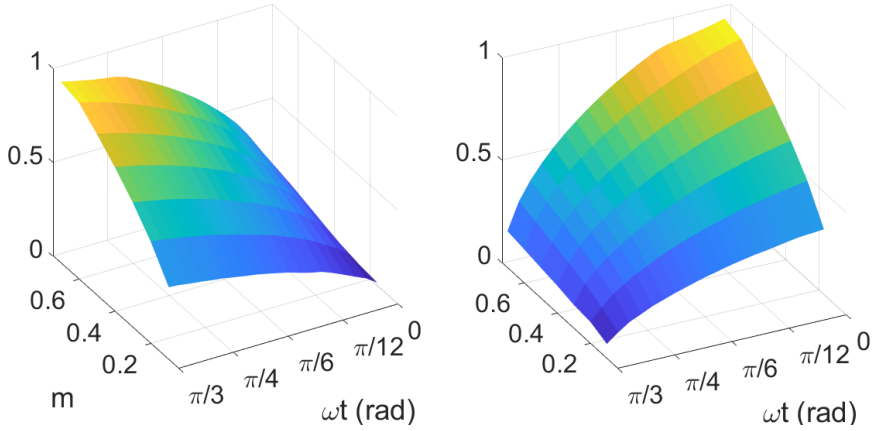

Figure 7.10: Neutral point current (rms) in the first Sector for unity power factor when a) u_{max} is reversed, b) u_{min} is reversed.

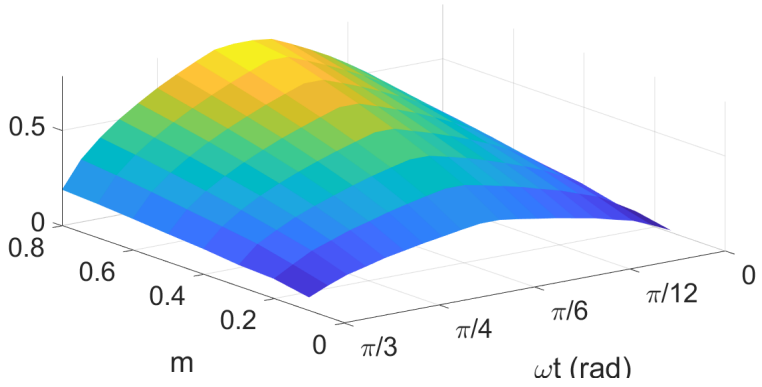

Figure 7.11: Neutral point current (rms) of the proposed hybrid modulation for unity power factor in the first Sector.

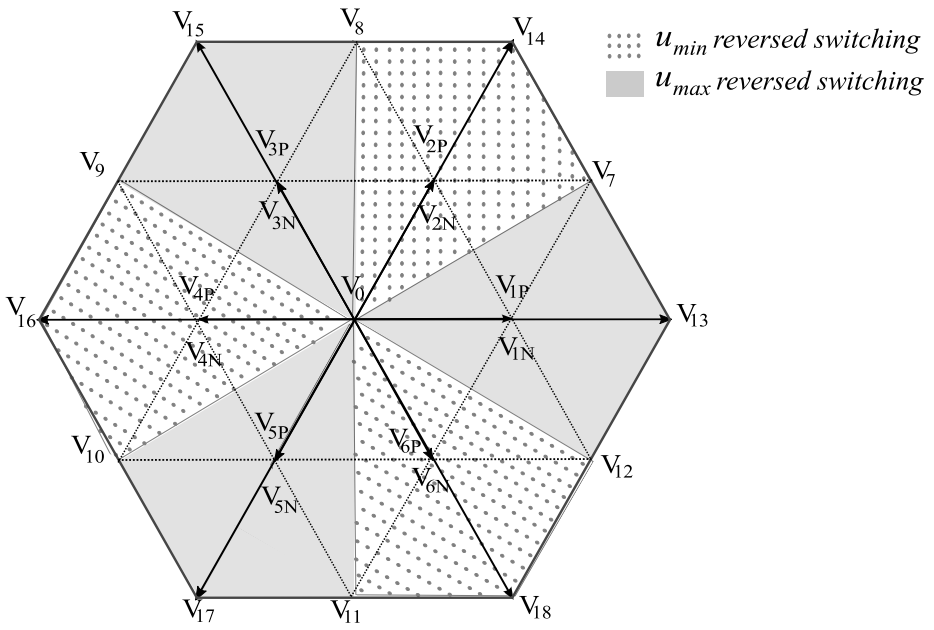

Figure 7.12: Space vector diagram of the proposed hybrid CBPWM with reduced CMV.

7.4 Active NPV controller

In the ideal conditions, the average neutral point is zero, and the voltages of the dc-link capacitors would be equal. However, in practice, V_{C1} and V_{C2} would drift from $U_{dc}/2$ due to the various disturbances. Some of the influencing factors are the leakage current flowing through the ground wire and unequal dc link capacitors. Therefore, an active controller is required to reduce the fluctuations of the neutral point voltage.

Since the NP current is influenced by level 0 of each phase, the NPV deviations can be controlled by adjusting the level 0 of one or more phases. Notice that the line to line voltage should not be affected. In this chapter, only the median phase, u_{mid} is used for level 0 adjustment. The reason is that the line voltage can be kept the same since u_{mid} contains all three levels, and there is no need to update the other phases.

In Fig. 7.13, the adjustment of the duty ratio of u_{mid} is depicted. Assuming level 0 should be changed by $\Delta d_{mid,0}$, the duty ratio of level 1 and level -1 should be updated as well since $\Delta d_{mid,0} = \Delta d_{mid,1} + \Delta d_{mid,-1}$. In order to keep the line to line voltage the same, the voltage changes of V_{mid} should be zero:

$$\Delta V_{mid} = \Delta d_{mid,1} V_{C1} - \Delta d_{mid,-1} V_{C2} = 0 \Rightarrow \frac{\Delta d_{mid,1}}{\Delta d_{mid,-1}} = \frac{V_{C2}}{V_{C1}} \tag{7.19}$$

Where V_{C1} and V_{C2} are the dc link capacitor voltages. Hence, duty ratio adjustment of different levels of u_{mid} can be calculated as follows:

$$\Delta d_{mid,1} = \frac{\Delta d_{mid,0}}{1 + K_{dc}}, \Delta d_{mid,-1} = \frac{K_{dc} \Delta d_{mid,0}}{1 + K_{dc}} \tag{7.20}$$

$K_{dc} = V_{C1}/V_{C2}$.

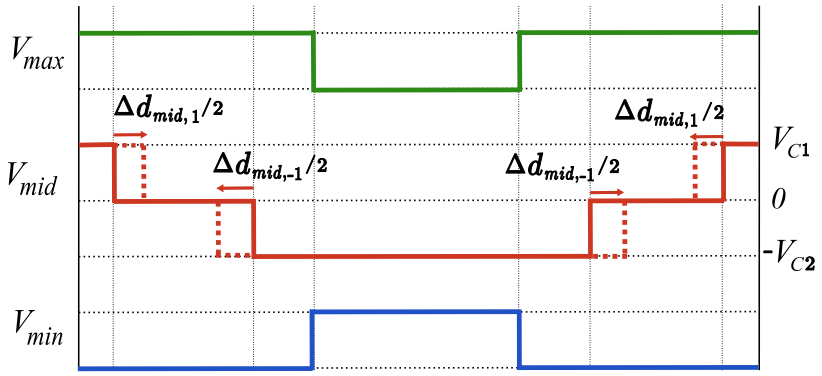

Figure 7.13: Adjusting the duty ratio of the median phase, u_{mid}, for NPV control.

Assuming that the voltage difference of the dc link capacitors are $\Delta V_{dc} = V_{C1} - V_{C2}$, the required compensating current for NPV adjustment is obtained by the following equation:

$$i_{cmp} = \frac{\Delta V_{dc}(C_1 + C_2)}{T_s} \tag{7.21}$$

Since only u_{mid} is used for level 0 adjustment, the compensated current after adjustment is equal to $i_{cmp} = \Delta d_{mid,0} \cdot i_{mid}$. Therefore,

$$\Delta d_{mid,0} = \frac{\Delta U_{dc}(C_1 + C_2)}{T_s i_{mid}} \tag{7.22}$$

So, the duty ratio adjustments can be obtained from (7.22) and (7.20). It should be mentioned that the duty ratio adjustment is limited to the initial values. For example, when $\Delta d_{mid,0} > 0$ (the case shown in Fig. 7.13), it is limited by $d_{mid,1}$ and $d_{mid,-1}$. This limitation can be mathematically expressed as:

$$0 < \Delta d_{mid,0} < min\{d_{mid,1}(1 + K_{dc}), \frac{d_{mid,-1}(1 + K_{dc})}{K_{dc}}\} \tag{7.23}$$

When $\Delta d_{mid,0} < 0$, it is limited by $d_{mid,0}$:

$$-d_{mid,0} < \Delta d_{mid,0} < 0 \tag{7.24}$$

From (7.22), one can conclude that the compensating capacity is a function of the adjusted phase current, the dc link capacitors, and the imbalance level of the capacitors. Furthermore, the compensating capability is not symmetric about zero according to (7.23) and (7.24). In Fig. 7.14, positive and negative compensating currents are shown under different modulation indices and for two different power factors.

It is noticeable that the positive and negative compensating currents are not symmetric in Sector I. Therefore, the average current is calculated in a fundamental cycle using (7.25) and depicted in Fig. 7.15 for various power factors and modulation indices. From Fig. 7.15, one can conclude that the compensating current magnitude

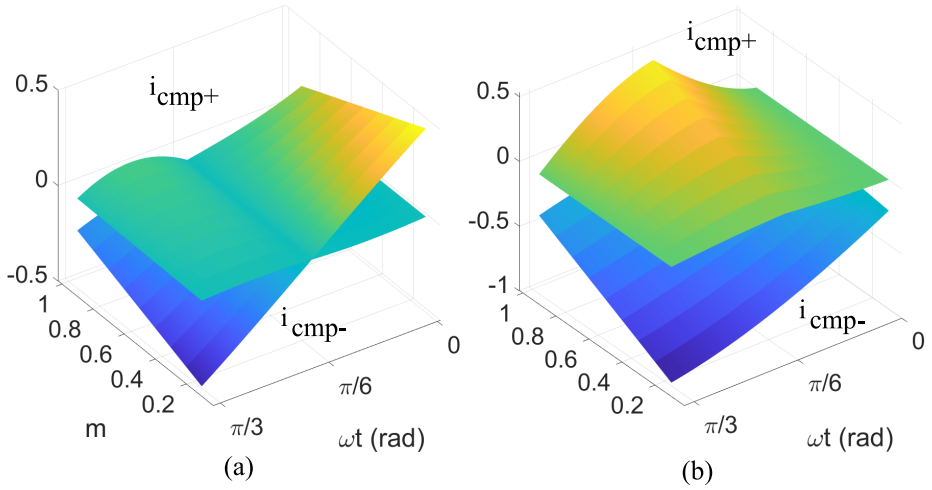

Figure 7.14: Positive and negative compensating currents in Sector I when a) $\phi = 0$, b) $\phi = \pi/4$.

is always higher than zero, meaning that the controller is capable of balancing the neutral point voltage in all operating conditions. However, the recovery speed is dependant on the power factor and modulation index. The controller can balance the NPV more quickly in low power factors and lower modulation indices.

$$i_{cmp\pm,avg} = \frac{1}{2\pi}\int_{0}^{2\pi} i_{cmp\pm}(\omega t)d\omega t \tag{7.25}$$

7.5 Experimental results

In this section, experimental results are presented to verify the performance of the proposed modulation. The experimental setup of the ANPC is shown in Fig. 7.16, and the experimental parameters are listed in Table 7.1. Three modulation schemes are implemented in TMS320f28379D micro-controller. The first one is the conventional

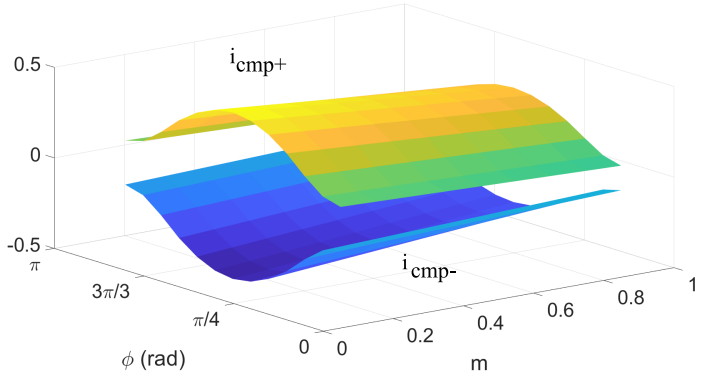

Figure 7.15: Average positive and negative compensating currents under different power factors and modulation indices.

Table 7.4: Experimental parameters

symbol	description	value
V_{dc}	input DC voltage	200 V
f_{sw}	switching frequency	50 kHz
f_o	fundamental frequency	833 Hz
C_1, C_2	dc-link capacitors	72 μF
m	modulation index	0.75
L	load inductance	200 μH
R	load resistance	1Ω

carrier-based. The second modulation is the double modulation wave CBPWM with CMV reduction proposed in [199]. Then, the proposed hybrid CBPWM with reduced CMV and the elimination of the NPV fluctuations is applied to the inverter.

Measured line-to-line voltage along with its harmonic content, dc-link capacitor voltages, and the generated common-mode voltages for all three modulations are shown in Fig. 7.17. The experimental results are repeated for two cases. In case I, series RL load is used, $\Phi = 0.7$, whereas case II indicates the results for only inductance load, $\Phi = 0$.

In comparison with the modulation proposed in [199], the proposed modulation can effectively reduce the harmonic distortion of the line voltage as well as the NPV

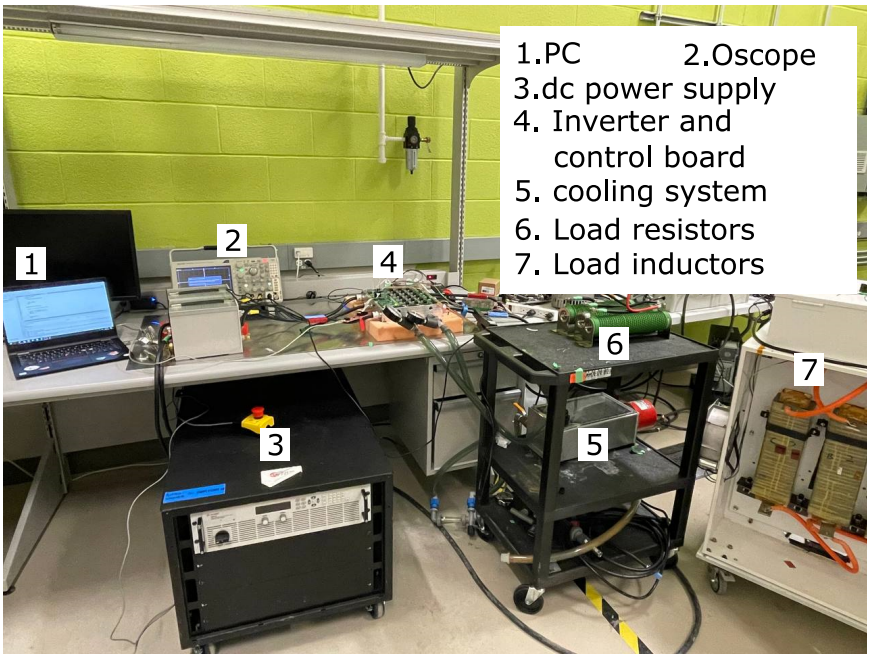

Figure 7.16: The experimental setup of the 3-L ANPC.

oscillation. The advantages of the proposed modulation as opposed to the second modulation is more noticeable in case II. Dc-link capacitor voltages possess different dc averages when the second modulation is applied demanding the voltage balance control. However, the proposed modulation ensures the same average values for the dc-link capacitors. The first modulation provides the lowest THD at the expense of high common mode voltage and NPV oscillations. The performance of the active NP controller is shown in Fig. 7.18. A voltage perturbation is enforced to assess the NPV controller. The initial voltage error is $14V$ and the controller recovers the voltage balance within 7 fundamental cycles.

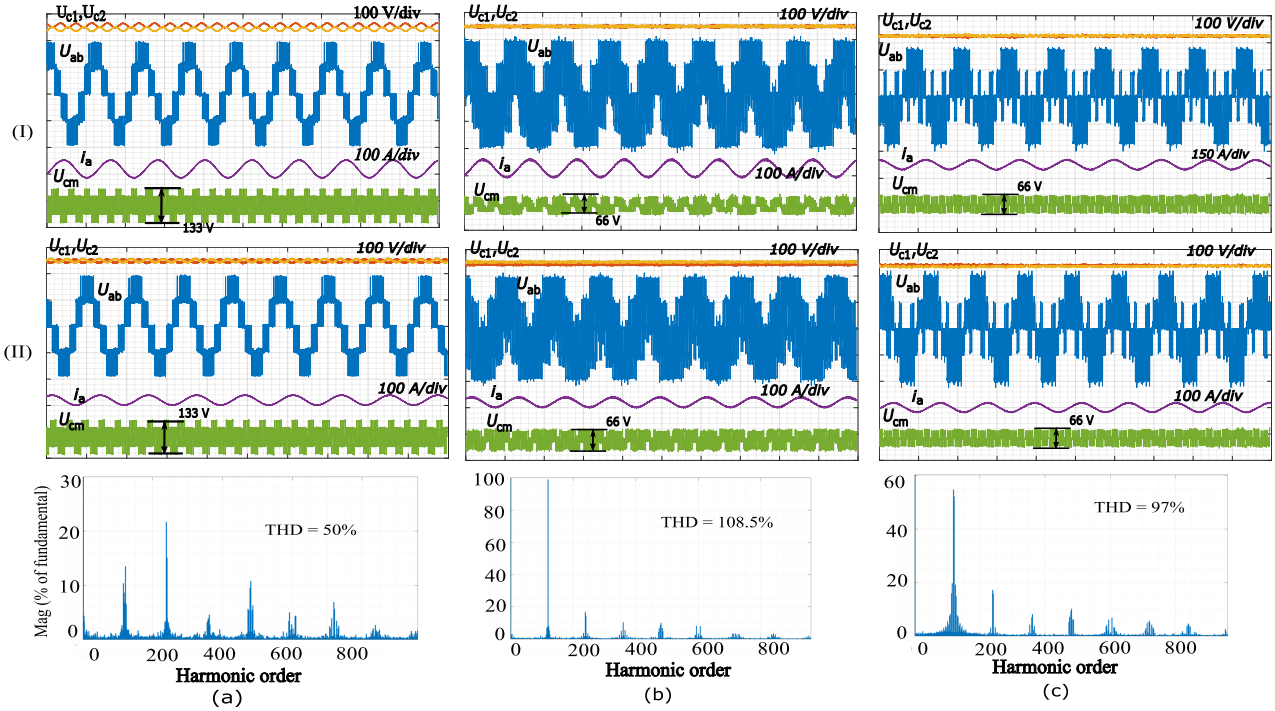

Figure 7.17: Measured line-to-line voltages, dc-link capacitor voltages, output current i_a, U_{cm}, and harmonic content of U_{ab}; a) conventional CBPWM, b) RCMV-CBPWM when only phase a is reversed, c) proposed CBPWM with CMV reductions.

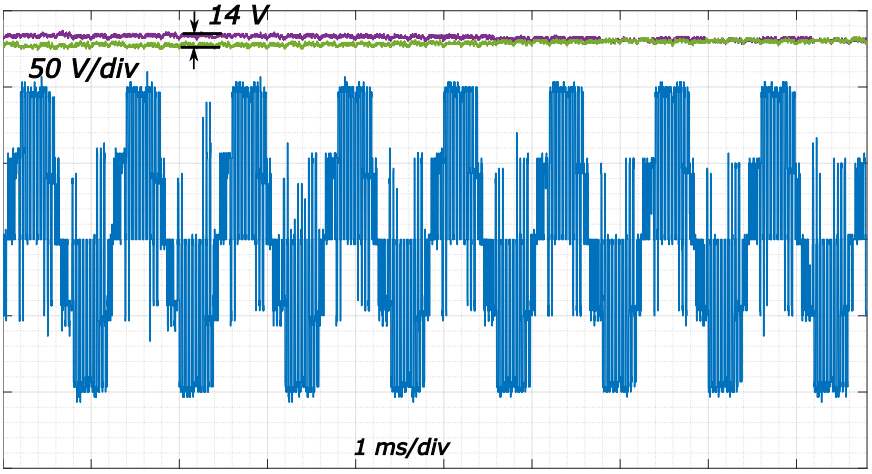

Figure 7.18: Experimental waveforms for voltage balancing control.

7.6 Summary

In order to reduce the common mode voltage and to eliminate the neutral point oscillations in a three level active NPC inverter, a hybrid carrier-based PWM is proposed in this chapter. This modulation is derived based on the theoretical analysis of the common mode voltage and the neutral point current ripples. Simulation results confirms that the proposed modulation minimizes the variations of the neutral point current in comparison with the conventional CBPWM modulation. In addition to easy implementation, common mode voltage is reduced by half. An active NP controller is also developed and tested to address the NPV perturbations. The performance the proposed modulation is evaluated experimentally and compared to the conventional CBPWM and the available RCMV-CBPWM modulations.

Chapter 8

Conclusions and Future Work

8.1 Conclusions

In this thesis, electromagnetic interference of power inverters is studied. Electromagnetic interference is one of the major issues of modern power electronic devices that need to be addressed at the early stages of design. Therefore, a comprehensive model is required to examine the drawbacks of EMI emissions. In this thesis, only conducted emissions are investigated.

In the beginning, a comprehensive review of the available modeling strategies is presented. Moreover, EMC measurement devices and testing procedures are reviewed for power converter applications. The topics discussed here help the reader obtain an overview of the EMC testing and develop a comprehensive understanding of the EMC measurement device. The next step is to create a model based on the project's technical requirements.

Assuming conducted emissions and EMI issues should be considered in the design stage, detailed system modeling is necessary. Therefore, the modeling process is

studied in detail for a three-phase motor drive system. Conducted emissions in a three-phase inverter-fed motor drive are studied. A physics-based model is derived for each part of the system using a device characterization tool, a finite element analysis tool, and impedance curve fitting tools. An improved universal equivalent circuit is proposed to model the induction motor in the entire frequency range. A balanced approach regarding the accuracy and simplicity of the model is considered through the model extraction. Furthermore, common mode and differential mode emissions are studied, and two equivalent circuits are extracted.

Equivalent circuits are a more robust analysis tool during the design process. Hence, equivalent circuit modeling is extensively studied in a three-level neutral point clamped inverter. Compared with the conventional differential mode (DM) EMI modeling of power inverters that use only one current source, it is shown that two current sources are required for more precise modeling. A new unified model is proposed for an active neutral point clamped inverter based on the existing equivalent circuit models for common-mode (CM) EMI and the developed DM model. The proposed model predicted both CM and DM EMI emissions and compared them with the time-domain results. Simulation results indicate that the modeling precision is improved by 56%.

In order to mitigate the EMI issues, various approaches are recommended in the literature. Software-based methods that generally suppress the emissions at the source are more cost-effective than hardware-based solutions such as EMI filters. In the last two chapters, two means of EMI noise suppression are explored. In one approach, spread-spectrum modulation techniques are studied and implemented. These methods spread the power spectrum in the frequency range, thus reducing the harmonic

spikes. Different spread-spectrum modulations are investigated for an active neutral point clamped (ANPC) inverter. The effect of EMI receiver and intermediate filter bandwidth is considered in the modeling. The validity of simulation results and calculations is confirmed by experimental results.

In another software-based EMI suppression method, a new hybrid CBPWM strategy is proposed that not only eliminates the neutral point voltage oscillations but also reduces the common-mode voltage (CMV) by half. Furthermore, the harmonic content of the output voltage is reduced by adjusting the modulation waves based on the location of the reference vector in the space vector diagram. An active neutral point voltage controller is also presented and applied in order to maintain the performance of the modulation strategy under the NPV perturbations. The performance of the proposed algorithm is compared to the conventional CBPWM and available RCMV-CBPWM in the literature. The performance the proposed modulation is evaluated experimentally and compared to the conventional CBPWM and the available RCMV-CBPWM modulations.

8.2 Future work

According to the work included in this thesis, the following suggestions could be considered in the future.

In Chapter 3, the detailed modeling of a three-phase motor drive system is studied. An improved universal equivalent circuit is proposed for the induction motor. Also, an improved equivalent circuit for DM and CM modeling is investigated. However, experimental validation is still lacking. High-frequency impedance measurement is needed to evaluate the accuracy of the improved model of the induction motor. The

conducted emissions should be measured based on the EMC standard guidelines. In Chapter 6, a similar approach is taken for the measurements.

The analytical modeling of the ANPC, developed is studied in Chapter 5. In the next step, the derived model can be used for EMI filter design, or to reduced the emissions by noise canceling methods.

Although various spread spectrum modulations are applied to the ANPC in Chapter 6, the impacts of the switching frequency need to be investigated more carefully. Switching frequency inversely affects the harmonic content of the output voltage and current. By increasing the switching frequency, output current ripples decrease and the dc-link voltage ripples. However, an increase in the switching frequency will result in higher conducted emissions along with higher switching loss. By closer investigation of the current ripples and NPV variations, it can be concluded that ripples are not uniformly distributed in a fundamental cycle. Several studies exercise a variable switching frequency approach by taking advantage of this fact. In the future, the effects of switching frequency on the neutral point current and the conducted emissions can be considered to improve the available variable switching frequency modulations. Furthermore, a similar analysis can be applied to the improved CBPWM proposed in Chapter 7.

References

[1] emc standards. (2020) Real-life short stories about electromagnetic interference (emi). [Online]. Available: https://www.emcstandards.co.uk/emi-stories

[2] the New York Times. (2013) Toyota recalling 1 million vehicles for airbag and wiper problems. [Online]. Available: https://wheels.blogs.nytimes.com/2013/01/30/toyota-recalling-1-million-vehicles-for-air-bag-and-wiper-problems/?ref=automobiles

[3] H. Ott, *Electromagnetic Compatibility Engineering.* Hoboken, NJ: Wiley, 2011.

[4] D. Morgan, *A Handbook for EMC Testing and Measurement.* Herts, U.K.: Institution of Engineering and Technology, 2007.

[5] U.S Federal Communication Commission, "Code of Federal Regulations, title 47, Part 15: Radiofrequency Devices, SubPart B: Unintentional Radiators," standard 67 FR 45670, July 2002.

[6] IEC, "Electromagnetic compatibility of multimedia equipment emission requirements, Edition 2.0," standard CISPR32, Oct. 2019.

[7] Department of Defense Interface Standard, "Requirements for the control of electromagnetic interference characteristics of subsystems and equipment," standard MIL-STD-461G, Dec. 2015.

[8] C. Paul, *Introduction to Electromagnetic Compatibility*, ser. Wiley Series in Microwave and Optical Engineering. Hoboken, NJ: Wiley, 2006.

[9] L. B. Gravelle and P. F. Wilson, "Emi/emc in printed circuit boards-a literature review," *IEEE Transactions on Electromagnetic Compatibility*, vol. 34, no. 2, pp. 109–116, May 1992.

[10] E. Li, X. Wei, A. C. Cangellaris, E. Liu, Y. Zhang, M. D'Amore, J. Kim, and T. Sudo, "Progress review of electromagnetic compatibility analysis technologies for packages, printed circuit boards, and novel interconnects," *IEEE Transactions on Electromagnetic Compatibility*, vol. 52, no. 2, pp. 248–265, May 2010.

[11] J. Fan, X. Ye, J. Kim, B. Archambeault, and A. Orlandi, "Signal integrity design for high-speed digital circuits: Progress and directions," *IEEE Transactions on Electromagnetic Compatibility*, vol. 52, no. 2, pp. 392–400, Apr. 2010.

[12] T. Wu, F. Buesink, and F. Canavero, "Overview of signal integrity and emc design technologies on pcb: Fundamentals and latest progress," *IEEE Transactions on Electromagnetic Compatibility*, vol. 55, no. 4, pp. 624–638, Ma. 2013.

[13] Q. Liu, W. Shen, F. Wang, D. Boroyevich, V. Stefanovic, and M. Arpilliere, "Experimental evaluation of igbts for characterizing and modeling conducted

emi emission in pwm inverters," in *Proc. IEEE Conference on Power Electronics Specialist (PESC)*, Acapulco, Mexico, June 2003, pp. 1951–1956.

[14] Q. Liu, F. Wang, and D. Boroyevich, "Frequency-domain emi noise emission characterization of switching power modules in converter systems," in *Proc. IEEE Applied Power Electronics Conference and Exposition (APEC)*, Austin, TX, June 2005, pp. 787–792.

[15] ——, "Conducted-emi prediction for ac converter systems using an equivalent modular–terminal–behavioral (mtb) source model," *IEEE Transactions on Industry Applications*, vol. 43, no. 5, pp. 1360–1370, Sep. 2007.

[16] A. Ales, J. Schanen, J. Roudet, and D. Moussaoui, "A new analytical emc model of power electronics converters based on quadripole system: Application to demonstrate the mode decoupling condition," in *Proc. IEEE Applied Power Electronics Conference and Exposition (APEC)*, Charlotte, NC, Mar. 2015, pp. 2684–2690.

[17] A. Ales, J. Schanen, D. Moussaoui, and J. Roudet, "Impedances identification of dc/dc converters for network emc analysis," *IEEE Transactions on Power Electronics*, vol. 29, no. 12, pp. 6445–6457, Dec. 2014.

[18] Q. Liu, F. Wang, and D. Boroyevich, "Modular-terminal-behavioral (mtb) model for characterizing switching module conducted emi generation in converter systems," *IEEE Transactions on Power Electronics*, vol. 21, no. 6, pp. 1804–1814, Nov. 2006.

[19] A. C. Baisden, D. Boroyevich, and F. Wang, "Generalized terminal modeling of electromagnetic interference," *IEEE Transactions on Industry Applications*, vol. 46, no. 5, pp. 2068–2079, Sep. 2010.

[20] H. Bishnoi, A. C. Baisden, P. Mattavelli, and D. Boroyevich, "Analysis of emi terminal modeling of switched power converters," *IEEE Transactions on Power Electronics*, vol. 27, no. 9, pp. 3924–3933, Sep. 2012.

[21] B. Kerrouche, M. Bensetti, and A. Zaoui, "New emi model with the same input impedances as converter," *IEEE Transactions on Electromagnetic Compatibility*, vol. 61, no. 4, pp. 1072–1081, Aug. 2019.

[22] J. Meng, W. Ma, Q. Pan, Z. Zhao, and L. Zhang, "Noise source lumped circuit modeling and identification for power converters," *IEEE Transactions on Industrial Electronics*, vol. 53, no. 6, pp. 1853–1861, Dec. 2006.

[23] H. Bishnoi, P. Mattavelli, and D. Boroyevich, "Un-terminated common-mode emi model of dc-fed motor drives," in *Proc. International Power Electronics and Motion Control Conference (EPE/PEMC)*, Novi Sad, Serbia, Sep. 2012, pp. DS2a.15–1–DS2a.15–8.

[24] H. Bishnoi, P. Mattavelli, R. Burgos, and D. Boroyevich, "Emi behavioral models of dc-fed three-phase motor drive systems," *IEEE Transactions on Power Electronics*, vol. 29, no. 9, pp. 4633–4645, Sep. 2014.

[25] B. Sun, R. Burgos, and D. Boroyevich, "Common-mode emi unterminated behavioral model of wide-bandgap-based power converters operating at high

switching frequency," *IEEE Journal of Emerging and Selected Topics in Power Electronics*, vol. 7, no. 4, pp. 2561–2570, Dec. 2019.

[26] T. J. Donnelly, S. D. Pekarek, D. R. Fudge, and N. Zarate, "Thévenin equivalent circuits for modeling common-mode behavior in power electronic systems," *IEEE Open Access Journal of Power and Energy*, vol. 7, pp. 163–172, 2020.

[27] H. Bishnoi, P. Mattavelli, R. Burgos, and D. Boroyevich, "Emi terminal modelling of dc-fed motor drives," in *Proc. European Conference on Power Electronics and Applications (EPE)*, Lille, France, Sep. 2013, pp. 1–10.

[28] H. Bishnoi, P. Mattavelli, R. P. Burgos, and D. Boroyevich, "Emi filter design of dc-fed motor-drives using behavioral emi models," in *Proc. European Conference on Power Electronics and Applications (EPE'15 ECCE-Europe)*, Geneva, Switzerland, Sep. 2015, pp. 1–10.

[29] M. Jin and M. Weiming, "A new technique for modeling and analysis of mixed-mode conducted emi noise," *IEEE Transactions on Power Electronics*, vol. 19, no. 6, pp. 1679–1687, 2004.

[30] W. Zhou, X. Pei, Y. Xiang, and Y. Kang, "A new emi modeling method for mixed-mode noise analysis in three-phase inverter system," *IEEE Access*, vol. 8, pp. 71 535–71 547, Mar. 2020.

[31] R. Zhu, N. Lin, V. Dinavahi, and G. Liang, "An accurate and fast method for conducted emi modeling and simulation of mmc-based hvdc converter station," *IEEE Transactions on Power Electronics*, vol. 35, no. 5, pp. 4689–4702, May 2020.

[32] G. Dadanema, M. Delhommais, F. Costa, J. L. Schanen, Y. Avenas, and C. Vollaire, "Analytical model for sic based power converter optimization including emc and thermal constraints," in *Proc. International Symposium on Electromagnetic Compatibility (EMC EUROPE)*, Angers, France, Sep. 2017, pp. 1–6.

[33] Y. Xiang, X. Pei, W. Zhou, Y. Kang, and H. Wang, "A fast and precise method for modeling emi source in two-level three-phase converter," *IEEE Transactions on Power Electronics*, vol. 34, no. 11, pp. 10 650–10 664, Nov. 2019.

[34] Y. Xie, C. Chen, Z. Huang, T. Liu, Y. Kang, and F. Luo, "High frequency conducted emi investigation on packaging and modulation for a sic-based high frequency converter," *IEEE Journal of Emerging and Selected Topics in Power Electronics*, vol. 7, no. 3, pp. 1789–1804, Sep. 2019.

[35] Y. Liu, K. Y. See, S. Yin, R. Simanjorang, A. K. Gupta, and J. Lai, "Equivalent circuit model of high power density sic converter for common-mode conducted emission prediction and analysis," *IEEE Electromagnetic Compatibility Magazine*, vol. 8, no. 1, pp. 67–74, 2019.

[36] X. Gong and J. A. Ferreira, "Investigation of conducted emi in sic jfet inverters using separated heat sinks," *IEEE Transactions on Industrial Electronics*, vol. 61, no. 1, pp. 115–125, Jan. 2014.

[37] A. Nejadpak and O. A. Mohammed, "Physics-based modeling of power converters from finite element electromagnetic field computations," *IEEE Transactions on Magnetics*, vol. 49, no. 1, pp. 567–576, Jan. 2013.

[38] I. F. Kovačević, T. Friedli, A. M. Muesing, and J. W. Kolar, "3-d electromagnetic modeling of emi input filters," *IEEE Transactions on Industrial Electronics*, vol. 61, no. 1, pp. 231–242, Jan. 2014.

[39] B. Revol, J. Roudet, J. Schanen, and P. Loizelet, "Emi study of three-phase inverter-fed motor drives," *IEEE Transactions on Industry Applications*, vol. 47, no. 1, pp. 223–231, Jan. 2011.

[40] J. Espina, J. Balcells, A. Arias, and C. Ortega, "Common mode emi model for a direct matrix converter," *IEEE Transactions on Industrial Electronics*, vol. 58, no. 11, pp. 5049–5056, Nov. 2011.

[41] J. Kotny and N. Idir, "Time domain models of the emi sources in the variable speed drives," in *Proc. IEEE Energy Conversion Congress and Exposition*, Atlanta, GA, Nov. 2010, pp. 1355–1360.

[42] A. D. Brovont, "Generalized differential-common-mode decomposition for modeling conducted emissions in asymmetric power electronic systems," *IEEE Transactions on Power Electronics*, vol. 33, no. 8, pp. 6461–6466, Aug. 2018.

[43] A. N. Lemmon, A. D. Brovont, C. D. New, B. W. Nelson, and B. T. DeBoi, "Modeling and validation of common-mode emissions in wide bandgap-based converter structures," *IEEE Transactions on Power Electronics*, vol. 35, no. 8, pp. 8034–8049, Aug. 2020.

[44] A. D. Brovont, A. N. Lemmon, C. New, B. W. Nelson, and B. T. DeBoi, "Analysis and cancellation of leakage current through power module baseplate

capacitance," *IEEE Transactions on Power Electronics*, vol. 35, no. 5, pp. 4678–4688, May 2020.

[45] P. R. Mugur, J. Roudet, and J. C. Crebier, "Power electronic converter emc analysis through state variable approach techniques," *IEEE Transactions on Electromagnetic Compatibility*, vol. 43, no. 2, pp. 229–238, May 2001.

[46] F. Costa, C. Vollaire, and R. Meuret, "Modeling of conducted common mode perturbations in variable-speed drive systems," *IEEE Transactions on Electromagnetic Compatibility*, vol. 47, no. 4, pp. 1012–1021, Nov. 2005.

[47] C. Jettanasen, F. Costa, and C. Vollaire, "Common-mode emissions measurements and simulation in variable-speed drive systems," *IEEE Transactions on Power Electronics*, vol. 24, no. 11, pp. 2456–2464, 2009.

[48] H. Zhu, J. Lai, A. R. Hefner, Y. Tang, and C. Chen, "Analysis of conducted emi emissions from pwm inverter based on empirical models and comparative experiments," in *Proc. IEEE Power Electronics Specialists Conference*, Charleston, SC, July 1999, pp. 861–867.

[49] G. Grandi, D. Casadei, and U. Reggiani, "Common- and differential-mode hf current components in ac motors supplied by voltage source inverters," *IEEE Transactions on Power Electronics*, vol. 19, no. 1, pp. 16–24, Jan. 2004.

[50] L. Xing, F. Feng, and J. Sun, "Behavioral modeling methods for motor drive system emi design optimization," in *Proc. IEEE Energy Conversion Congress and Exposition*, Atlanta, GA, Sep. 2010, pp. 947–954.

[51] Y. Duan, F. Iannuzzo, and F. Blaabjerg, "A new lumped-charge modeling method for power semiconductor devices," *IEEE Transactions on Power Electronics*, vol. 35, no. 4, pp. 3989–3996, April 2020.

[52] Y. Duan, F. Xiao, Y. Luo, and F. Iannuzzo, "A lumped-charge approach based physical spice-model for high power soft-punch through igbt," *IEEE Journal of Emerging and Selected Topics in Power Electronics*, vol. 7, no. 1, pp. 62–70, March 2019.

[53] S. Perez, R. M. Kotecha, A. U. Rashid, M. M. Hossain, T. Vrotsos, A. M. Francis, H. A. Mantooth, E. Santi, and J. L. Hudgins, "A datasheet driven unified si/sic compact igbt model for n-channel and p-channel devices," *IEEE Transactions on Power Electronics*, vol. 34, no. 9, pp. 8329–8341, Sep. 2019.

[54] H. Cao, P. Ning, X. Wen, T. Yuan, and H. Li, "An electrothermal model for igbt based on finite differential method," *IEEE Journal of Emerging and Selected Topics in Power Electronics*, vol. 8, no. 1, pp. 673–684, March 2020.

[55] L. Jing, M. Du, K. Wei, and W. G. Hurley, "An improved behavior model for igbt modules driven by datasheet and measurement," *IEEE Transactions on Electron Devices*, vol. 67, no. 1, pp. 230–236, Jan. 2020.

[56] Y. Mukunoki, K. Konno, T. Matsuo, T. Horiguchi, A. Nishizawa, M. Kuzumoto, M. Hagiwara, and H. Akagi, "An improved compact model for a silicon-carbide mosfet and its application to accurate circuit simulation," *IEEE Transactions on Power Electronics*, vol. 33, no. 11, pp. 9834–9842, Nov 2018.

[57] Z. Duan, T. Fan, X. Wen, and D. Zhang, "Improved sic power mosfet model considering nonlinear junction capacitances," *IEEE Transactions on Power Electronics*, vol. 33, no. 3, pp. 2509–2517, March 2018.

[58] V. Talesara, D. Xing, X. Fang, L. Fu, Y. Shao, J. Wang, and W. Lu, "Dynamic switching of sic power mosfets based on analytical subcircuit model," *IEEE Transactions on Power Electronics*, vol. 35, no. 9, pp. 9680–9689, Sep. 2020.

[59] T. Liu, T. T. Y. Wong, and Z. J. Shen, "A new characterization technique for extracting parasitic inductances of sic power mosfets in discrete and module packages based on two-port s-parameters measurement," *IEEE Transactions on Power Electronics*, vol. 33, no. 11, pp. 9819–9833, Nov. 2018.

[60] L. Pace, N. Defrance, A. Videt, N. Idir, J. C. De Jaeger, and V. Avramovic, "Extraction of packaged gan power transistors parasitics using s-parameters," *IEEE Transactions on Electron Devices*, vol. 66, no. 6, pp. 2583–2588, June 2019.

[61] J. Meng, W. Ma, Q. Pan, L. Zhang, and Z. Zhao, "Multiple slope switching waveform approximation to improve conducted emi spectral analysis of power converters," *IEEE Transactions on Electromagnetic Compatibility*, vol. 48, no. 4, pp. 742–751, Nov. 2006.

[62] X. Yang, X. Zhang, and P. R. Palmer, "Igbt converters conducted emi analysis by controlled multiple-slope switching waveform approximation," in *IEEE International Symposium on Industrial Electronics*, Taipei, Taiwan, May 2013, pp. 1–6.

[63] T. Qi, J. Graham, and J. Sun, "Characterization of igbt modules for system emi simulation," in *Proc. IEEE Applied Power Electronics Conference and Exposition (APEC)*, Palm Springs, CA, Feb. 2010, pp. 2220–2225.

[64] M. Moreau, N. Idir, P. Le Moigne, and J. J. Franchaud, "Utilization of a behavioural model of motor drive systems to predict the conducted emissions," in *Proc. IEEE Power Electronics Specialists Conference*, Rhodes, Greece, Aug. 2008, pp. 4387–4391.

[65] L. Ran, S. Gokani, J. Clare, K. J. Bradley, and C. Christopoulos, "Conducted electromagnetic emissions in induction motor drive systems. ii. frequency domain models," *IEEE Transactions on Power Electronics*, vol. 13, no. 4, pp. 768–776, July 1998.

[66] A. D. Callegaro, J. Guo, M. Eull, B. Danen, J. Gibson, M. Preindl, B. Bilgin, and A. Emadi, "Bus bar design for high-power inverters," *IEEE Transactions on Power Electronics*, vol. 33, no. 3, pp. 2354–2367, March 2018.

[67] M. Khan, P. Magne, B. Bilgin, S. Wirasingha, and A. Emadi, "Laminated busbar design criteria in power converters for electrified powertrain applications," in *Proc. IEEE Transportation Electrification Conference and Expo (ITEC)*, Dearborn, MI, June 2014, pp. 1–6.

[68] B. Mirafzal, G. L. Skibinski, R. M. Tallam, D. W. Schlegel, and R. A. Lukaszewski, "Universal induction motor model with low-to-high frequency-response characteristics," *IEEE Transactions on Industry Applications*, vol. 43, no. 5, pp. 1233–1246, Sep. 2007.

[69] B. Mirafzal, G. L. Skibinski, and R. M. Tallam, "Determination of parameters in the universal induction motor model," *IEEE Transactions on Industry Applications*, vol. 45, no. 1, pp. 142–151, Jan. 2009.

[70] L. Ran, S. Gokani, J. Clare, K. J. Bradley, and C. Christopoulos, "Conducted electromagnetic emissions in induction motor drive systems. i. time domain analysis and identification of dominant modes," *IEEE Transactions on Power Electronics*, vol. 13, no. 4, pp. 757–767, July 1998.

[71] J. Sun and L. Xing, "Parameterization of three-phase electric machine models for emi simulation," *IEEE Transactions on Power Electronics*, vol. 29, no. 1, pp. 36–41, Jan. 2014.

[72] G. Vidmar and D. Miljavec, "A universal high-frequency three-phase electric-motor model suitable for the delta- and star-winding connections," *IEEE Transactions on Power Electronics*, vol. 30, no. 8, pp. 4365–4376, Aug. 2015.

[73] M. S. Toulabi, L. Wang, L. Bieber, S. Filizadeh, and J. Jatskevich, "A universal high-frequency induction machine model and characterization method for arbitrary stator winding connections," *IEEE Transactions on Energy Conversion*, vol. 34, no. 3, pp. 1164–1177, Sep. 2019.

[74] D. Zhao, K. Shen, W. Liu, L. Lang, and P. Liang, "A measurement-based wide-frequency model for aircraft wound-rotor synchronous machine," *IEEE Transactions on Magnetics*, vol. 55, no. 7, pp. 1–8, July 2019.

[75] L. Wang, C. Ngai-Man Ho, F. Canales, and J. Jatskevich, "High-frequency modeling of the long-cable-fed induction motor drive system using tlm approach

for predicting overvoltage transients," *IEEE Transactions on Power Electronics*, vol. 25, no. 10, pp. 2653–2664, Oct. 2010.

[76] X. Fang, S. Li, and D. Jiandong, "Prediction model of conducted common-mode emi in pwm motor drive system," in *Proc. International Conference on Pervasive Computing, Signal Processing and Applications*, Harbin, China, Sep. 2010, pp. 1298–1301.

[77] M. Moreau, N. Idir, and P. Le Moigne, "Modeling of conducted emi in adjustable speed drives," *IEEE Transactions on Electromagnetic Compatibility*, vol. 51, no. 3, pp. 665–672, Aug. 2009.

[78] I. Stevanović, B. Wunsch, G. L. Madonna, and S. Skibin, "High-frequency behavioral multiconductor cable modeling for emi simulations in power electronics," *IEEE Transactions on Industrial Informatics*, vol. 10, no. 2, pp. 1392–1400, May 2014.

[79] B. Wunsch, I. Stevanović, and S. Skibin, "Length-scalable multiconductor cable modeling for emi simulations in power electronics," *IEEE Transactions on Power Electronics*, vol. 32, no. 3, pp. 1908–1916, Mar. 2017.

[80] C. Marlier, A. Videt, and N. Idir, "Nif-based frequency-domain modeling method of three-wire shielded energy cables for emc simulation," *IEEE Transactions on Electromagnetic Compatibility*, vol. 57, no. 1, pp. 145–155, Feb. 2015.

[81] W. L. de Souza, H. de Paula, A. De Conti, and R. C. Mesquita, "Cable parameter calculation for typical industrial installation methods and high-frequency

studies," *IEEE Transactions on Industry Applications*, vol. 54, no. 4, pp. 3919–3927, July 2018.

[82] J. S. Lai, X. Huang, E. Pepa, S. Chen, and T. W. Nehl, "Inverter emi modeling and simulation methodologies," *IEEE Transactions on Industrial Electronics*, vol. 53, no. 3, pp. 736–744, June 2006.

[83] G. Frantz, D. Frey, J. L. Schanen, B. Revol, H. Bishnoi, and P. Mattavelli, "Emc models for power electronics: From converter design to system level," in *Proc. IEEE Energy Conversion Congress and Exposition*, Denver, CO, Sep. 2013, pp. 4247–4252.

[84] K. Mainali and R. Oruganti, "Conducted emi mitigation techniques for switch-mode power converters: A survey," *IEEE Transactions on Power Electronics*, vol. 25, no. 9, pp. 2344–2356, Sep. 2010.

[85] S. Natarajan, T. Sudhakar Babu, K. Balasubramanian, U. Subramaniam, and D. J. Almakhles, "A state-of-the-art review on conducted electromagnetic interference in non-isolated dc to dc converters," *IEEE Access*, vol. 8, pp. 2564–2577, 2020.

[86] R. Gamoudi, D. Elhak Chariag, and L. Sbita, "A review of spread-spectrum-based pwm techniques—a novel fast digital implementation," *IEEE Transactions on Power Electronics*, vol. 33, no. 12, pp. 10 292–10 307, Dec. 2018.

[87] Q. Li and D. Jiang, "Variable switching frequency pwm strategy of two-level rectifier for dc-link voltage ripple control," *IEEE Transactions on Power Electronics*, vol. 33, no. 8, pp. 7193–7202, Aug. 2018.

[88] J. Chen, D. Jiang, Z. Shen, W. Sun, and Z. Fang, "Uniform distribution pulsewidth modulation strategy for three-phase converters to reduce conducted emi and switching loss," *IEEE Transactions on Industrial Electronics*, vol. 67, no. 8, pp. 6215–6226, Aug 2020.

[89] A. Charalambous, X. Yuan, and N. McNeill, "High-frequency emi attenuation at source with the auxiliary commutated pole inverter," *IEEE Transactions on Power Electronics*, vol. 33, no. 7, pp. 5660–5676, July 2018.

[90] Y. Yang, Y. Wen, and Y. Gao, "A novel active gate driver for improving switching performance of high-power sic mosfet modules," *IEEE Transactions on Power Electronics*, vol. 34, no. 8, pp. 7775–7787, Aug. 2019.

[91] H. C. P. Dymond, J. Wang, D. Liu, J. J. O. Dalton, N. McNeill, D. Pamunuwa, S. J. Hollis, and B. H. Stark, "A 6.7-ghz active gate driver for gan fets to combat overshoot, ringing, and emi," *IEEE Transactions on Power Electronics*, vol. 33, no. 1, pp. 581–594, Jan. 2018.

[92] F. Chen, R. Burgos, D. Boroyevich, and X. Zhang, "Low-frequency common-mode voltage control for systems interconnected with power converters," *IEEE Transactions on Industrial Electronics*, vol. 64, no. 1, pp. 873–882, Jan. 2017.

[93] M. Perotti and F. Fiori, "Investigating the emi mitigation in power inverters using delay compensation," *IEEE Transactions on Power Electronics*, vol. 34, no. 5, pp. 4270–4278, May 2019.

[94] D. Han, S. Li, Y. Wu, W. Choi, and B. Sarlioglu, "Comparative analysis on conducted cm emi emission of motor drives: Wbg versus si devices," *IEEE Transactions on Industrial Electronics*, vol. 64, no. 10, pp. 8353–8363, Oct 2017.

[95] C. T. Morris, D. Han, and B. Sarlioglu, "Reduction of common mode voltage and conducted emi through three-phase inverter topology," *IEEE Transactions on Power Electronics*, vol. 32, no. 3, pp. 1720–1724, March 2017.

[96] D. Han, C. T. Morris, and B. Sarlioglu, "Common-mode voltage cancellation in pwm motor drives with balanced inverter topology," *IEEE Transactions on Industrial Electronics*, vol. 64, no. 4, pp. 2683–2688, April 2017.

[97] L. Dai, W. Chen, X. Yang, M. Zheng, Y. Yang, and R. Wang, "A multi-function common mode choke based on active cm emi filters for ac/dc power converters," *IEEE Access*, vol. 7, pp. 43 534–43 546, 2019.

[98] D. Xu, C. K. Lee, S. Kiratipongvoot, and W. M. Ng, "An active emi choke for both common- and differential-mode noise suppression," *IEEE Transactions on Industrial Electronics*, vol. 65, no. 6, pp. 4640–4649, June 2018.

[99] R. Goswami and S. Wang, "Modeling and stability analysis of active differential-mode emi filters for ac/dc power converters," *IEEE Transactions on Power Electronics*, vol. 33, no. 12, pp. 10 277–10 291, Dec. 2018.

[100] Jih-Sheng Lai, Xudong Huang, E. Pepa, Shaotang Chen, and T. W. Nehl, "Inverter emi modeling and simulation methodologies," *IEEE Transactions on Industrial Electronics*, vol. 53, no. 3, pp. 736–744, June 2006.

[101] Kuang Sheng, B. W. Williams, and S. J. Finney, "A review of igbt models," *IEEE Transactions on Power Electronics*, vol. 15, no. 6, pp. 1250–1266, Nov. 2000.

[102] L. Han, L. Liang, Y. Kang, and Y. Qiu, "A review of sic igbt: Models, fabrications, characteristics, and applications," *IEEE Transactions on Power Electronics*, vol. 36, no. 2, pp. 2080–2093, Feb. 2021.

[103] A. R. Hefner, "An improved understanding for the transient operation of the power insulated gate bipolar transistor (igbt)," *IEEE Transactions on Power Electronics*, vol. 5, no. 4, pp. 459–468, Oct. 1990.

[104] A. R. Hefner and D. M. Diebolt, "An experimentally verified igbt model implemented in the saber circuit simulator," *IEEE Transactions on Power Electronics*, vol. 9, no. 5, pp. 532–542, Sep. 1994.

[105] GoodFellow. (2021) Polyethylene terephthalate (polyester, pet, petp). [Online]. Available: http://www.goodfellow.com/E/Polyethylene-terephthalate.html

[106] O. Magdun and A. Binder, "High-frequency induction machine modeling for common mode current and bearing voltage calculation," *IEEE Transactions on Industry Applications*, vol. 50, no. 3, pp. 1780–1790, May 2014.

[107] H. Zhang, L. Yang, S. Wang, and J. Puukko, "Common-mode emi noise modeling and reduction with balance technique for three-level neutral point clamped topology," *IEEE Transactions on Industrial Electronics*, vol. 64, no. 9, pp. 7563–7573, Sep. 2017.

[108] T. Williams and K. Armstrong, *EMC for Systems and Installations*. Elsevier Science, 1999.

[109] Texas Instrument. (2021) Automotive 3-v to 36-v, 6-a low EMI synchronous step-down quiet converter with integrated capacitors. [Online]. Available: https://www.ti.com/product/LMQ61460-Q1

[110] A. Eadie. (2014) How to do an emc design review. [Online]. Available: https://emcfastpass.com/emc-design-review/

[111] S. Vasudevan. (2020, May) Five steps for successful automotive emc design. [Online]. Available: https://interferencetechnology.com/five-steps-for-successful-automotive-emc-design/

[112] General Motors. (2012) General specification for electrical/electronic components and subsystems, electromagnetic compatibility. [Online]. Available: https://bit.ly/39g1qRH

[113] Ford Motor Company. (2003) Emc design for automotive electronics. [Online]. Available: https://bit.ly/2MsllE0

[114] A. Eadie. (2020) Electromagnetic compatibility (emc) testing: The beginner's guide - emc fastpass. [Online]. Available: https://emcfastpass.com/emc-testing-beginners-guide/

[115] Academy of EMC. (2021) Emc standards. [Online]. Available: https://www.academyofemc.com/emc-standards

[116] EMC Bayswater. (2017, Feb.) How to write an emc test plan. [Online]. Available: https://www.emcbayswater.com.au/blog/certifications/how-to-write-an-emc-test-plan/

[117] SolarEdge. (2020) Three phase commercial inverters. [Online]. Available: https://www.solaredge.com/us/products/pv-inverter/three-phase#/

[118] IEC, "Electromagnetic compatibility (EMC) – Part 4-6: Testing and measurement techniques – Immunity to conducted disturbances, induced by radio-frequency fields," standard IEC 61000-4-6, Oct. 2013.

[119] ——, "Electromagnetic compatibility (EMC) – Part 3-2: Limits – Limits for harmonic current emissions (equipment input current ≤16 A per phase) ," standard IEC 61000-3-2, Jul. 2020.

[120] ——, "Electromagnetic compatibility (EMC) – Part 3-12: Limits – Limits for harmonic currents produced by equipment connected to public low-voltage systems with input current ≥16 A and ≤75 A per phase ," standard IEC 61000-3-12, May 2011.

[121] ——, "Electromagnetic compatibility (EMC) – Part 3-3: Limits – Limitation of voltage changes, voltage fluctuations and flicker in public low-voltage supply systems, for equipment with rated current ≤ 16 A per phase and not subject to conditional connection ," standard IEC 61000-3-3, May 2017.

[122] ——, "Electromagnetic compatibility (EMC) – Part 4-2: Testing and measurement techniques – Electrostatic discharge immunity test," standard IEC 61000-4-2, Dec. 2008.

[123] ——, "Electromagnetic compatibility (EMC) – Part 4-4: Testing and measurement techniques – Electrical fast transient/burst immunity test," standard IEC 61000-4-4, Mar. 2012.

[124] ——, "Electromagnetic compatibility (EMC) – Part 4-5: Testing and measurement techniques – Surge immunity test ," standard IEC 61000-4-5, Aug. 2017.

[125] ——, "Electromagnetic compatibility (EMC) – Part 4-11: Testing and measurement techniques – Voltage dips, short interruptions and voltage variations immunity tests," standard IEC 61000-4-11, Jan. 2020.

[126] C. Rauscher, V. Janssen, and R. Minihold, *Fundamentals of spectrum analysis*. Rohde & Schwarz, 2016.

[127] L. Yang, S. Wang, H. Zhao, and Y. Zhi, "Prediction and analysis of emi spectrum based on the operating principle of emc spectrum analyzers," *IEEE Transactions on Power Electronics*, vol. 35, no. 1, pp. 263–275, Jan. 2020.

[128] M. Parvis, G. Perrone, and A. Vallan, "A precompliance emc test-set based on a sampling oscilloscope," *IEEE Transactions on Instrumentation and Measurement*, vol. 52, no. 4, pp. 1220–1223, Aug. 2003.

[129] J. Meng, X. Zhang, L. Zhang, and Z. Zhao, "Time-domain low-frequency non-periodic transient emi measurement system," *IET Science, Measurement & Technology*, vol. 13, no. 5, pp. 650–655, July 2019.

[130] C. Hoffmann and P. Russer, "A real-time low-noise ultrabroadband time-domain emi measurement system up to 18 ghz," *IEEE Transactions on Electromagnetic Compatibility*, vol. 53, no. 4, pp. 882–890, Nov. 2011.

[131] X. Kong, Y. Xie, Q. Li, S. He, and Y. Jin, "Development of one-dimensional norm detector for nanosecond-level transient electric field measurement," *IEEE Transactions on Electromagnetic Compatibility*, vol. 59, no. 4, pp. 1035–1040, Aug. 2017.

[132] S. Braun and P. Russer, "A low-noise multiresolution high-dynamic ultra-broadband time-domain emi measurement system," *IEEE Transactions on Microwave Theory and Techniques*, vol. 53, no. 11, pp. 3354–3363, Nov. 2005.

[133] S. Braun, T. Donauer, and P. Russer, "A real-time time-domain emi measurement system for full-compliance measurements according to cispr 16-1-1," *IEEE Transactions on Electromagnetic Compatibility*, vol. 50, no. 2, pp. 259–267, May 2008.

[134] M. A. Azpúrua, J. A. Oliva, M. Pous, and F. Silva, "Fast and automated verification of multi-channel full time-domain emi measurement systems," in *In proceedings of IEEE International Instrumentation and Measurement Technology Conference (I2MTC)*, May 2017, pp. 1–6.

[135] K. Hörmaier, H. Zangl, and H. Zojer, "An emi receiver model to evaluate electromagnetic emissions by simulation," in *In proceedings of IEEE International Instrumentation and Measurement Technology Conference*, May 2012, pp. 2558–2562.

[136] M. A. Azpúrua, M. Pous, and F. Silva, "On the statistical properties of the peak detection for time-domain emi measurements," *IEEE Transactions on Electromagnetic Compatibility*, vol. 57, no. 6, pp. 1374–1381, Dec. 2015.

[137] F. Krug and P. Russer, "Quasi-peak detector model for a time-domain measurement system," *IEEE Transactions on Electromagnetic Compatibility*, vol. 47, no. 2, pp. 320–326, May 2005.

[138] M. A. Azpúrua, M. Pous, and F. Silva, "A measurement system for radiated transient electromagnetic interference based on general purpose instruments," in *IEEE International Symposium on Electromagnetic Compatibility (EMC)*, Aug. 2015, pp. 1189–1194.

[139] J. A. Russer and S. Braun, "A novel vector near-field scanning system for emission measurements in time-domain," in *In proceedings of IEEE International Symposium on Electromagnetic Compatibility*, Aug. 2012, pp. 462–467.

[140] M. Pous, M. A. Azpúrua, J. A. Oliva, M. Aragón, I. González, and F. Silva, "Full time domain emi measurement system applied to railway emissions according to iec 62236-3-1/en 50121-3-1 standards," in *In proceedings of IEEE International Symposium on Electromagnetic Compatibility (EMC EUROPE)*, Aug. 2018, pp. 260–265.

[141] M. Pous and F. Silva, "Full-spectrum apd measurement of transient interferences in time domain," *IEEE Transactions on Electromagnetic Compatibility*, vol. 56, no. 6, pp. 1352–1360, Dec. 2014.

[142] Y. Zhang and L. Jiang, "A novel data-driven analysis method for electromagnetic radiations based on dynamic mode decomposition," *IEEE Transactions on Electromagnetic Compatibility*, vol. 62, no. 4, pp. 1443–1450, Aug. 2020.

[143] M. A. Azpúrua, M. Pous, and F. Silva, "Decomposition of electromagnetic interferences in the time-domain," *IEEE Transactions on Electromagnetic Compatibility*, vol. 58, no. 2, pp. 385–392, April 2016.

[144] ——, "Specifying the waveforms for the calibration of cispr 16-1-1 measuring receivers," *IEEE Transactions on Electromagnetic Compatibility*, vol. 62, no. 3, pp. 654–662, June 2020.

[145] M. A. Azpúrua, M. Pous, J. A. Oliva, B. Pinter, M. Hudlička, and F. Silva, "Waveform approach for assessing conformity of cispr 16-1-1 measuring receivers," *IEEE Transactions on Instrumentation and Measurement*, vol. 67, no. 5, pp. 1187–1198, May 2018.

[146] S. M. Satav and V. Agarwal, "Design and development of a low-cost digital magnetic field meter with wide dynamic range for emc precompliance measurements and other applications," *IEEE Transactions on Instrumentation and Measurement*, vol. 58, no. 8, pp. 2837–2846, Aug. 2009.

[147] H. Lin, H. Chen, C. Kuo, and Y. Chang, "Design and application of a mobile miniature current probe for analysing the cause of emi noise in ic circuits," *IET Science, Measurement & Technology*, vol. 11, no. 5, pp. 655–665, Aug. 2017.

[148] W. Liu, Z. Yan, Z. Min, Z. Ning, and J. Wang, "Design of miniature active magnetic probe for near-field weak signal measurement in ics," *IEEE Microwave and Wireless Components Letters*, vol. 30, no. 3, pp. 312–315, March 2020.

[149] W. Liu, Z. Yan, J. Wang, X. Yan, and J. Fan, "An ultrawideband electric probe based on u-shaped structure for near-field measurement from 9 khz to 40 ghz,"

IEEE Antennas and Wireless Propagation Letters, vol. 18, no. 6, pp. 1283–1287, June 2019.

[150] Z. Min, Z. Yan, W. Liu, J. Wang, D. Su, and X. Yan, "A miniature high-sensitivity active electric field probe for near-field measurement," *IEEE Antennas and Wireless Propagation Letters*, vol. 18, no. 12, pp. 2552–2556, Dec. 2019.

[151] R. Tani, I. Wu, K. Gotoh, Y. Matsumoto, S. Ishigami, R. Suga, and O. Hashimoto, "Characterization of ac/coaxial adapter for lisn calibration above 30 mhz using improved equivalent circuit model," *IEEE Transactions on Electromagnetic Compatibility*, vol. 60, no. 5, pp. 1357–1365, Oct. 2018.

[152] J. Zhang, K. W. Kam, J. Min, V. V. Khilkevich, D. Pommerenke, and J. Fan, "An effective method of probe calibration in phase-resolved near-field scanning for emi application," *IEEE Transactions on Instrumentation and Measurement*, vol. 62, no. 3, pp. 648–658, March 2013.

[153] K. Fujii, S. Harada, A. Sugiura, Y. Matsumoto, and Y. Yamanaka, "An estimation method for the free-space antenna factor of vhf emi antennas," *IEEE Transactions on Electromagnetic Compatibility*, vol. 47, no. 3, pp. 627–634, Aug. 2005.

[154] H. Chen and K. Lin, "An improved method for free-space antenna-factor measurement by using the music algorithm," *IEEE Transactions on Electromagnetic Compatibility*, vol. 53, no. 2, pp. 274–282, May 2011.

[155] V. Trainotti, "Electromagnetic compatibility (emc) antenna gain and factor," *IEEE Transactions on Electromagnetic Compatibility*, vol. 59, no. 4, pp. 1006–1015, Aug. 2017.

[156] J. Arroyo. (2019) Interference technology, 2019 emc testing guide. [Online]. Available: https://learn.interferencetechnology.com/2019-emc-testing-guide/

[157] S. Kouro, M. Malinowski, K. Gopakumar, J. Pou, L. G. Franquelo, B. Wu, J. Rodriguez, M. A. Pérez, and J. I. Leon, "Recent advances and industrial applications of multilevel converters," *IEEE Transactions on Industrial Electronics*, vol. 57, no. 8, pp. 2553–2580, Aug. 2010.

[158] J. Rodriguez, S. Bernet, B. Wu, J. O. Pontt, and S. Kouro, "Multilevel voltage-source-converter topologies for industrial medium-voltage drives," *IEEE Transactions on Industrial Electronics*, vol. 54, no. 6, pp. 2930–2945, Dec. 2007.

[159] T. Bruckner, S. Bernet, and H. Guldner, "The active npc converter and its loss-balancing control," *IEEE Transactions on Industrial Electronics*, vol. 52, no. 3, pp. 855–868, June 2005.

[160] F. A. Kharanaq, A. Emadi, and B. Bilgin, "Modeling of conducted emissions for emi analysis of power converters: State-of-the-art review," *IEEE Access*, vol. 8, pp. 189 313–189 325, 2020.

[161] J. Wang, X. Liu, Y. Xun, and S. Yu, "Common mode noise reduction of three-level active neutral point clamped inverters with uncertain parasitic capacitance of photovoltaic panels," *IEEE Transactions on Power Electronics*, vol. 35, no. 7, pp. 6974–6988, July 2020.

[162] J. Wang, X. Liu, Q. Peng, Y. Xun, S. Yu, N. Jiang, W. Wang, and F. Hou, "Co-reduction of common mode noise and loop current of three-level active neutral point clamped inverters," *IEEE Journal of Emerging and Selected Topics in Power Electronics*, vol. 9, no. 1, pp. 1088–1103, Feb. 2021.

[163] E. Gubia, P. Sanchis, A. Ursua, J. Lopez, and L. Marroyo, "Frequency domain model of conducted emi in electrical drives," *IEEE Power Electronics Letters*, vol. 3, no. 2, pp. 45–49, June 2005.

[164] M. Jin and M. Weiming, "A new technique for modeling and analysis of mixed-mode conducted emi noise," *IEEE Transactions on Power Electronics*, vol. 19, no. 6, pp. 1679–1687, Nov. 2004.

[165] D. Jiang, Q. Li, and Z. Shen, "Model predictive pwm for ac motor drives," *IET Electric Power Applications*, vol. 11, no. 5, pp. 815–822, 2017. [Online]. Available: https://ietresearch.onlinelibrary.wiley.com/doi/abs/10.1049/iet-epa.2016.0456

[166] L. Xing and J. Sun, "Conducted common-mode emi reduction by impedance balancing," *IEEE Transactions on Power Electronics*, vol. 27, no. 3, pp. 1084–1089, March 2012.

[167] Y. Li, H. Zhang, S. Wang, H. Sheng, C. P. Chng, and S. Lakshmikanthan, "Investigating switching transformers for common mode emi reduction to remove common mode emi filters and y-capacitors in flyback converters," *IEEE Journal of Emerging and Selected Topics in Power Electronics*, vol. 6, no. 4, pp. 2287–2301, Dec. 2018.

[168] X. Yang, Y. Yuan, X. Zhang, and P. R. Palmer, "Shaping high-power igbt switching transitions by active voltage control for reduced emi generation," *IEEE Transactions on Industry Applications*, vol. 51, no. 2, pp. 1669–1677, March 2015.

[169] P. Pairodamonchai, S. Suwankawin, and S. Sangwongwanich, "Design and implementation of a hybrid output emi filter for high-frequency common-mode voltage compensation in pwm inverters," *IEEE Transactions on Industry Applications*, vol. 45, no. 5, pp. 1647–1659, Sep. 2009.

[170] H. Akagi and T. Shimizu, "Attenuation of conducted emi emissions from an inverter-driven motor," *IEEE Transactions on Power Electronics*, vol. 23, no. 1, pp. 282–290, Jan. 2008.

[171] D. Jiang and F. Wang, "Variable switching frequency pwm for three-phase converters based on current ripple prediction," *IEEE Transactions on Power Electronics*, vol. 28, no. 11, pp. 4951–4961, Nov. 2013.

[172] J. Xu, Z. Nie, and J. Zhu, "Characterization and selection of probability statistical parameters in random slope pwm based on uniform distribution," *IEEE Transactions on Power Electronics*, vol. 36, no. 1, pp. 1184–1192, Jan. 2021.

[173] H. G. Li, S. D. Gong, J. W. Liu, and D. L. Su, "Cmos-based chaotic pwm generator for emi reduction," *IEEE Transactions on Electromagnetic Compatibility*, vol. 59, no. 4, pp. 1224–1231, Aug. 2017.

[174] Z. Yang, H. Li, Y. Ding, and J. Wang, "Continuous multi-scroll chaotic pwm and its chaotic signal selection method for emi suppression of power converters," *IEEE Access*, vol. 8, pp. 168 910–168 922, Aug. 2020.

[175] D. Holmes and T. Lipo, *Pulse Width Modulation for Power Converters: Principles and Practice*, ser. IEEE Press Series on Power and Energy Systems. Wiley, 2003. [Online]. Available: https://books.google.ca/books?id=8LGi1AjSfpcC

[176] J. Chen, D. Jiang, W. Sun, Z. Shen, and Y. Zhang, "A family of spread-spectrum modulation schemes based on distribution characteristics to reduce conducted emi for power electronics converters," *IEEE Transactions on Industry Applications*, vol. 56, no. 5, pp. 5142–5157, Sep. 2020.

[177] M. M. Bech, F. Blaabjerg, and J. K. Pedersen, "Random modulation techniques with fixed switching frequency for three-phase power converters," *IEEE Transactions on Power Electronics*, vol. 15, no. 4, pp. 753–761, July 2000.

[178] K. K. Tse, H. S. . Chung, S. Y. Huo, and H. C. So, "Analysis and spectral characteristics of a spread-spectrum technique for conducted emi suppression," *IEEE Transactions on Power Electronics*, vol. 15, no. 2, pp. 399–410, March 2000.

[179] S. Kaboli, J. Mahdavi, and A. Agah, "Application of random pwm technique for reducing the conducted electromagnetic emissions in active filters," *IEEE Transactions on Industrial Electronics*, vol. 54, no. 4, pp. 2333–2343, Aug 2007.

[180] F. Pareschi, G. Setti, R. Rovatti, and G. Frattini, "Practical optimization of emi reduction in spread spectrum clock generators with application to switching dc/dc converters," *IEEE Transactions on Power Electronics*, vol. 29, no. 9, pp. 4646–4657, Sep. 2014.

[181] D. Gonzalez, J. Balcells, A. Santolaria, J. Le Bunetel, J. Gago, D. Magnon, and S. Brehaut, "Conducted emi reduction in power converters by means of periodic switching frequency modulation," *IEEE Transactions on Power Electronics*, vol. 22, no. 6, pp. 2271–2281, Nov. 2007.

[182] Y. Wang, A. Poorfakhraei, N. Mehdi, and A. Emadi, "Comparative analysis of 2-level and 3-level voltage source inverters in traction applications," in *IEEE Transportation Electrification Conference Expo (ITEC)*, June 2021, pp. 614–619.

[183] A. Kersten, K. Oberdieck, J. Gossmann, A. Bubert, R. Loewenherz, M. Neubert, T. Thiringer, and R. W. D. Doncker, "Measuring and separating conducted three-wire emissions from a fault-tolerant, npc propulsion inverter with a split-battery using hardware separators based on hf transformers," *IEEE Transactions on Power Electronics*, vol. 36, no. 1, pp. 378–390, Jan. 2021.

[184] D. Zhou and D. Rouaud, "Experimental comparisons of space vector neutral point balancing strategies for three-level topology," *IEEE Transactions on Power Electronics*, vol. 16, no. 6, pp. 872–879, Nov. 2001.

[185] S. Busquets-Monge, J. Bordonau, D. Boroyevich, and S. Somavilla, "The nearest three virtual space vector pwm - a modulation for the comprehensive neutral-point balancing in the three-level npc inverter," *IEEE Power Electronics Letters*, vol. 2, no. 1, pp. 11–15, March 2004.

[186] S. Busquets-Monge, J. D. Ortega, J. Bordonau, J. A. Beristain, and J. Rocabert, "Closed-loop control of a three-phase neutral-point-clamped inverter using an optimized virtual-vector-based pulsewidth modulation," *IEEE Transactions on Industrial Electronics*, vol. 55, no. 5, pp. 2061–2071, May 2008.

[187] S. Busquets Monge, S. Somavilla, J. Bordonau, and D. Boroyevich, "Capacitor voltage balance for the neutral-point- clamped converter using the virtual space vector concept with optimized spectral performance," *IEEE Transactions on Power Electronics*, vol. 22, no. 4, pp. 1128–1135, July 2007.

[188] C. Q. Xiang, C. Shu, D. Han, B.-K. Mao, X. Wu, and T.-J. Yu, "Improved virtual space vector modulation for three-level neutral-point-clamped converter with feedback of neutral-point voltage," *IEEE Transactions on Power Electronics*, vol. 33, no. 6, pp. 5452–5464, June 2018.

[189] X. Wu, G. Tan, Z. Ye, G. Yao, Z. Liu, and G. Liu, "Virtual-space-vector pwm for a three-level neutral-point-clamped inverter with unbalanced dc-links," *IEEE Transactions on Power Electronics*, vol. 33, no. 3, pp. 2630–2642, March 2018.

[190] J. Wang, Y. Gao, and W. Jiang, "A carrier-based implementation of virtual space vector modulation for neutral-point-clamped three-level inverter," *IEEE Transactions on Industrial Electronics*, vol. 64, no. 12, pp. 9580–9586, Dec. 2017.

[191] W. Jiang, X. Huang, J. Wang, J. Wang, and J. Li, "A carrier-based pwm strategy providing neutral-point voltage oscillation elimination for multi-phase neutral point clamped 3-level inverter," *IEEE Access*, vol. 7, pp. 124 066–124 076, 2019.

[192] J. Weidong, L. Wang, J. Wang, X. Zhang, and P. Wang, "A carrier-based virtual space vector modulation with active neutral-point voltage control for a neutral-point-clamped three-level inverter," *IEEE Transactions on Industrial Electronics*, vol. 65, no. 11, pp. 8687–8696, Nov. 2018.

[193] A. M. Hava and E. Ün, "A high-performance pwm algorithm for common-mode voltage reduction in three-phase voltage source inverters," *IEEE Transactions on Power Electronics*, vol. 26, no. 7, pp. 1998–2008, July 2011.

[194] H. Zhang, A. Von Jouanne, S. Dai, A. Wallace, and F. Wang, "Multilevel inverter modulation schemes to eliminate common-mode voltages," *IEEE Transactions on Industry Applications*, vol. 36, no. 6, pp. 1645–1653, Nov. 2000.

[195] W. Jiang, P. Wang, M. Ma, J. Wang, J. Li, L. Li, and K. Chen, "A novel virtual space vector modulation with reduced common-mode voltage and eliminated neutral point voltage oscillation for neutral point clamped three-level inverter," *IEEE Transactions on Industrial Electronics*, vol. 67, no. 2, pp. 884–894, Feb. 2020.

[196] F. Guo, T. Yang, A. M. Diab, S. S. Yeoh, S. Bozhko, and P. Wheeler, "An enhanced virtual space vector modulation scheme of three-level npc converters for more-electric-aircraft applications," *IEEE Transactions on Industry Applications*, vol. 57, no. 5, pp. 5239–5251, Sep. 2021.

[197] S. Xia, X. Wu, J. Zheng, X. Li, and K. Wang, "A virtual space vector pwm with active neutral point voltage control and common mode voltage suppression for three-level npc converters," *IEEE Transactions on Industrial Electronics*, vol. 68, no. 12, pp. 11 761–11 771, Dec. 2021.

[198] C. Hu, X. Yu, D. G. Holmes, W. Shen, Q. Wang, F. Luo, and N. Liu, "An improved virtual space vector modulation scheme for three-level active neutral-point-clamped inverter," *IEEE Transactions on Power Electronics*, vol. 32, no. 10, pp. 7419–7434, Oct. 2017.

[199] P. Liu, S. Duan, C. Yao, and C. Chen, "A double modulation wave cbpwm strategy providing neutral-point voltage oscillation elimination and cmv reduction for three-level npc inverters," *IEEE Transactions on Industrial Electronics*, vol. 65, no. 1, pp. 16–26, Jan. 2018.

[200] J. Pou, J. Zaragoza, P. Rodriguez, S. Ceballos, V. M. Sala, R. P. Burgos, and D. Boroyevich, "Fast-processing modulation strategy for the neutral-point-clamped converter with total elimination of low-frequency voltage oscillations in the neutral point," *IEEE Transactions on Industrial Electronics*, vol. 54, no. 4, pp. 2288–2294, Aug. 2007.

[201] J. Prieto, M. Jones, F. Barrero, E. Levi, and S. Toral, "Comparative analysis of discontinuous and continuous pwm techniques in vsi-fed five-phase induction motor," *IEEE Transactions on Industrial Electronics*, vol. 58, no. 12, pp. 5324–5335, Dec. 2011.

[202] B. P. McGrath, D. G. Holmes, and T. Meynard, "Reduced pwm harmonic distortion for multilevel inverters operating over a wide modulation range,"

IEEE Transactions on Power Electronics, vol. 21, no. 4, pp. 941–949, July 2006.

[203] D. Glose and R. Kennel, "Continuous space vector modulation for symmetrical six-phase drives," *IEEE Transactions on Power Electronics*, vol. 31, no. 5, pp. 3837–3848, May 2016.

[204] N. Beniwal, C. D. Townsend, G. G. Farivar, J. Pou, S. Ceballos, and H. D. Tafti, "Band-limited three-level modulation for balancing capacitor voltages in neutral-point-clamped converters," *IEEE Transactions on Power Electronics*, vol. 35, no. 9, pp. 9737–9752, Sep. 2020.